15

Interferometric GPS/Micro-Mechanical Gyro Attitude Determination System: A Study Into the Integration Issues

by

Antonio Giustino, 2nd Lt, USAF

B.S. Engineering Sciences
United States Air Force Academy, 1996

Submitted to the Department of Aeronautics and Astronautics in partial fulfillment of the requirements for the Degree of

Master of Science in Aeronautics and Astronautics

at the

MASSACHUSETTS INSTITUTE OF TECHNOLOGY

June 1998

Signature of Author.....
Department of Aeronautics and Astronautics
June 1998

Approved by.....
Christopher N. D' Souza
Charles Stark Draper Laboratory, Inc.
Technical Supervisor

Certified by.....
Professor John J. Deyst, Jr.
Department of Aeronautics and Astronautics
Thesis Supervisor

Accepted by.....
Jaime Peraire
Professor of Aeronautics and Astronautics
Chair, Graduate Office

Accepted by .....

Jaime Peraire
Professor of Aeronautics and Astronautics
Chair, Graduate Office

Inteferometric GPS/Micro-Mechanical Gyro Attitude Determination System: A Study Into the Integration Issues

by

Antonio Giustino

Submitted to the Department of Aeronautics and Astronautics on
May 8, 1998, in partial fulfillment of the requirements for the
Degree of Master of Science in Aeronautics and Astronautics.

Abstract

The near future will see a proliferation of small low cost communication and science satellites with modest (~0.1 - 0.5 deg) pointing requirements which will use attitude determination systems (ADS's) of low power, weight, size and cost. This thesis is a study into the integration issues of such a system, that uses micro-mechanical inertial sensors and an interferometric GPS (IGPS) attitude determining receiver that are tightly coupled using "model based" estimation techniques. The integration issues analyzed include: the effect on performance of limited IGPS use, the effect on performance of various gyro qualities and model accuracies, the inherent robustness to failure of the system and a power consumption analysis for a minimum energy IGPS receiver.

It was found that attitude performance varied less than 0.05 degrees (RSS) when the interval between GPS phase measurements was varied from once every second to once every 30 seconds. This justifies the development of a minimum energy receiver to take advantage of the power savings of less frequent GPS measurements. During times of low dynamic model accuracy, the IGPS/MM Gyro ADS was bound by the steady state attitude error of the IGPS which averages a 1 σ RSS error of about 0.28 degrees within the GPS update range mentioned above. Attitude error also depends on the gyro quality, and various projected system accuracies are given using several gyro error models. Real micro-mechanical gyro data from a prototype gyro was successfully integrated with real GPS phase measurements using an Extended Kalman filter. Failure scenarios and power expenditures were also analyzed using steady state linear covariance analysis as well as a space simulation which uses orbital parameters of a telecommunication satellite constellation. Total power expenditure of 200 mWatts can be achieved for this system and still fulfill mission requirements.

Professor John J. Deyst, Jr.

Title: Professor, Department of Aeronautics and Astronautics

Technical Supervisor: Christopher N. D' Souza
Title: Senior Member Technical Staff, C.S. Draper Laboratory, Inc.

Acknowledgments

This page serves as an attempt to thank the many people who have made this work possible and have made my days in New England so memorable. I owe more to you than I could possibly verbalize here.

I would like to thank the Draper Lab and its staff for giving me this opportunity. A debt of gratitude goes to my technical advisor, Chris D'Souza, for his guidance and support in this project. Many thanks also to the IR&D staff, namely Dick Phillips and Kevin Mahar, for showing me how the pros do it; and to Roy Setterlund for funding my fellowship. To Varun Puri, thanks for providing the foundation for all of this work. The VIHIGP-SAIRSJMEF will somehow live on.

Thanks to all the DLF's who have made the 5th floor so much fun: Atiff, Carla, Christina, Matt, Nick, Geoff, Mike, Andy, Jack, Brett, Nhut and Pat. To the crew: Chris, Beau, George, Ben, Gordon, Steve and Rudy; for making the Boston area nightlife such a "good time". Rudy, man, I will always remember those late nights in the Lab with only our CD's and Netscape to keep us sane. Someday we'll have to implement our plans for the Chuck D. 5th Floor Disco Dance Club. To my Market Street roomies, a.k.a. *theboys*: Ted and Chad, thanks for the memories. You know I'm coming to visit: Chad, keep some salsa ready; Ted, don't forget to clean out Son's litter box.

I saved the most important for last: my family. I couldn't have done it without you guys. Teresa and Domenico, thanks for coming up and visiting. I hope it wasn't just for the Guiness. Mom, Dad and Pietro: thanks for all your support. I love you guys. Finally, I want to dedicate this thesis to Abuela.

This thesis was prepared at The Charles Stark Draper Laboratory, Inc., under Independent Research and Development #13329.

Publication of this thesis does not constitute approval by Draper or the sponsoring agency of the findings or conclusions contained herein. It is published for the exchange and stimulation of ideas.

Permission is hereby granted by the Author to the Massachusetts Institute of Technology to reproduce any or all of this thesis.

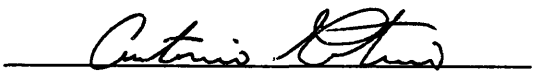

Antonio Giustino

Table of Contents

List of Figures

List of Tables

List of Acronyms

ADOP - Attitude Dilution of Precision

ACS - Attitude Control System

ADS - Attitude Determination System

ARW - Angle Random Walk

ASICS - Application Specific Integrated Circuits

DCAR - Decoupled and Constrained Ambiguity Resolution

DDP - Data Dependent Processor

DOP - Dilution of Precision

DSP - Digital Signal Processor

EKF - Extended Kalman Filter

GDOP - Geometric Dilution of Precision

GPS - Global Positioning System

IGPS - Interferometric GPS

LOS - Line of Sight

MAC's - Multiply Accumulates

MM - Micro-Mechanical (also known as MEM)

MEM - Micro-Electro-Mechanical

RFE - Radio Frequency Electronics

RPU - Receiver Processing Unit

SD - Single Difference

SV - Satellite Vehicle

T-C - Tightly-Coupled

TT&C - Telemetry Tracking and Command

Chapter 1

Introduction

The next few years will witness an explosion in the demand for communication infrastructure. With the rising popularity of the internet and an ever increasing need for global media communication such as fax, voice, data and video lines, the telecommunication industry will face the formidable challenge of trying to meet the demand. In addition to fiber optic lines, various small satellite constellations are being proposed and designed to provide large numbers of small, low cost communication platforms in low-Earth-orbit (LEO) and medium-Earth-orbit (MEO). Some of these projects include Iridium, Globalstar, Teledesic and Ellipso.

1.1 Objectives

The Charles Stark Draper Laboratory has been developing techniques for a new attitude determination system (ADS) for the small satellite market. This project proposes to synthesize two in-house navigation systems as an alternative for the traditional LEO/MEO spacecraft ADS suite. This system consists of the Draper Micro-Mechanical (MM) gyroscopes aided by an interferometric GPS (IGPS) receiver. The two systems are integrated in a tightly-coupled design through an Extended Kalman filter (EKF) described in Chapter 3.

Mechanical wheel gyros have been extensively used on spacecraft ADS in the past. The main disadvantages of these gyros are their relatively large weight, power and volume requirements; their cost; and their need for measurements from other sensors to bound error growth and keep their biases calibrated. The size and cost issue can now be overcome through advancements in micromachining and Application Specific Integrated Circuits (ASICs), which have led to the development of the MM gyros. The error growth and calibration challenge will be met by integrating an

attitude determining IGPS receiver with the gyros. The IGPS/MM Gyro ADS will use low quality, high output-rate gyros to measure dynamics while the interferometer will serve to bound errors through measurements at lower sampling frequencies.

As with any design, the proposed system must meet cost, performance and reliability criteria. This thesis addresses some of these issues. Increased performance usually comes at a price, and this study will address such trade-offs associated with this system's integration. An analysis is presented in Chapter 4 which summarizes the effects of using varying IGPS measurement updates, varying gyro qualities, and varying model confidences. Chapter 5 presents a demonstration of the robustness to failure inherent with this ADS. Chapter 7 addresses the power issue associated with the system.

1.2 The Sensors

A brief description of the theory and hardware pertaining to the two sensors used in this application is presented below.

1.2.1 IGPS

The use of GPS interferometry, in which the differential phase between antennas is used for attitude determination, is an increasingly significant application of the GPS system. Several commercial three-axis attitude determination receivers such as the Trimble Quadrex and TANS Vector, the Ashtech 3DF and the Loral Tensor, have been developed and marketed as off-the-shelf technology. The commercial IGPS receivers use a least squares point solution when computing attitude. Recent interferometry research has focused on using Kalman filtering of these attitude solutions to take advantage of previous attitude knowledge and gain improved performance.

Theory

In IGPS the phase of the L1 signal, the primary wave carrier transmitted by the GPS system, is used to estimate the orientation of the body frame with respect to a known reference frame. The carrier phase is tracked and differenced between two antennas to produce a measurement of relative range to the GPS satellite vehicle (SV). The following figure illustrates this principle.

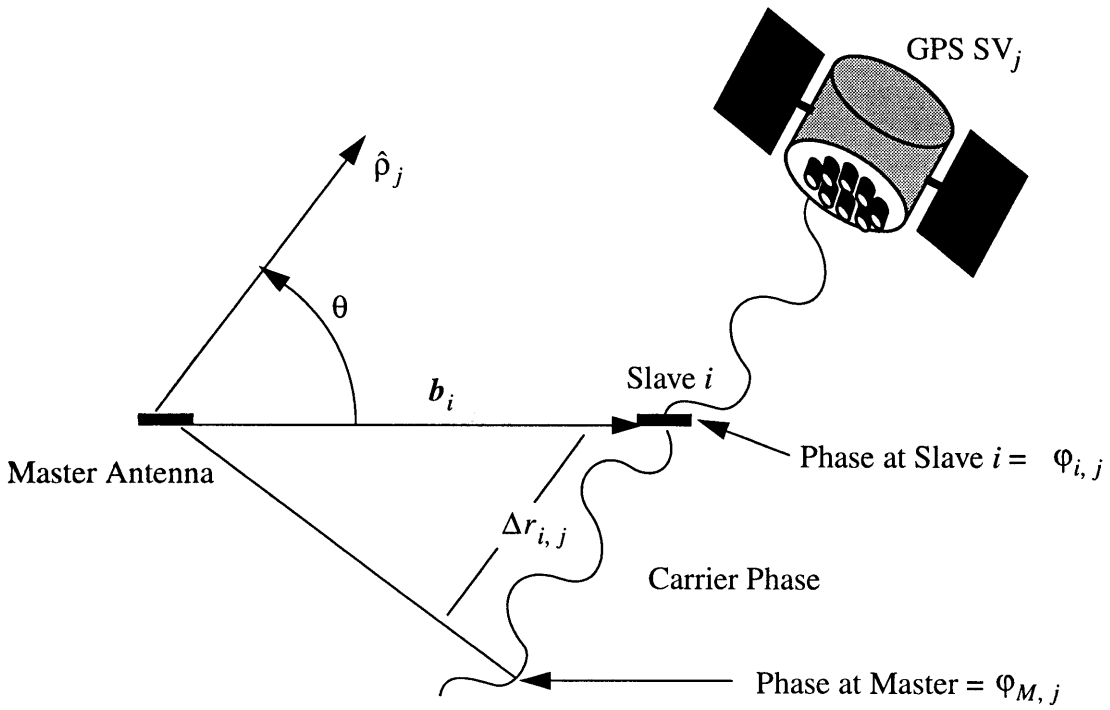

Figure 1.1: GPS Interferometric Theory

$\Delta r_{i,j}$, the relative range, is the projection of the baseline vector $\boldsymbol{b_i}$ onto the line-of-sight (LOS) vector $\hat{\rho}_j$ for the GPS SV on channel j:

$$\Delta r_{i,j} = \boldsymbol{b}_i^T \cdot \hat{\rho}_j = |\boldsymbol{b}_i| \cdot \cos(\theta) \qquad \textbf{(1.1)}$$

θ is the aspect angle between the $\boldsymbol{b_i}$ and $\hat{\rho}_j$. The primary observable for GPS interferometry is differential phase, $\Delta\varphi_{i,j}$, which is the difference between slave antenna carrier phase, $\varphi_{i,j}$, and master antenna carrier phase, $\varphi_{M,j}$. $\Delta\varphi_{i,j}$ differs from delta range by the integer ambiguity $\Delta k_{i,j}$,

which is some integer number of wavelengths of the GPS signal. The relationship between measured phase and differential range is:

$$\Delta r_{i,j} = \Delta\varphi_{i,j} + \Delta k_{i,j} - \varepsilon_{i,j} \tag{1.2}$$

where $\varepsilon_{i,j}$ are the errors in the received signal. These errors will be further discussed in Chapter 2. From equation 1.1 and 1.2 we can solve for the measurement equation:

$$\Delta\varphi_{i,j} = \boldsymbol{b}_i^T \cdot \hat{\rho}_j - \Delta k_{i,j} + \varepsilon_{i,j} \tag{1.3}$$

The method for determining $\Delta k_{i,j}$ used in this thesis is the decoupled and constrained ambiguity resolution method (DCAR) developed by Puri [20]. Additional information about IGPS theory is presented in Appendix C.

Hardware

The receiver, which collected all differential phase data used in the roof-top filter to be described in Chapter 4, is the Trimble TANS Vector GPS receiver. The Vector is a six-channel, four-antenna, C/A code receiver which outputs differential phase measurements at the rate of 1 Hz. The six channel tracking loops are time multiplexed across the four antennas. The receiver is connected to the four micro-strip patch antennas by coaxial cables. The patch antennas are mounted on Trimble-supplied 8-inch radius metallic ground planes to reduce susceptibility to multipath. Each ground plane is mounted on a 2 meter maximum length adjustable antenna array. This array was set at a 0.6 m per side configuration, yielding a total of three baselines from the master antenna: two 60 cm baselines and one 84 cm baseline across the diagonal. The array was mounted on a 2-axis turntable on the roof of the Draper Lab building. The phase data was collected and stored using a laptop computer which was connected to the receiver. The following picture illustrates the IGPS hardware.

Figure 1.2: IGPS Data Collection Hardware

1.2.2 MM Gyro

The development of micro-mechanical tuning fork gyros is the subject of current research and development at the C.S. Draper Laboratory. The low power consumption and compact size of these gyros make them ideal for satellite application.

Theory and Hardware

The basic operational concept of the MM tuning fork gyro is the sensing of a coriolis force. Two proof masses vibrate in opposing motion perpendicular to the axis the gyro is trying to measure. The Coriolis effect is described by

$$\underline{a} = 2\underline{\omega} \times \underline{V} \tag{1.4}$$

where $\underline{a}$ is the acceleration of mass with respect to the inertial frame, $\underline{\omega}$ is the angular rate of the gyro frame and $\underline{V}$ is the linear velocity of mass with respect to the gyro frame. The following figure shows the general description of the sensor:

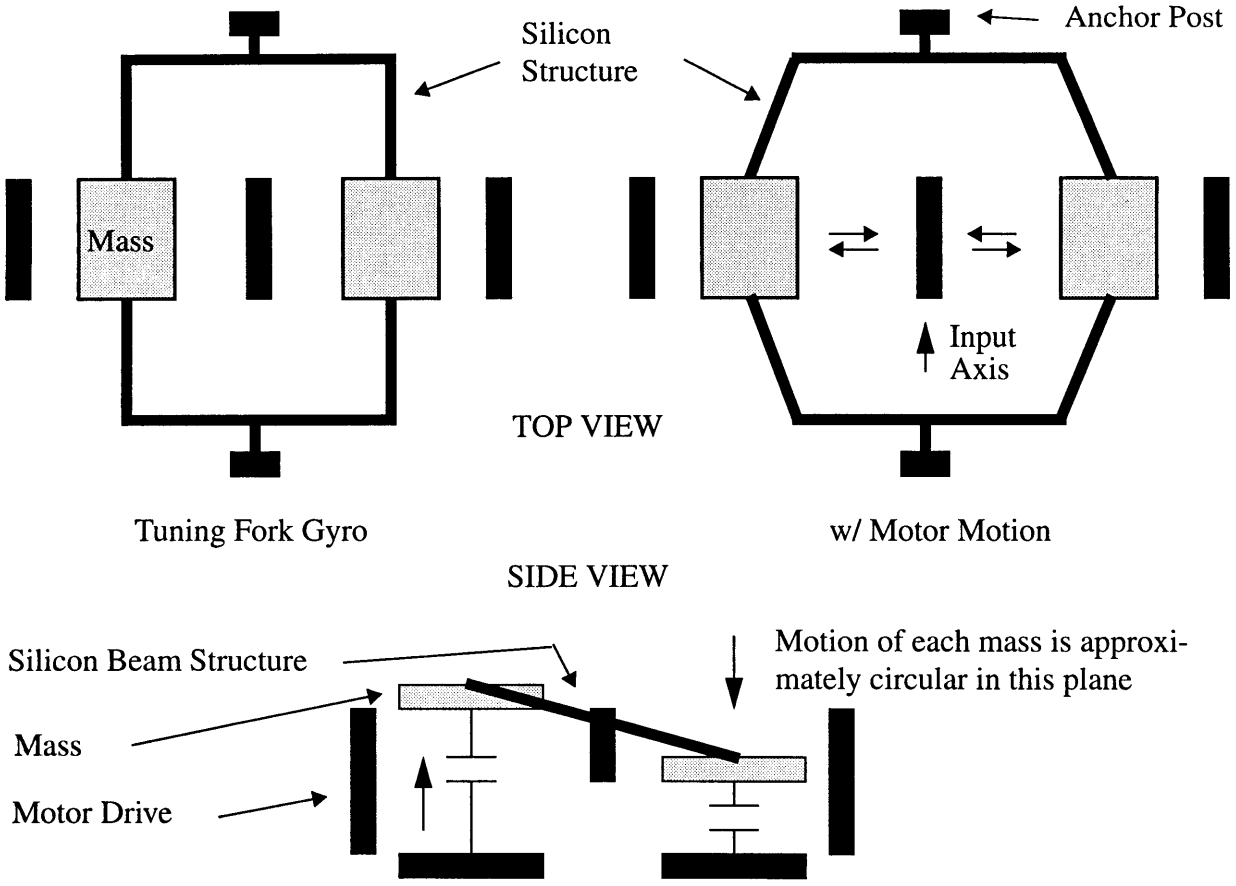

Figure 1.3: Illustration of MM Gyro Dynamics

The tuning fork gyro consists of a silicon structure suspended above a glass substrate containing metallization deposited for sensor interfacing. It is this silicon structure that suspends the two masses by a sequence of beams anchored at specific points in the substrate. The motor-drives force the two masses in lateral, in-plane oscillatory motion. An angular rate, ω, applied about the input axis, perpendicular to the velocity vector of the masses, generates a Coriolis force that acts to push the masses in and out of the plane of oscillation. Since the velocity vectors of the masses are in the plane of, and orthogonal to, the input axis; perpendicular motion orthogonal to the plane is induced in response to the Coriolis force. The resultant motion is measured by capacitor plates under each of the two masses, providing a signal proportional to the rate input. The gyro element

itself is very small, measuring about 2 mm on a side. A magnified picture of the MM Gyro is shown in Figure 1.4.

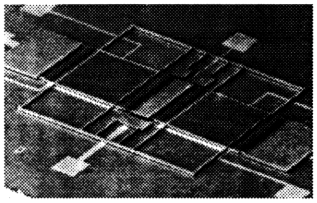

Figure 1.4: Micro-Mechanical Tuning Fork Gyro

The bulk of the size and complexity of the MM gyros actually comes from the electronics, which are an integral part of the gyro system. The electronics implement the control loops that drive the gyro and measure its out of plane motion. All the electronics are done in Application Specific Integrated Circuits (ASICs) using Complementary Metal-Oxide Semiconductor (CMOS) processes which allow for the entire gyro package to be approximately 1 cm X 1 cm in area and a few millimeters thick [12]

Figure 1.5 is a magnified picture of the MM Gyro and ASICs assembly. It measures approximately one centimeter on each side.

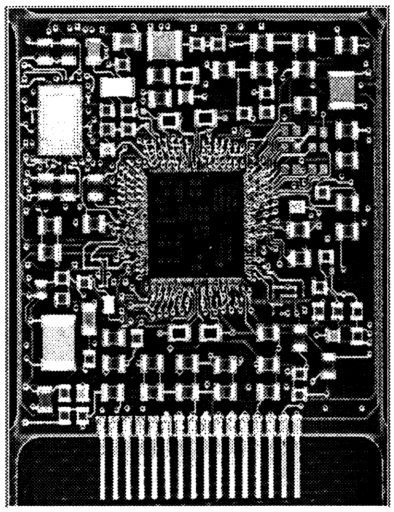

Figure 1.5: MM Gyro and ASICs

Chapter 2

Error Modeling

2.1 Introduction

The performance of the Extended Kalman Filter that combines MM gyro measurements with the IGPS measurements inherently depends on the correct modeling of the system errors. This chapter presents models of the IGPS and MM gyro measurement errors that will be used in the Kalman filter design. These models are a continuation of the work already done in IGPS/MM Gyro attitude determination at the Charles Stark Draper Laboratory. The first section of this chapter provides models for the error sources in the GPS differential phase measurements. The second section gives a standard model for the error sources inherent in a strapdown gyro.

2.2 GPS Differential Phase Error

This section summarizes the models used to characterize the errors present in GPS differential phase measurements. Although many models have been presented in the literature, the models used here are consistent with those developed by Puri [20] at Draper Laboratory. The emphasis of this study is integration issues; hence, the models already developed were deemed sufficient for the analysis.

2.2.1 Overview

Errors in the GPS differential phase measurements can directly affect attitude accuracy. A brief description of the sources of these errors follows. The mathematical models will be

presented in the next section.

Line Bias

The L1 carrier signal arrives at each patch antenna and travels to the Receiver Processing Unit (RPU) along four separate coaxial cables. Line bias error, denoted by $\Delta\beta$, is any phase delay caused by cable path length variations from the antenna to the receiver. The bias caused by this delay can vary since the path lengths may change with temperature variations of the system. The coaxial cables are designed to be as close to the same length as possible. Assuming the cables are positioned close to each other, any thermal variations which affect one cable should affect the others in a similar fashion since attitude is determined by phase differences. Thus close proximity of cables, one to another, should help to minimize line bias error.

Baseline Length Error

The attitude solution accuracy is limited by the knowledge of the baseline vectors (from master to slave antennas) that define the vehicle orientation. The baseline vector is subject to vehicle flexure, expansion and contraction. On a spacecraft, for example, one source of flexure would be thermal stresses experienced when passing in and out of eclipse. Baseline expansions are kept small by placing the IGPS array on a rigid platform no more than one meter apart. This error is modeled in this study only for the orbital simulations and not for analysis performed on the roof-top. Roof-top temperature variations were not great enough justify such modeling. Baseline length error will be denoted by δb.

Multipath

One of the largest and most troublesome causes of error in GPS interferometry is multipath. Multipath is any undesired signal reflection that interferes with the direct signal.

Since the reflected signal travels a longer path, its phase is shifted from that of the direct signal. Ways of mitigating multipath include limiting any reflectors in the vicinity of the antennas and using ground planes under each patch antenna. Once multipath has already corrupted the signal, there are ways to compensate for the repeatable part of the error caused by static sources such as body-fixed reflectors. Cohen and Parkinson [6] have demonstrated cancellation of low frequency multipath by developing a spherical harmonic model from experimental data. A similar fifth order model, developed by Puri, to match the Draper roof-top environment will be used in this study. The multipath dynamics not captured in this bias map will be modeled by augmenting the receiver correlated noise model. Multipath is not expected to be as great a problem on the spacecraft as on the Draper roof. Total multipath error will be denoted by Δm.

Antenna Phase Center Variations

Asymmetry of the dielectric substrate of the antenna which captures the L1 signal can lead to apparent movement of the phase center [24]. This variation is a function of the incidence angle of the incoming signal. Since typical RMS variation of 2-4 mm can be caused by phase center variation on microstrip GPS antennas [24], it is important to calibrate and/or model this error. Phase center variation, Δp, is body fixed and time invariant, however, it is antenna specific. These characteristics allow it to be modeled, along with low frequency multipath, in the calibration model mentioned above. Any mismodeling of the phase center by the bias map will be accounted for by augmenting the receiver correlated noise model, in accordance with analysis done previously [20].

Receiver Noise

The incoming carrier phase is corrupted by errors induced by the receiver itself. In this

analysis the receiver noise is broken down into two constituent parts: receiver white noise, Δv; and receiver correlated noise, $\Delta\xi$. The white noise model captures all of the uncorrelated errors such as thermal noise and oscillator noise [17]. Receiver correlated noise models any temporally correlated errors in the receiver. It is also used to absorb mismodeling in the multipath and phase center error calibration [20].

The following sections present models for line bias, baseline length error, multipath, phase center variation, and receiver noise. They are all in accordance with [20].

2.2.2 Line Bias Error Model

The single difference operator subtracts the line bias of each of the slave antennas from the master antenna bias to yield the differential line bias, $\Delta\beta$:

$$\underline{\Delta\beta} = \begin{bmatrix}\Delta\beta_1\\ \Delta\beta_2\\ \Delta\beta_3\end{bmatrix} = \begin{bmatrix}1 & -1 & 0 & 0\\ 1 & 0 & -1 & 0\\ 1 & 0 & 0 & -1\end{bmatrix} \cdot \begin{bmatrix}\beta_M\\ \beta_1\\ \beta_2\\ \beta_3\end{bmatrix} \tag{2.1}$$

Since the line bias is dependent on the coaxial cables, the differential line bias is a function of the baseline and not the channel from which the measurement comes. Hence, only three line bias error states will be needed. A first order exponentially correlated error model is used to model line bias:

$$\frac{d}{dt}\underline{\Delta\beta} = -\frac{1}{\tau_{\Delta\beta}}(\underline{\Delta\beta} - \underline{\Delta\beta_0}) + w_{\Delta\beta}(t) \tag{2.2}$$

where $\tau_{\Delta\beta}$ is the time constant and $w_{\Delta\beta}$ is zero mean white Gaussian process noise. The nominal line bias, $\underline{\Delta\beta_0}$, is calibrated before estimation [20]. The time constant depends on the receiver environment and is modeled as half the orbital period for the orbital simula-

tion that will be discussed later and 12 hours for the roof-top configuration. The driving noise strength is a function of the steady state line bias covariance, $\sigma_{\Delta\beta}$,

$$\sigma^2_{w_{\Delta\beta}} = \frac{2 \cdot \sigma^2_{\Delta\beta}}{\tau_{\Delta\beta}} \tag{2.3}$$

and since it is a product of the single difference operator, it is correlated between antennas. The correlations are added as shown below for a single channel and three baselines:

$$\mathbf{Q}_{\Delta\beta} = \begin{bmatrix} 1 & 0.5 & 0.5 \\ 0.5 & 1 & 0.5 \\ 0.5 & 0.5 & 1 \end{bmatrix} \cdot \sigma^2_{w_{\Delta\beta}} \tag{2.4}$$

where $\mathbf{Q}_{\Delta\beta}$ is the process noise covariance. The line bias steady state covariance, $\sigma_{\Delta\beta}$, is the value that needs to be determined and the method for so doing is described in detail in reference [20].

2.2.3 Baseline Length Error Modeling

It is assumed that the flexure of the IGPS array will be limited to expansions and contractions of the baselines due to thermal variations of the environment. Another first order Markov process will be used to model the baseline error dynamics:

$$\frac{d}{dt}(\underline{\delta b}) = -\frac{1}{\tau_b}\underline{\delta b} + w_b(t) \tag{2.5}$$

with driving noise strength:

$$\sigma^2_{w_b} = \frac{2 \cdot \sigma^2_b}{\tau_b} \tag{2.6}$$

The baseline length error, δb, enters the differential phase as a function of geometry and the resulting differential phase error due to δb is presented here without derivation [20]:

$$\varepsilon_{b_{i,j}} = (\boldsymbol{u}_{b_i}^T \cdot \hat{\rho}_j)\delta b_i \tag{2.7}$$

where i is the baseline and j is the channel as explained in chapter 1, and $\boldsymbol{u}_b$ is the unit vector for a nominal baseline.

2.2.4 Multipath and Phase Center Error Modeling

As mentioned earlier, the deterministic errors produced by body fixed sources and phase center variation are basically time invariant and only a function of the GPS line of sight vector in the body frame. These errors can be compensated for by comparing the measured phase to the predicted phase for a static receiver. Puri developed a bias map similar to the spherical harmonic model developed by Cohen in which the sky was divided into partitions that individually contained corrections for that line of sight. However, only body-fixed multipath due to diffraction off the ground planes could be calibrated since the data collections required movement of the IGPS antenna array. Multipath sources on the roof of Draper Lab include cooling stacks, an aluminum shed, and a skylight from another building. The multipath might be a result of planar reflectors or multiple point reflectors. Any uncorrected multipath or mismodeled phase center variation is modeled by increasing the steady state covariance of the process noise in the receiver correlated error state model.

2.2.5 Receiver Noise

As stated earlier, the receiver noise has been separated into receiver white (wide band) noise and receiver correlated noise. For this study the differential phase wide band noise strength, $\sigma_{\Delta\nu}^2$, is experimentally characterized as a function of SV line of sight elevation in the body frame. The receiver measurement noise is also cross correlated via the single difference operator:

$$\mathbf{R}_{\Delta\nu} = \begin{bmatrix} \sigma^2_{\Delta\nu}(\theta_{\rho 1}) & 0.5\cdot\sigma^2_{\Delta\nu}(\theta_{\rho 1}) & 0 & 0 \\ 0.5\cdot\sigma^2_{\Delta\nu}(\theta_{\rho 1}) & \sigma^2_{\Delta\nu}(\theta_{\rho 1}) & 0 & 0 \\ 0 & 0 & \sigma^2_{\Delta\nu}(\theta_{\rho 2}) & 0.5\cdot\sigma^2_{\Delta\nu}(\theta_{\rho 2}) \\ 0 & 0 & 0.5\cdot\sigma^2_{\Delta\nu}(\theta_{\rho 2}) & \sigma^2_{\Delta\nu}(\theta_{\rho 2}) \end{bmatrix} \tag{2.8}$$

where θ_{ρ_1} is the elevation of the SV on channel 1 in the body frame, and the example is for two baselines and two satellites.

The time correlated errors in the receiver, as well as the multipath and phase center variation mismodeling mentioned above, are modeled with the receiver correlated noise parameter. A first order Markov process is used to model this error,

$$\frac{d}{dt}\underline{\Delta\xi}(t) = -\frac{1}{\tau_{\Delta\xi}}\underline{\Delta\xi}(t) + w_{\Delta\xi}(t) \tag{2.9}$$

where $\tau_{\Delta\xi}$ is the time constant and $w_{\Delta\xi}$ is white Gaussian process noise. The driving noise strength is:

$$\sigma^2_{w_{\Delta\xi}} = \frac{2\cdot\sigma_{\Delta\xi}(\theta_{\rho j})^2}{\tau_{\Delta\xi}(\theta_{\rho j})} \tag{2.10}$$

where the steady state covariance of $\Delta\xi$, $\sigma^2_{\Delta\xi}$, is a function of SV elevation in the body frame, θ_{ρ_j}. The process noise strength is again correlated across the baselines, as shown in this example for a single channel and three baselines:

$$\mathbf{Q}_{\Delta\xi} = \begin{bmatrix} 1 & 0.5 & 0.5 \\ 0.5 & 1 & 0.5 \\ 0.5 & 0.5 & 1 \end{bmatrix}\cdot\sigma^2_{w_{\Delta\xi}} \tag{2.11}$$

2.2.6 Differential Phase Sensitivities

The following equation expands the error term in equation 1.3 to include the above mod-

eled errors:

$$\Delta\varphi_{i,j} = \boldsymbol{b}_{i_0}^T \cdot \hat{\rho}_j - \Delta k_{i,j} + \Delta\beta_i + \varepsilon_{b_{i,j}} + \Delta m_{i,j} + \Delta p_{i,j} + \Delta v_{i,j} + \Delta\xi_{i,j} \tag{2.12}$$

With this equation we can determine the sensitivity of the differential phase measurement to each modeled error source. The sensitivities will be important when deriving the Kalman filter measurement sensitivity matrix in the next chapter. All the sensitivities are straight forward except for the baseline length error which is obtained by taking the derivative of equation 2.7. In the order discussed they are:

$$\frac{\partial\Delta\varphi_{i,j}}{\partial\Delta\beta_k} = \delta(i,k) \tag{2.13}$$

$$\frac{\partial\Delta\varphi_{i,j}}{\partial(\delta b_k)} = \delta(i,k)\cdot(\boldsymbol{u}_{b_j}^T \cdot \hat{\rho}_j^B) \tag{2.14}$$

$$\frac{\partial\Delta\varphi_{i,j}}{\partial\Delta m_{k,l}} = \delta(i,k)\delta(j,l) \tag{2.15}$$

$$\frac{\partial\Delta\varphi_{i,j}}{\partial\Delta p_{k,l}} = \delta(i,k)\delta(j,l) \tag{2.16}$$

$$\frac{\partial\Delta\varphi_{i,j}}{\partial\Delta v_{k,l}} = \delta(i,k)\delta(j,l) \tag{2.17}$$

$$\frac{d}{dt}\underline{\Delta\xi}(t) = -\frac{1}{\tau_{\Delta\xi}}\underline{\Delta\xi}(t) + w_{\Delta\xi}(t) \tag{2.18}$$

$$\tag{2.19}$$

2.3 MM Gyro Errors

The IGPS/MM Gyro ADS treats gyro system output as measurement inputs to the EKF to determine attitude and angular rate rather than as an instrument that determines body rate, as is normally done with ADS's with high quality gyros. These inputs are essential for the

model based 'tightly-coupled' filter design, alluded to earlier, and which will be formally explained in the next chapter. This type of integration is possible due to modeling of the dynamic forces such as the gravity gradient torque.

2.3.1 Overview

There are several sources of error that are inherent in all gyros and some that are particular to the MM gyros currently being developed at the Draper Lab. The typical sources of error are captured in the classical gyro model presented below. Other sources such as scale factor bias and misalignment error will be mentioned as will errors specific to the MM gyro.

2.3.2 Classic Gyro Error Model

The classic gyro error model is:

$$\underline{\omega}_M(t) = \underline{\omega}_T(t) + \boldsymbol{b}_g(t) + \boldsymbol{v}_g(t) \tag{2.20}$$

where $\underline{\omega}_M$ is the measured angular rate, $\underline{\omega}_T$ is the actual rate, $\boldsymbol{b}_g$ is a time varying bias, and $\boldsymbol{v}_g$ is the white measurement noise.

Angle Random Walk

The white noise, $\boldsymbol{v}_g$, is also known as drift rate noise or random drift rate noise. It is modeled with strength $\mathbf{R}_g$. It produces "angular random walk" (ARW), created by integrating the angular velocty, $\underline{\omega}_M$, over a short interval Δt. The variance of the error due to ARW is given by:

$$\sigma^2_{ARW} = \mathbf{R}_g \cdot \Delta t \tag{2.21}$$

where Δt is the integration step size or the inverse of the output rate. ARW get its name because the noise term integrates into "random walk" in the angle.

Gyro Bias

The gyro bias is a varying drift rate in the gyro that can cause considerable error when using low accuracy gyros for extended periods of time. One benefit of the IGPS/MM Gyro ADS is that the differential GPS phase measurements will constitute a way of periodically recalibrating this drift rate. The gyro bias, with units of angular rate, can be modeled either as a Markov process:

$$\frac{d}{dt}(b_g) = -\frac{1}{\tau_g}(b_g) + v_b \tag{2.22}$$

or by a simpler random walk model:

$$\frac{d}{dt}(b_g) = v_b \tag{2.23}$$

This study will use the model presented in equation 2.22. The strength of the bias noise is modeled by:

$$\sigma^2_{v_b} = \frac{2 \cdot \sigma^2_b}{\tau_g} \tag{2.24}$$

where σ^2_b is the variance of the gyro bias steady-state value and τ_g is the time constant associated with the bias dynamics.

2.3.3 Other Gyro Errors

In addition to the standard angle random walk and gyro bias errors, there are some other errors that can affect the quality of gyro output.

Scale Factor Error

Scale factor error arises when the calibration of the relationship between actual angular rate and gyro output is incorrect. The attitude error this causes is proportional to the prod-

uct of the net rotation angle with the scale factor error [21]. When real gyro data is used in this study, it will be assumed that scale factor error has either been calibrated out or is negligible.

Misalignment Error

Since strapdown gyro packages are literally strapped onto the body of the vehicle, a misalignment error can result if the transformation relating the gyro axes to body axes is not known perfectly. For this application, it will be assumed that the misalignment errors are either calibrated *a priori* or are small enough to be negligible. Body flexure is also assumed negligible.

Temperature Bias

The MM Gyros currently under development at the Draper Laboratory are very sensitive to temperature changes. In a space application vehicle electronics could easily see temperature fluctuations from $0^{o}C$ to $40^{o}C$ [14]. For this reason, the MM Gyro output must be temperature compensated. The temperature dependence of the MM Gyros is shown in Figure 2.1 for a 15 hour drift test:

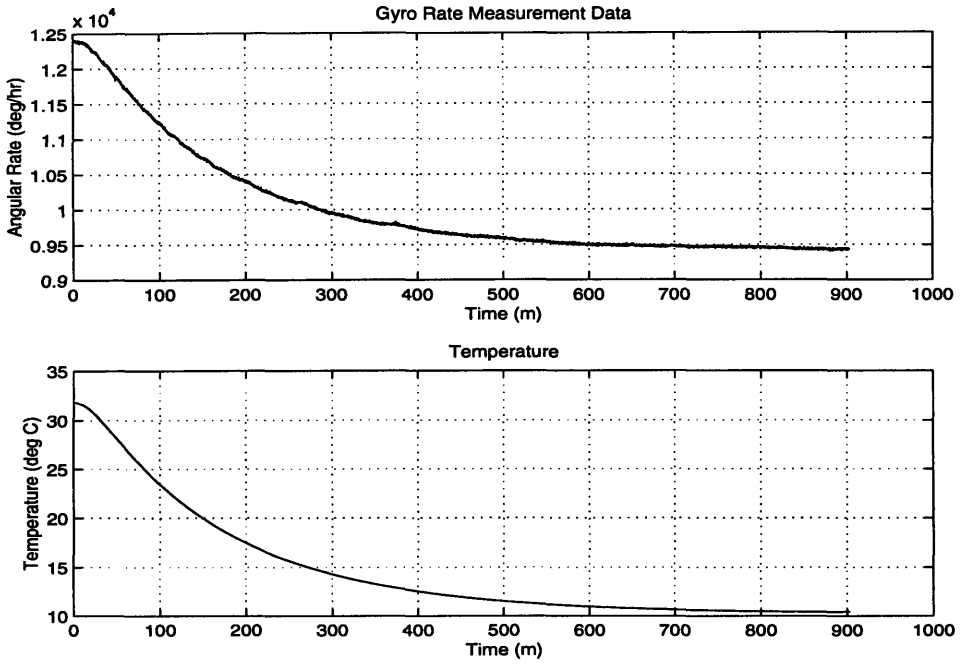

Figure 2.1: Raw MM Gyro Data

After applying temperature compensation, the resultant data is well characterized by the noise-induced bias model of Equation 2.2:

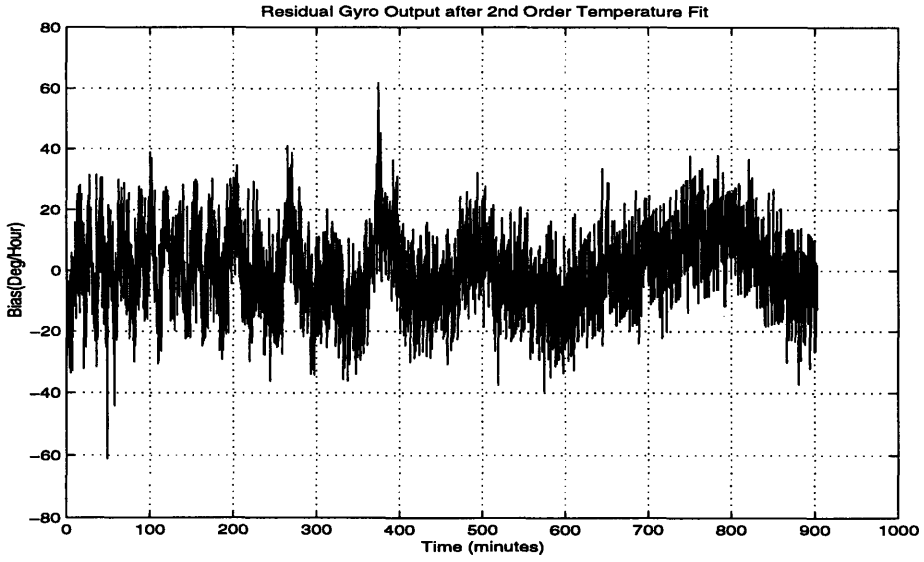

Figure 2.2: Temperature Compensated Gyro Data

When not using real data in this study, gyro measurements were created by simulation using the model of Equation 2.2.

Chapter 3

Filter Design

3.1 Introduction

The key to the tightly coupled integration of the IGPS/MM Gyro ADS is the Kalman filter. It combines gyro and GPS measurements to form an accurate attitude estimate. As mentioned in Chapter 1, this application requires an Extended Kalman filter (EKF) to deal with nonlinear dynamics and nonlinear measurement relationships. The nonlinear measurement relationships are a result of the motion of the GPS satellites that provide the phase measurements.

This chapter reviews the standard filter equations. The dynamics used in state propagation will be presented along with a formulation of the measurement relationships. The last part of the chapter will give a brief description of some of the implementation issues which must be addressed in the filter algorithms.

3.2 Filter Equations

A review of the Extended Kalman filter equations will be presented in the following sections. The quaternion formulation of the state, presented in Section 3.2.2, was first demonstrated by Lefferts, Markley, and Shuster [15] and has been successfully implemented by many researchers including some in the IGPS field [3, 20, 25]. Additional information on Kalman filtering theory can be obtained in Gelb [9] and [1].

3.2.1 Continuous-Discrete EKF

This application lends itself to a particular class of estimation problems in which the non-linear system has continuous dynamics and discrete-time measurements. The system dynamics are characterized by the continuous nonlinear state differential equation:

$$\dot{\boldsymbol{x}}(t) = \boldsymbol{f}(\boldsymbol{x}(t), t) + \boldsymbol{g}(\boldsymbol{x}(t), t)\boldsymbol{w}(t) \tag{3.1}$$

and measurements are characterized by the discrete-time nonlinear measurement equation:

$$z_k = \boldsymbol{h}(\boldsymbol{x}_k, t_k) + \boldsymbol{v}_k \tag{3.2}$$

where the subscript k refers to the measurement at time t_k. $\boldsymbol{w}(t)$ is a zero mean white Gaussian process noise with strength $\mathbf{Q}(t)$:

$$E[\boldsymbol{w}(t)\boldsymbol{w}(t-\tau)^T] = \mathbf{Q}(t)\delta(t-\tau) \tag{3.3}$$

where δ is the Dirac delta function with units of 1/time. $\boldsymbol{v}_k$ is discrete white Gaussian measurement noise with covariance $\mathbf{R}_k$:

$$E[\boldsymbol{v}_k \boldsymbol{v}_i^T] = \begin{cases} \mathbf{R}_k & i = k \\ \mathbf{0} & i \neq k \end{cases} \tag{3.4}$$

and it is assumed that there is no cross correlation between the measurement noise and the process noise:

$$E[\boldsymbol{w}(t)\boldsymbol{v}_k^T] = \mathbf{0} \text{ for all t and k.} \tag{3.5}$$

We define the error between the true state, $\boldsymbol{x}$, and the state estimate, $\hat{\boldsymbol{x}}$:

$$\tilde{\boldsymbol{x}} = \boldsymbol{x} - \hat{\boldsymbol{x}} \tag{3.6}$$

The error covariance matrix is defined as:

$$\mathbf{P} = E[(\tilde{\boldsymbol{x}})(\tilde{\boldsymbol{x}})^T] \tag{3.7}$$

If the functions of $\boldsymbol{f}$ and $\boldsymbol{g}$ are sufficiently well behaved, we can linearize the system about the state estimate at time t:

$$\mathbf{F}(t) \equiv \frac{\partial}{\partial \boldsymbol{x}} \boldsymbol{f}(\boldsymbol{x}(t), t)|_{\hat{\boldsymbol{x}}(t_-)} \tag{3.8}$$

$$\mathbf{G}(t) \equiv \frac{\partial}{\partial \boldsymbol{x}} \boldsymbol{g}(\boldsymbol{x}(t), t)|_{\hat{\boldsymbol{x}}(t_-)} \tag{3.9}$$

yielding the linearized dynamics,

$$\dot{\tilde{\boldsymbol{x}}}(t) = \mathbf{F}(t)\tilde{\boldsymbol{x}}(t) + \mathbf{G}(t)\boldsymbol{w}(t) \tag{3.10}$$

The minus and plus subscripts denote the state estimates before and after measurement updates, respectively. A predicted measurement at time t_k can be formulated by using the state estimate and the nonlinear measurement equation:

$$\hat{\boldsymbol{z}}_k = \boldsymbol{h}(\hat{\boldsymbol{x}}_{k-}, t_k) \tag{3.11}$$

Now the measurement residual is:

$$\tilde{\boldsymbol{z}}_k = \boldsymbol{z}_k - \hat{\boldsymbol{z}}_k \tag{3.12}$$

which can be related to the state error vector, $\tilde{\boldsymbol{x}}$, by the following linearized sensitivity matrix, $\mathbf{H}_k$:

$$\tilde{\boldsymbol{z}}_k = \mathbf{H}_k\tilde{\boldsymbol{x}}_k + \boldsymbol{v}_k \tag{3.13}$$

where $\mathbf{H}_k$ is defined by,

$$\mathbf{H}_k = \left.\frac{\partial \tilde{\boldsymbol{z}}_k}{\partial \boldsymbol{x}}\right|_{\hat{\boldsymbol{x}}_{k-}} \tag{3.14}$$

We can incorporate the measurements to form the optimal state correction as a function of the residual and the Kalman gain, $\boldsymbol{K}_k$:

$$\hat{\boldsymbol{x}}_{k+} = (\hat{\boldsymbol{x}}_{k-} + \mathbf{K}_k\tilde{\boldsymbol{z}}_k) \tag{3.15}$$

and the updated covariance matrix shown in the Joseph form:

$$\mathbf{P}_{k+} = (1 - \mathbf{K}_k\mathbf{H}_k)\mathbf{P}_{k-}\ (1 - \mathbf{K}_k\mathbf{H}_k)^T + \mathbf{K}_k\mathbf{R}_k\mathbf{K}_k^T \tag{3.16}$$

This above form is used to ensure symmetry, where

$$\mathbf{P}_{k+} = E[(\tilde{\boldsymbol{x}}_{k+})(\tilde{\boldsymbol{x}}_{k+})^T] \tag{3.17}$$

and

$$\mathbf{K}_k = \mathbf{P}_{k-}\,\mathbf{H}_k^T(\mathbf{H}_k\mathbf{P}_{k-}\,\mathbf{H}_k^T + \mathbf{R}_k)^{-1} \tag{3.18}$$

After a measurement update, the state is propagated to the next time increment t_{k+1} through the nonlinear dynamics:

$$\dot{\hat{\boldsymbol{x}}}(t) = f(\hat{\boldsymbol{x}}(t), t) \tag{3.19}$$

The error covariance matrix is propagated via the discrete solution of the continuous time matrix Ricatti equation:

$$\dot{\mathbf{P}} = \mathbf{FP} + \mathbf{PF}^T + \mathbf{GQG}^T \tag{3.20}$$

which has the solution,

$$\mathbf{P}_{(k+1)-} = \Phi_{k+1,k}\,\mathbf{P}_{k+}\,\Phi_{k+1,k}^T + \tilde{\mathbf{Q}}(t_{k+1,k}) \tag{3.21}$$

where Φ is the state transition matrix, and $\tilde{\mathbf{Q}}$ is the process noise dynamics both defined below:

$$\Phi(t_{k+1}, t_k) = \int_{t_k}^{t_{k+1}} \mathbf{F}(\tau)\Phi(\tau, t_k)d\tau \tag{3.22}$$

$$\Phi(t_k, t_k) = \mathbf{1} \tag{3.23}$$

$$\tilde{\mathbf{Q}}(t_{k+1}, t_k) = \int_{t_k}^{t_{k+1}} \Phi_\tau \mathbf{G}(\tau)\mathbf{Q}(\tau)\mathbf{G}(\tau)^T\Phi_\tau d\tau \tag{3.24}$$

where $\mathbf{1}$ is an identity matrix of appropriate size. For short time steps these equations can be approximated to first order by:

$$\Phi(t_{k+1}, t_k) = (\mathbf{1} + \mathbf{F}\Delta t) \tag{3.25}$$

$$\tilde{\mathbf{Q}}(t_{k+1}, t_k) = \mathbf{G}[\mathbf{Q}\Delta t]\mathbf{G}^T \tag{3.26}$$

where

$$\Delta t = t_{k+1} - t_k \tag{3.27}$$

3.2.2 Choosing the State

A critical step in designing a Kalman filter is deciding what states to incorporate in the system dynamics. The states of interest need to be modeled, as well the errors that affect those states. However, too much complexity in the modeling can also unnecessarily burden the filter.

Reference Frames

Since attitude information is the goal of this system, there must be some state representation of vehicle attitude. The vehicle orientation with respect to the navigation frame (nav frame) is of primary interest. The body frame will be represented with the subscript B while the nav frame will be denoted with an N. The nav frame used for this application is the Local Vertical Local Horizontal (LVLH) frame. This frame is constructed with the X axis pointed in the velocity direction, the Z axis toward nadir and the Y axis out of plane. Two other reference frames important in this study are the Earth-Centered-Earth-Fixed (E) frame and the Inertial (I) reference frame. The E frame is the frame in which the GPS SV positions are reported. It has its X axis in the equatorial plane pointing toward the Greenwich Meridian, its Z axis aligned approximately with the Earth's spin axis, and the Y axis completes the right-handed triad [23]. The I frame, for short time periods, can be defined as the E frame minus the Earth's rotation about the Z axis. The following figure summarizes the above descriptions. Note that the only rotation between the body frame and nav frame is a yaw rotation.

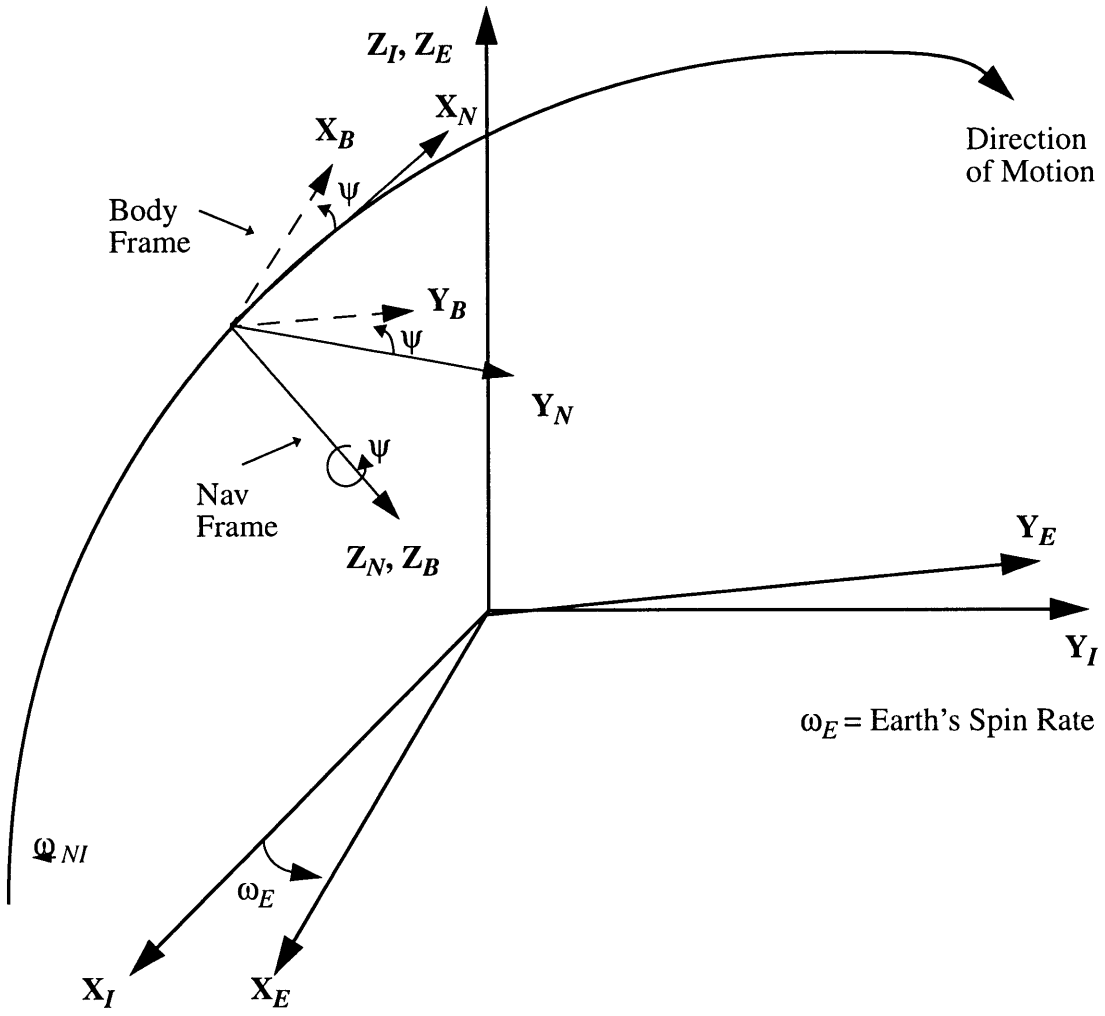

Figure 3.1: Summary of Reference Frames

Attitude State

As mentioned, the attitude state is of fundamental importance in this study. There are various methods of representing the vehicle body with respect to the nav frame. The most common representation is through the actual physical angles, known as Euler angles, between the nav and body frames. The disadvantages of this method, however, include singularities and burdensome trigonometric terms. Another very common method used in many applications is the direction cosine matrix. Although it eliminates these problems, it

contains nine parameters, some of which are redundant. For this application the quaternion representation of the attitude, which overcomes these disadvantages, will be adopted.

The benefits of the quaternion attitude representation have been known and applied since Hamilton first developed it more than 150 years ago. However, its use in Kalman filtering has had some difficulty due to the constraint that the four quaternion parameters have unit norm which results in the singularity of the attitude portion of the covariance matrix. Lefferts, Markley and Shuster were able to overcome this problem, and the use of quaternion attitude representation in filtering applications has become more commonplace in the last 15 years. For more information on this subject see [15].

The quaternion, $\underline{q}$, is defined by four parameters which represent some rotation Φ about an axis of rotation, $\hat{e}$:

$$\underline{q} = \begin{bmatrix} \hat{e} \cdot \sin\left(\frac{\Phi}{2}\right) \\ \cos\left(\frac{\Phi}{2}\right) \end{bmatrix} = \begin{bmatrix} q_1 \\ q_2 \\ q_3 \\ q_4 \end{bmatrix} = \begin{bmatrix} \boldsymbol{q} \\ q_4 \end{bmatrix} \tag{3.28}$$

where $\boldsymbol{q}$ is the vector part of the quaternion, and q_4 is the scalar portion. The four quaternion parameters satisfy the aforementioned constraint:

$$q_1^2 + q_2^2 + q_3^2 + q_4^2 = 1 \tag{3.29}$$

As stated previously in the beginning of the chapter in section 3.2, we wish the filter to keep track of the best estimate of the difference between the true attitude and the estimated attitude. Equivalently, we can say we want to keep track of the estimation error between the nav and body frame, i.e.,

$$\boldsymbol{C}_{BN} = \boldsymbol{C}_{B\hat{B}}\boldsymbol{C}_{\hat{B}N} \tag{3.30}$$

where $\boldsymbol{C}_{B\hat{B}}$ can also be viewed as the error in rotation from nav to body, or $\tilde{\boldsymbol{C}}_{BN}$. This

error can be expressed through small Euler angle rotations from the body as

$$\tilde{C}_{BN} \approx [\mathbf{1} + [\delta\underline{\Theta}]_X] \tag{3.31}$$

where $[\delta\underline{\Theta}]_X$ is the vector of the small Euler angles in cross-product form:

$$[\delta\underline{\Theta}]_X = \begin{bmatrix} 0 & \psi & -\theta \\ -\psi & 0 & \varphi \\ \theta & -\varphi & 0 \end{bmatrix} \tag{3.32}$$

and ψ, θ, and ϕ are the small Euler yaw, pitch, and roll angles, respectively. The small angle error vector is related to the quaternion by

$$\delta\underline{q} = \frac{1}{2}\delta\underline{\Theta} \tag{3.33}$$

where

$$\delta\underline{q} = (\underline{q} \otimes \hat{\underline{q}}^{-1}) \tag{3.34}$$

and $\underline{q}$ represents the true attitude state, while $\hat{\underline{q}}$ represents the estimated attitude state. $\otimes$ is the quaternion operator described by

$$\underline{q} \otimes \hat{\underline{q}} = \begin{bmatrix} q_4' & q_3' & -q_2' & q_1' \\ -q_3' & q_4' & q_1' & q_2' \\ q_2' & -q_1' & q_4' & q_3' \\ -q_1' & -q_2' & -q_3' & q_4' \end{bmatrix} \begin{bmatrix} \hat{q}_1 \\ \hat{q}_2 \\ \hat{q}_3 \\ \hat{q}_4 \end{bmatrix} \tag{3.35}$$

$\hat{\underline{q}}^{-1}$ is the quaternion inverse operator:

$$\hat{\underline{q}}^{-1} = \begin{bmatrix} -\hat{\underline{q}} \\ q_4 \end{bmatrix} \tag{3.36}$$

Finally, the attitude state, $\delta\underline{q}_{BN}^{B}$, is the error quaternion from nav to body frame expressed in body coordinates. The omission of the scalar part of the quaternion is in accordance with [15].

Model Replacement State

As mentioned previously in section 2.3, due to the quality of the low cost gyros, the traditional "model replacement" mode is not used in this application. Instead they are used as any other measurement with appropriate intensities and sensitivities. This "gyro replacement" mode requires the incorporation of a state to capture the modeled dynamics. For this reason the dynamic modeling state, the attitude rate error state, is included in the filter design.

The angular rate error is defined as:

$$\delta\underline{\omega}_{BN}^{B} = \underline{\omega}_{BN}^{B} - \hat{\underline{\omega}}_{BN}^{B} \tag{3.37}$$

which is the difference between the true and estimated rate. This state will play an important role in state propagation which will be needed to form the predicted state. The dynamics of this state, largely influenced by the gravity gradient torque for space applications, will be provided in section 3.3.

Other States

The rest of the states serve to model the errors of the previous chapter. The total states of the filter depend on the type of environment the filter is used. The baseline error state is omitted for the roof-top filter. Also, no disturbance torque state is included following the sub-optimal analysis performed by Puri [20]. The only disturbance torque modeled is the inclusion of gravity gradient affects on the dynamics in the space filter. The total state matrix then is:

$$\boldsymbol{x} = \left[\delta\mathbf{q}_{BN}^{B}\ \delta\underline{\omega}_{BN}^{B}\ \boldsymbol{b}_{g}\ \underline{\Delta\beta}\ \underline{\Delta\xi}\ (\underline{\delta b})\right]^{T} \tag{3.38}$$

3.3 State Dynamics

The dynamics of the modeled system will be used to propagate the state. First the non-linear dynamics will be presented. The second sub-section describes the linearized dynamics of the Extended Kalman filter.

3.3.1 Non-Linear Dynamics

Attitude

The rate of change of a quaternion can be found to be:

$$\frac{d}{dt}\underline{q}(t) = \frac{1}{2}(\underline{\omega}(t) \otimes \underline{q}(t)) \tag{3.39}$$

This equation can be used to express the attitude kinematics by separating the angular velocity into two components: the angular velocity of the body with respect to the inertial frame and the rate of the body with respect to the nav frame:

$$\frac{d}{dt}\underline{q}^B_{BN} = \frac{1}{2}\underline{\omega}^B_{BI} \otimes \underline{q}^B_{BN} - \frac{1}{2}\underline{q}^B_{BN} \otimes \underline{\omega}^B_{NI} \tag{3.40}$$

which can be more conveniently written as the extension of equation 3.37:

$$\frac{d}{dt}\underline{q}^B_{BN} = \frac{1}{2}\underline{\omega}^B_{BN} \otimes \underline{q}^B_{BN} \tag{3.41}$$

due to the relation

$$\underline{\omega}_{BI} = \underline{\omega}_{BN} + \underline{\omega}_{NI} \tag{3.42}$$

The dynamics of the attitude error are obtained by manipulation of equations 3.35, 3.38, and 3.40 to yield the following for the vector part of the quaternion [4, 15, 25]:

$$\frac{d}{dt}\delta\boldsymbol{q}^B_{BN} = [\underline{\omega}^B_{BN}]_X \delta\boldsymbol{q}^B_{BN} + \frac{1}{2}\delta\underline{\omega}^B_{BN} \tag{3.43}$$

Attitude Rate

The derivation of the attitude error rate dynamics is somewhat more involved. In the inter-

est of clarity, the non-linear equation for angular rate error will be presented without derivation. For a derivation of the following equations see Appendix A. The equation is:

$$\frac{d}{dt}(\delta\underline{\omega}^B_{BN}) = I^{-1}[6\underline{\omega}^2{}_{NI}([\hat{r}_X]I - [I\hat{r}]_X)[\hat{r}_X]]\delta\mathbf{q}^B_{BN} \tag{3.44}$$
$$+ I^{-1}([I\hat{\underline{\omega}}^B_{BI}]_X - [\hat{\underline{\omega}}^B_{BI} \times I])(\delta\underline{\omega}^B_{BN} + \delta\underline{\omega}^B_{NI}) - \delta\underline{\omega}^B_{NI} \times \delta\underline{\omega}^B_{BN}$$

This equation contains the dynamic modeling that will aid the filter in attitude extrapolation.

3.3.2 Linearized Dynamics

The non-linear attitude error states

$$\tilde{x}_1 = \left[\delta\mathbf{q}^B_{BN}\ \delta\underline{\omega}^B_{BN}\right] \tag{3.45}$$

have the dynamics presented in equations 3.43 and 3.44. The linearized dynamics matrix in the Extended Kalman filter will be formed by partial differentiation of the nonlinear equations with respect to each state:

$$F_1 = \begin{bmatrix} A & B \\ C & D \end{bmatrix} \tag{3.46}$$

where

$$A = \frac{\partial}{\partial\delta q^B_{BN}}\delta\dot{q}^B_{BN} = [\hat{\underline{\omega}}^B_{BN}]_X \tag{3.47}$$

$$B = \frac{\partial}{\partial\delta\underline{\omega}^B_{BN}}\delta\dot{q}^B_{BN} = \frac{1}{2}(\mathbf{1}_{3\times3}) \tag{3.48}$$

$$C = \frac{\partial}{\partial\delta q^B_{BN}}\delta\dot{\underline{\omega}}^B_{BN} = I^{-1}[6\omega^2{}_{NI}([\hat{r}_X]I - [I\hat{r}]_X)[\hat{r}_X]] \tag{3.49}$$

$$D = \frac{\partial}{\partial\delta\underline{\omega}^B_{BN}}\delta\dot{\underline{\omega}}^B_{BN} = I^{-1}([I\hat{\underline{\omega}}^B_{BI}]_X - [\hat{\underline{\omega}}^B_{BI}]_X I) - [\delta\underline{\omega}^B_{NI}]_X \tag{3.50}$$

The other states, which are the gyro and GPS error states,

$$\tilde{x}_2 = \left[b_g \ \underline{\Delta\beta} \ \underline{\Delta\xi} \ (\underline{\delta b})\right]^T \tag{3.51}$$

are governed by their respective dynamics:

$$\mathbf{F}_2 = \begin{bmatrix} \left(-\frac{1}{\tau_{b_g}}\right)\mathbf{1}_{3x3} & 0 & 0 & 0 \\ 0 & \left(-\frac{1}{\tau_{\Delta\beta}}\right)\mathbf{1}_{3x3} & 0 & 0 \\ 0 & 0 & \begin{bmatrix} \left(-\frac{1}{\tau_{\Delta\xi_1}}\right)\mathbf{1}_{3X3} & \mathbf{0} \\ \cdots & \\ \mathbf{0} & \left(-\frac{1}{\tau_{\Delta\xi_6}}\right)\mathbf{1}_{3x3} \end{bmatrix} & 0 \\ 0 & 0 & 0 & \left\{\left(-\frac{1}{\tau_{\delta b}}\right)\mathbf{1}_{3x3}\right\} \end{bmatrix} \tag{3.52}$$

The process noise follows the same formulation:

$$w_1 = \left[\mathbf{0}_{1x3} \ (w_{\delta\omega})\right]^T \tag{3.53}$$

$$w_2 = \left[w_{b_g} \ w_{\Delta\beta} \ w_{\Delta\xi} \ (w_{\delta b})\right]^T \tag{3.54}$$

with

$$\mathbf{G}_1 = \begin{bmatrix} \mathbf{0} \\ (I^{-1}) \end{bmatrix} \tag{3.55}$$

$$\mathbf{G}_2 = \begin{bmatrix} \mathbf{1}_{3x3} & \mathbf{0} & \mathbf{0} & \mathbf{0} & \mathbf{0} \\ \mathbf{0} & \mathbf{1}_{3x3} & \mathbf{0} & \mathbf{0} & \mathbf{0} \\ \mathbf{0} & \mathbf{0} & \mathbf{1}_{18x18} & \mathbf{0} & \mathbf{0} \\ \mathbf{0} & \mathbf{0} & \mathbf{0} & \mathbf{1}_{3x3} & \mathbf{0} \\ \mathbf{0} & \mathbf{0} & \mathbf{0} & \mathbf{0} & \mathbf{1}_{3x3} \end{bmatrix} \tag{3.56}$$

The reason the attitude rate error process noise is in parenthesis is because the noise is only added for the space filter. The parenthesis around the baseline length error process noise serves to indicate that this state is also only modeled in the space filter. It is assumed that the dynamics of the roof-top filter are fairly well known, whereas mismodeling orbital dynamics is much more likely, especially in the presence of disturbance torques. Finally, the total dynamics are:

$$\dot{\tilde{x}}_1 = \mathbf{F}_1\tilde{x} + \mathbf{G}_1 w_1 \tag{3.57}$$

$$\dot{\tilde{x}}_2 = \mathbf{F}_2\tilde{x}_2 + \mathbf{G}_2 w_2 \tag{3.58}$$

3.4 Measurement Prediction and Sensitivities

The key to maximizing the benefit that measurements provide to attitude estimation in Kalman filtering lies in the fidelity of the measurement model. Better measurement models will provide better sensitivities which will result in more optimal filter gains to bring the state closer to truth. Recall that the optimal gain correction applied by the filter is based on the measurement sensitivity matrix:

$$\mathbf{H}_k = \left.\frac{\partial \tilde{z}_k}{\partial x}\right|_{\hat{x}_{k-}} \tag{3.14}$$

The first sub-section will present the GPS measurement prediction and sensitivities. The second section will derive the gyro measurement prediction and sensitivities.

3.4.1 GPS Measurement Prediction and Sensitivities

The GPS measurement prediction and sensitivities have been described in detail in [20]. They are summarized here for convenience. To create the GPS measurement residual,

$$\tilde{z}_{k_{GPS}} = \underline{\Delta\varphi}(t_k) - \underline{\hat{\Delta\varphi}}(t_{k-}) \tag{3.59}$$

the predicted phase is formulated by applying the following equation:

$$\Delta\hat{\varphi}_{i,j} = (\boldsymbol{b}_{i_0}^{B})^{T}[\hat{\rho}_{j,est}^{B}] - \Delta\hat{k}_{ij} + \hat{\varepsilon}_{ij} \tag{3.60}$$

The integer ambiguity, $\Delta\hat{k}_{ij}$, is predicted with the integer ambiguity resolver mentioned in Chapter 1. The predicted error, $\hat{\varepsilon}_{ij}$, and the estimated LOS vector, $\hat{\rho}_{j,est}^{B}$, are formulated in [20] but their definitions are summarized with the following two equations:

$$\Delta\hat{\varepsilon}_{ij} = \chi([\hat{\rho}_{j,est}^{B}], i) + \Delta\hat{\beta}_i + \Delta\hat{\xi}_{i,j} + (\boldsymbol{u}_{b_i}^{T} \cdot [\hat{\rho}_{j,est}^{B}])\delta\hat{b}_i \tag{3.61}$$

$$[\hat{\rho}_{j,est}^{B}] = {}^{B}\hat{\boldsymbol{C}}^{N} \cdot \hat{\rho}_{j}^{N} \tag{3.62}$$

χ is the calibration from the bias map described in Chapter 2. Following the derivation in [20], the sensitivity of the GPS measurement residual to the attitude state is:

$$\frac{\partial\tilde{z}_{i,j}}{\partial\delta\mathbf{q}_{BN}^{B}} = 2 \cdot [\hat{\rho}_{j,est}^{B}]_{\times} \cdot \boldsymbol{b}_{i_0} \tag{3.63}$$

There is no phase measurement sensitivity to the angular rate or gyro bias. The sensitivities for the GPS error states were given in Chapter 2 and will not be repeated here.

3.4.2 Gyro Measurement Prediction and Sensitivities

The following section describes how the low cost gyro measurements are treated, and the prediction and sensitivities are derived.

Prediction and Sensitivities

The gyro measurement residual is simply the actual measurement minus the predicted measurement, or:

$$\tilde{z}_g = \underline{\omega}_M - \hat{\underline{\omega}}_M \tag{3.64}$$

where

$$\underline{\omega}_M = \underline{\omega}_{BI}^{B} + \boldsymbol{b}_g + \upsilon_g \tag{3.65}$$

$$\hat{\underline{\omega}}_M = \hat{\underline{\omega}}_{BI}^B + \hat{\boldsymbol{b}}_g \tag{3.66}$$

so by applying relation 3.42:

$$\tilde{z}_g = (\underline{\omega}_{BN}^B - \hat{\underline{\omega}}_{BN}^B) + (\underline{\omega}_{NI}^B - \hat{\underline{\omega}}_{NI}^B) + \tilde{\boldsymbol{b}}_g + \upsilon_g \tag{3.67}$$

The inertial to nav predicted rate, $\hat{\underline{\omega}}_{NI}^B$, can be found by realizing that

$$\hat{\underline{\omega}}_{NI}^B = \hat{C}_{BN}(\underline{\omega}_{NI}^N) = [\mathbf{1} + [\delta\underline{\Theta}]_X](\underline{\omega}_{NI}^N) \tag{3.68}$$

Application of the above relations along with equation 3.32, yields:

$$\tilde{z}_g = \delta\underline{\omega}_{BN}^B + [2\delta\boldsymbol{q}_{BN}^B]_X \cdot (\underline{\omega}_{NI}^B) + \tilde{\boldsymbol{b}}_g + \upsilon_g \tag{3.69}$$

This can be differentiated to find the measurement sensitivities:

$$\frac{\partial\tilde{z}_g}{\partial\delta\mathbf{q}_{BN}^B} = -2[\underline{\omega}_{NI}^B]_X \tag{3.70}$$

$$\frac{\partial\tilde{z}_g}{\partial\delta\underline{\omega}_{BN}^B} = (\mathbf{1})_{3\times3} \tag{3.71}$$

$$\frac{\partial\tilde{z}_g}{\partial\tilde{\boldsymbol{b}}_g} = (\mathbf{1})_{3\times3} \tag{3.72}$$

3.5 Filter Algorithms

The Extended Kalman filter described in the previous sections is used in two scenarios. The first, the roof-top filter, will test the integration issues on a static mount on the roof of Draper Laboratory. The second scenario will study how these issues are affected by the high dynamic environment of a LEO by integrating the filter with a space simulation. The integration issues, such as power consumption and real MM Gyro data integration, are the focus of this study and will be tested on the two types of filters. The basic filter algorithm is presented in the following figure.

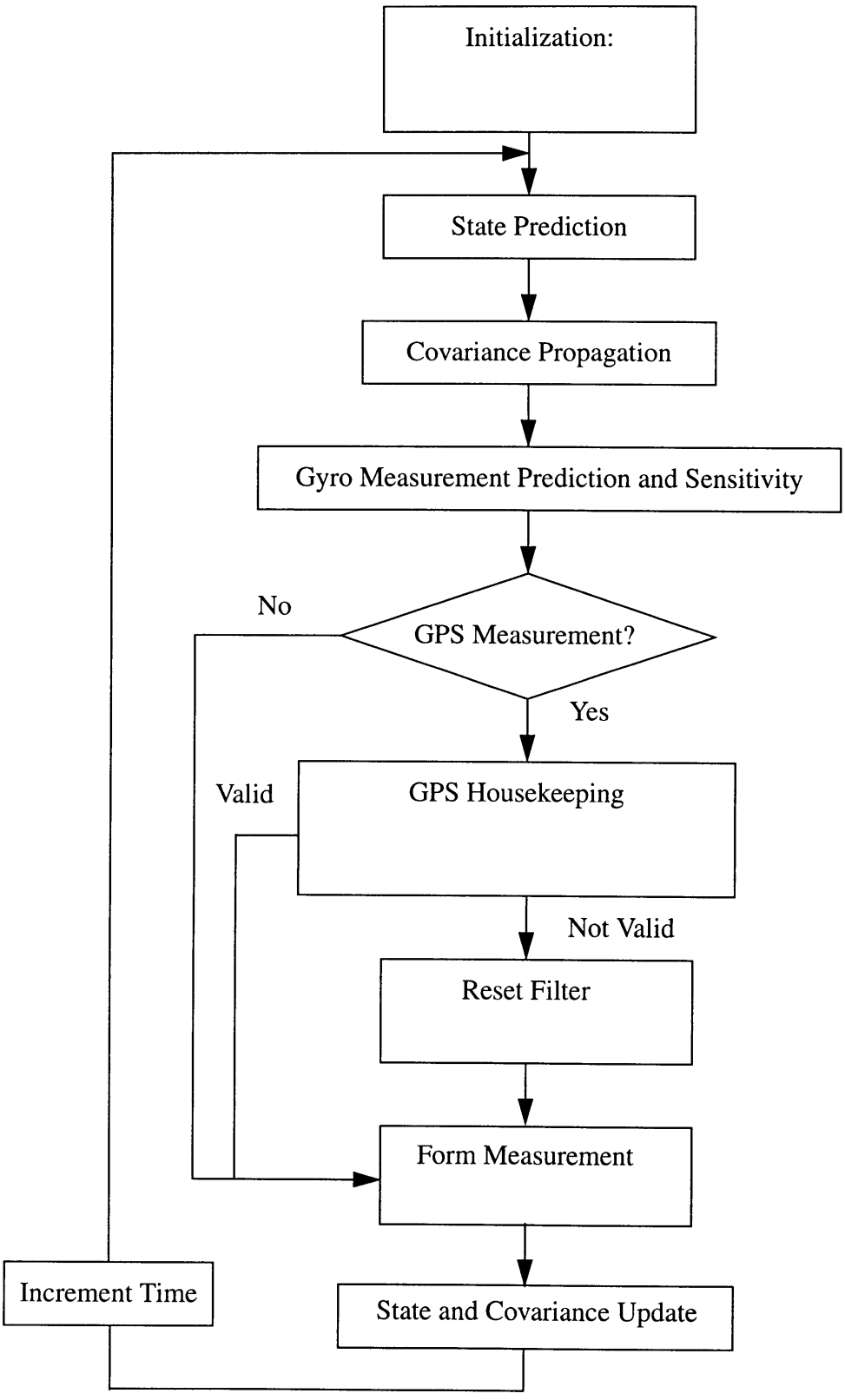

Figure 3.2: Basic Filter Algorithm

3.5.1 Roof-top Filter

The roof-top filter is used to post-process GPS data taken from the Trimble TANS Vector receiver on the roof of Draper Laboratory. Post-processing is required for a number of reasons. First, the MM Gyros are still not ready for real-time integration with other instruments and the equipment required to run the gyros could not be taken up to the roof. Also, the temperature fluctuations on the roof would add an additional degree of uncertainty in the gyro measurements that would preclude any useful analysis. Post-processing is also a necessity because of the receiver used. The Trimble is designed to calculate a point solution from each differential phase measurement. This means that it has its own algorithms that have nothing to do with the Kalman filter described above. Fortunately, it does output the raw differential phase measurement which the IGPS/MM Gyro ADS uses as one of its two measurement sources. Since the receiver outputs these measurements at 1 Hz, post-processing is required to vary the frequency of GPS measurement use.

The roof-top filter lacks the baseline estimation state. Temperature fluctuations on the roof are small enough not to affect the size of the rigid aluminum array on which the antennas are mounted. Since there is more multipath on the roof (the shed, heat stacks, and sky light mentioned in Chapter 2), analysis of data takes from the roof have been done with and without an extra multipath state. This will be described later.

3.5.2 Space Simulation

In order to validate this system for use in space, Puri developed an orbital simulation that incorporates the filter in a LEO environment [20]. This same simulation (with minor changes) will be used to test the integration issues which are the focus of this study. Importantly, it will also verify the ability of the IGPS/MM Gyro ADS to handle high frequency dynamics: something the roof-top version cannot do. For more information on the

details and mechanics of the orbital simulation, see reference [20]. A summary of the simulation is presented below for convenience.

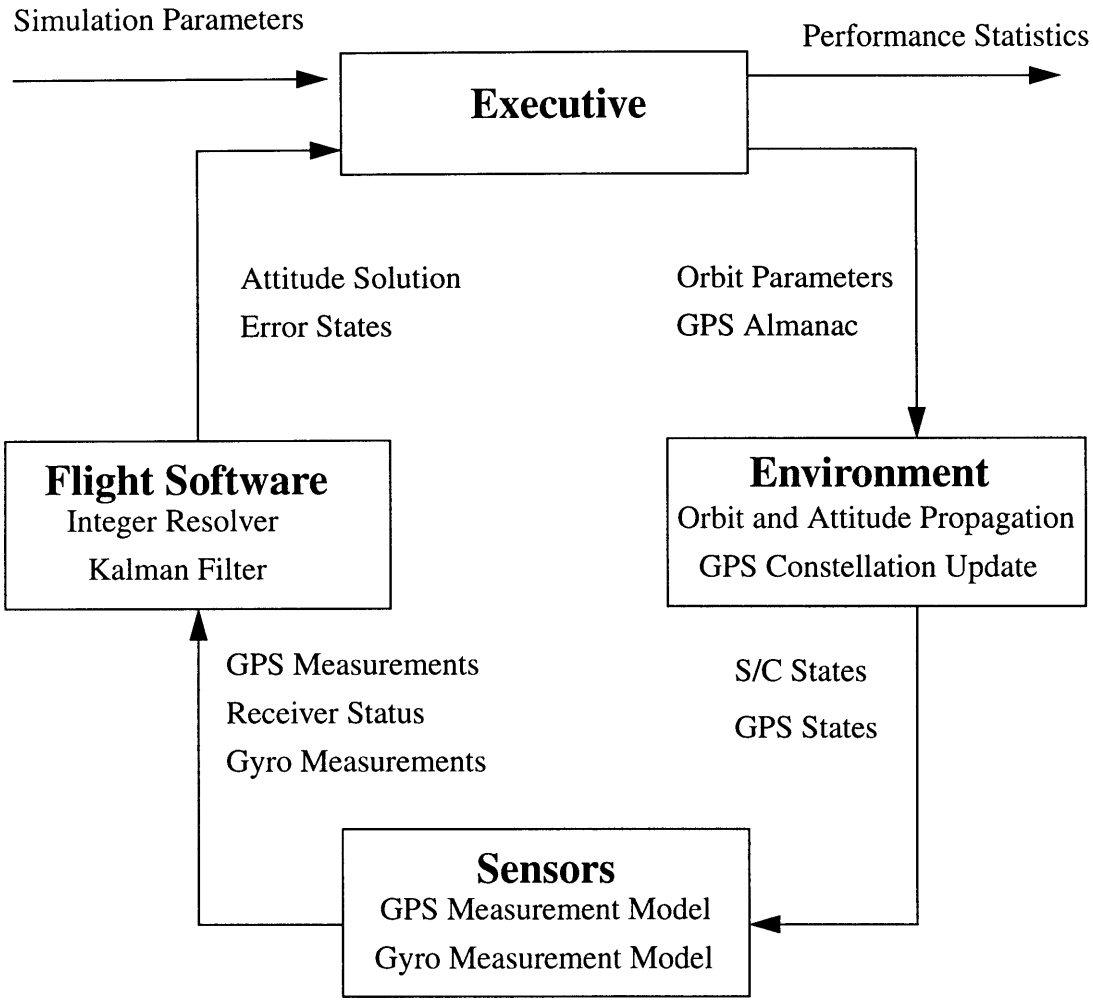

Figure 3.3: Summary of Orbital Simulation

GPS measurement errors for the simulation are generated using the dynamic error models developed in Chapter 2. The orbit used in this study will be a typical LEO used by small communications satellites. The orbit is assumed to be circular with variable inclination, semi-major axis, and longitude of ascending node. No orbit pertubations are modeled. For the space simulations the inclination chosen is 89 degrees, and the altitude is 421 nm, which corresponds to the orbit of the Iridium satellite constellation. The GPS constellation

is propagated using the ICD-GPS-200 almanac equations [20].

Chapter 4

Covariance Analysis

4.1 Overview

This chapter presents a covariance analysis of the Kalman filter to analyze different integration schemes for the ADS. One area of concern is the effect of using varying GPS measurement update rates. Because the goal of this application is to provide an ADS of reasonable quality and low power, the trade-offs between performance and power usage must be analyzed. Power consumption will be addressed Chapter 7, but a baseline assumption of the covariance analysis is that most of the power used by the IGPS/MM Gyro ADS is consumed by the interferometric GPS receiver. This assumption seems valid knowing that the TANS Vector receiver itself uses four Watts at its 12-18 Volt operating range, while the gyro system will use well under one Watt of power. Covariance analysis will be done on the roof-top filter as well as on the space filter. This analysis will begin by looking at the covariance matrix of the EKF when run with real measurements; however, a linearized covariance analysis will be conducted for most of the study. The linearized analysis is performed because of the great computational burden required for Monte Carlo runs with the EKF.

4.2 Methodology

The following sub-sections describe the manner in which the covariance analysis in this study was conducted.

4.2.1 Equations

The Kalman filter can be used not only as an estimator, but also as a means to conduct system error analyses to compare different plausible designs. The advantage of a Kalman filter covariance analysis is that the estimate, $\hat{x}$, does not have to be propagated along with the covariance matrix, **P**. To obtain the steady state value of the covariance we simply apply the recursive equations of the previous chapter [1]. The following figure demonstrates the recursive loop for propagating the error covariance matrix. Note that steady state analysis techniques, such as solving the closed loop Lyapunov equation, will not work in this case. This recursive loop must be used due to the different frequencies at which the two discrete measurements are input to the filter.

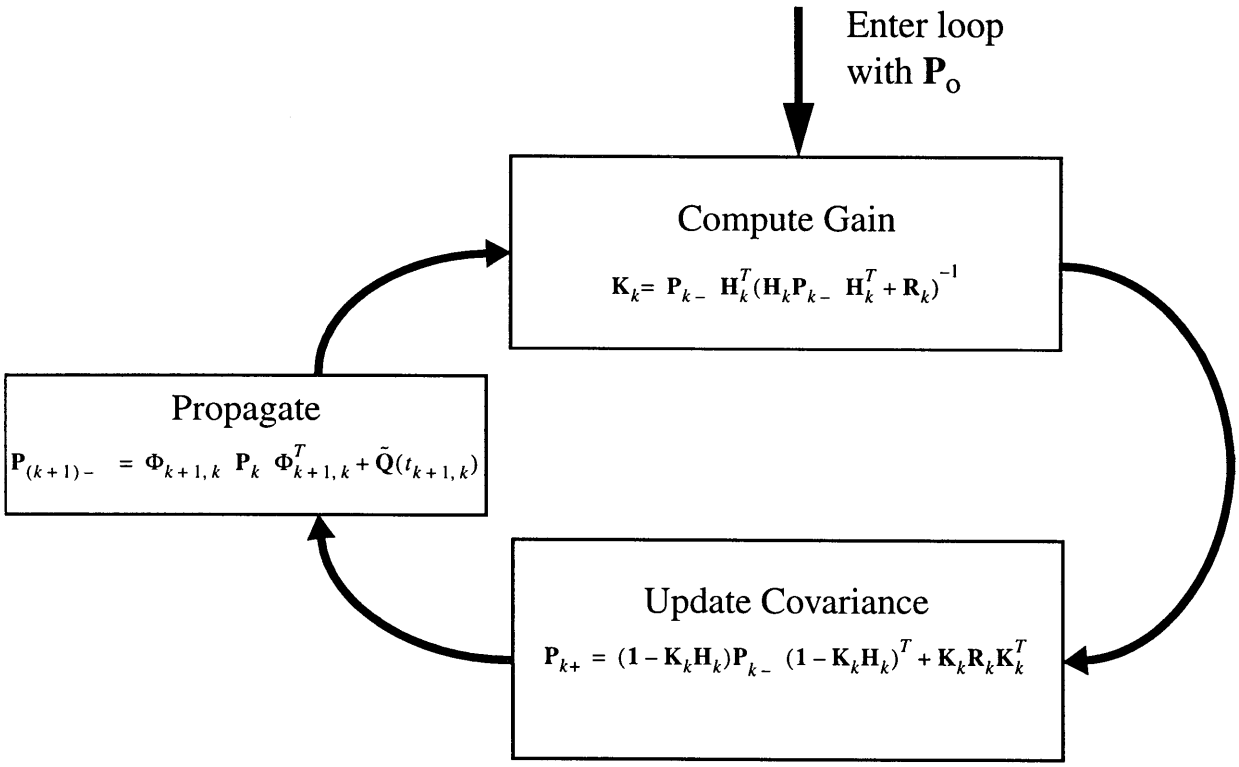

Figure 4.1: Recursive Covariance Propagation

4.2.2 Linearization

In the EKF the non-linear system is linearized about a trajectory that is continuously updated with each state estimate obtained from the measurements. In the above algorithm, however, the state estimate is not propagated and there are no measurements. To linearize the system, a nominal point in the trajectory is chosen that is representative of what the filter would experience if it was running in real-time using real measurements. Since the non-linearity of the system is caused by the GPS SV's motion through the visible sky, a *frozen* nominal geometry is chosen. It consists of six SV's with an Attitude Dilution of Precision (ADOP) of about .053 (see Appendix C). A factor of safety is included by invalidating the lowest satellite in elevation. This nominal geometry is shown in the sky plot below:

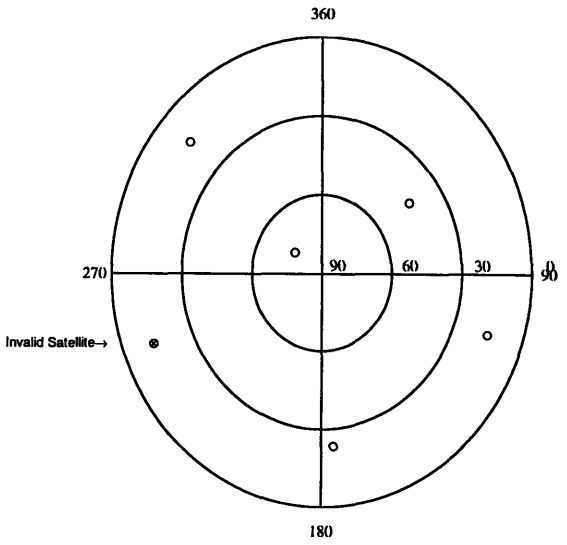

Figure 4.2: Nominal Geometry Used in Linearization

The sky plot is a representation of GPS SV's as *seen* by the receiver. Elevation is measured from 0^o to 90^o where 0^o is the horizon. Azimuth is measured in standard north, south, east and west where 360^o is north. All the measurement sensitivities for the linearized covari-

ance analysis will be derived from this geometry.

Verifying the Linearization

To ensure that the above linearization technique will yield accurate variances, it must be compared to actual EKF variances. The following plot shows the results of the roof-top filter for a standard run. The differential phase data was recorded on the Draper Lab roof on January 14, 1998, at a rate of 1 Hz from the Tans Vector. The IGPS antenna array was the 0.6 meter square mentioned in the first chapter. Simulated gyro measurements were integrated every 2 Hz. The gyro measurements were produced according to the gyro measurement model presented in Chapter 2. Unless otherwise stated, the following tests are done assuming a MM Gyro bias of 5^{o}/hr and an ARW of $.25^{o}/hr^{1/2}$. The EKF 1σ standard deviation lines are overlaid about the mean of the solution. The mean had to be used due to the uncertainty of the actual truth orientation of the array, and it is computed by taking the average value of the solution over the entire interval. The run comprises approximately three and a half hours of data. The satellite geometries, measurement validities and ADOPs for this run are given in Appendix B.

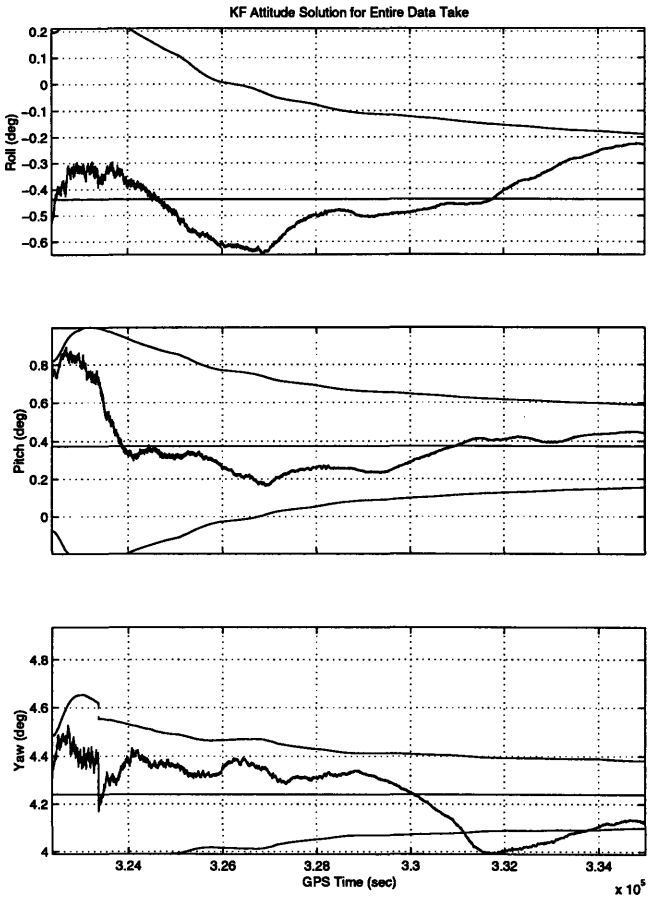

Figure 4.3: EKF Results for 01/14/98 GPS Data

In order to see the effect of reducing the GPS measurement update frequency on the variance of the solution, various runs on the same data were performed with the only difference being the frequency of GPS measurement use. In other words, instead of using all the differential phase data recorded, only an amount commensurate with the GPS measurement update frequency was used. This was possible since the differential phase data is time-tagged by the receiver. The next figure summarizes the effect this had on the EKF attitude error. The steady state value was obtained by averaging the value of the attitude variance during the last few seconds of the run.

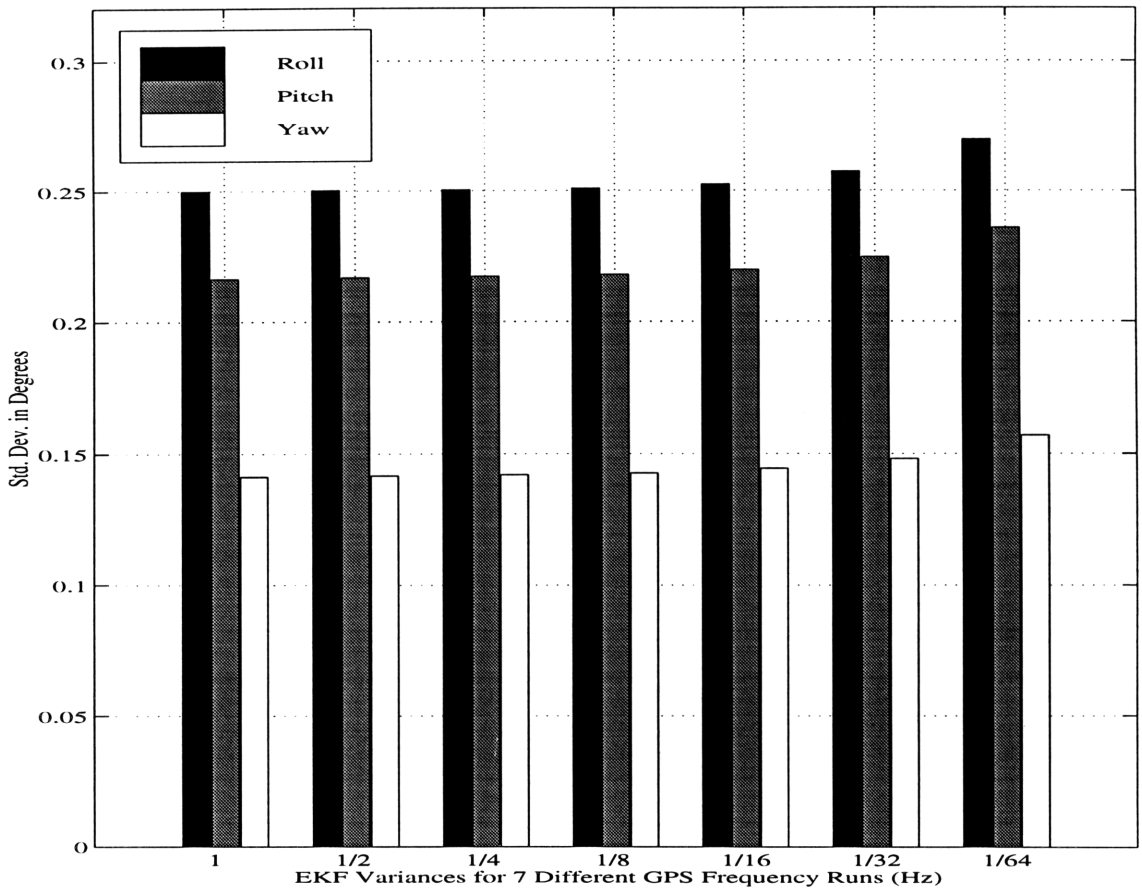

Figure 4.4: EKF Steady State Standard Deviations for Varying GPS Use

We see that attitude errors did not increase much from using GPS measurements once every second to once every minute. Using even less GPS updates than the 1/64 Hz rate, however, does cause a filter reset (see Figure 3.2). We would expect the linearized covariance analysis to show similar results. The following figure displays the steady state results of the linearized recursive covariance analysis:

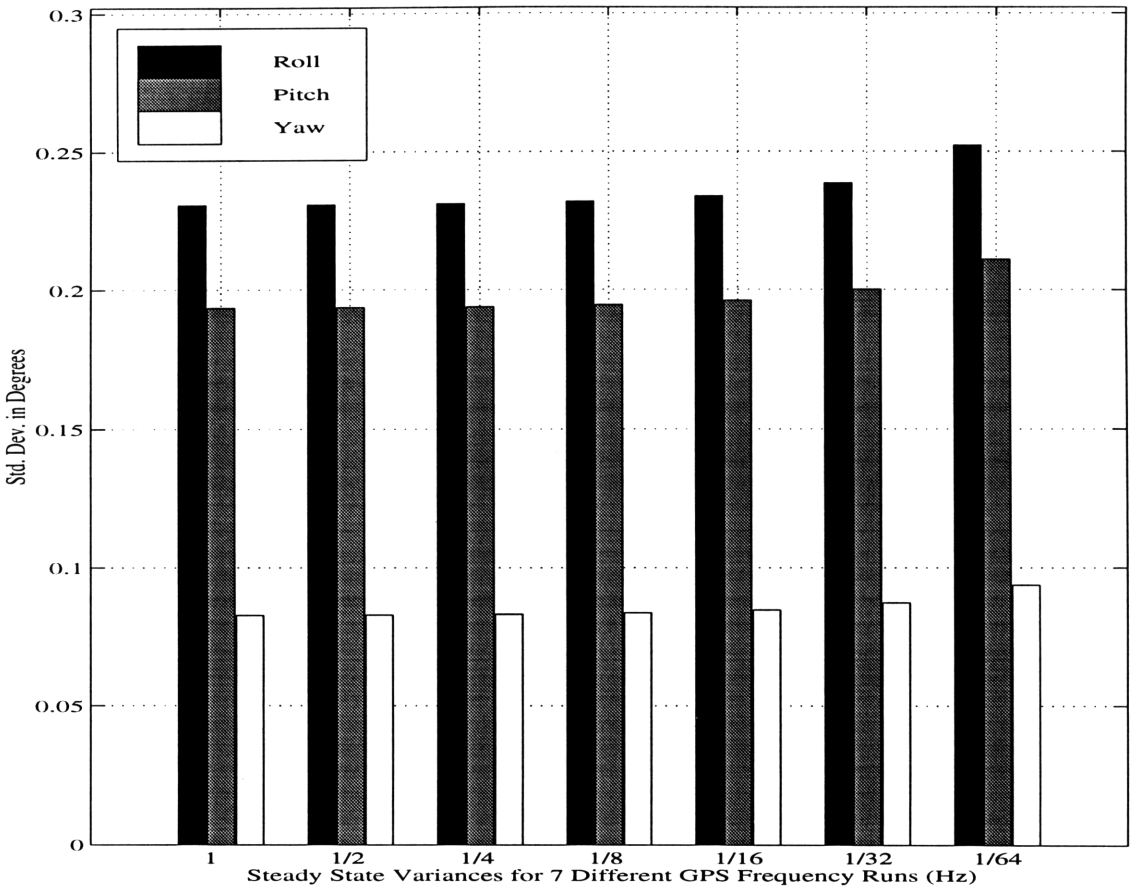

Figure 4.5: Steady State Error of Linear Analysis

From this figure we conclude that the linearized covariance results are indeed credible since the general trend and magnitude of the standard deviations are similar. Modest discrepancies, as those seen in the yaw values, are the result of using the same geometry versus a changing environment. The yaw performance is always better than roll or pitch since the IGPS array is orthogonal to the yaw axis.

We would expect that continually reducing the frequency of GPS measurements would indeed degrade the accuracy of the attitude solution. This is confirmed by the following plot which carries the trend of reducing GPS use still further:

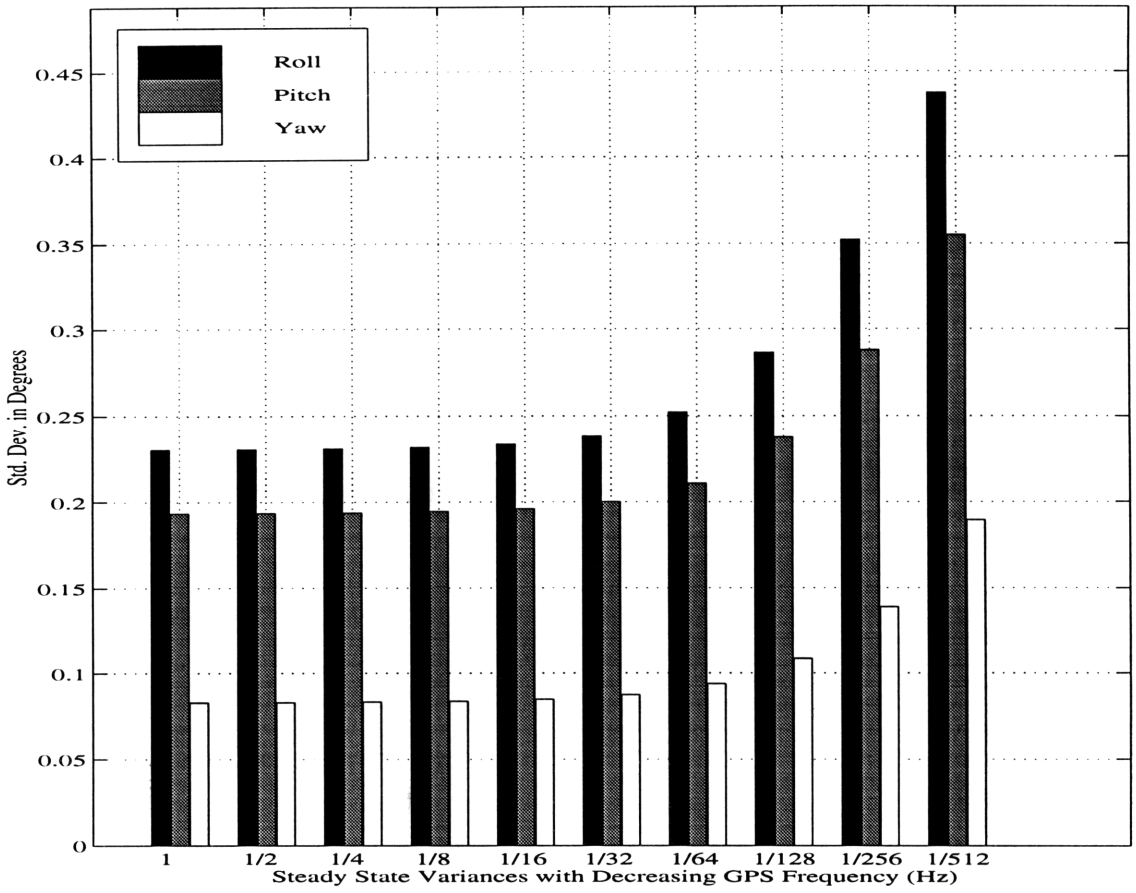

Figure 4.6: Linear Analysis for Continually Less GPS

The results of this graph serve to show that for the region in which the EKF will not reset (any GPS frequency use below 1/64 Hz), the GPS update frequency has negligible effect on the error bounds. A filter reset is not necessarily a bad thing, but it does prohibit steady state variance analysis since the covariance matrix is re-initialized. Also, the aim of this analysis is to evaluate the impact of mitigating the use of the "power hungry" GPS interferometer on performance. Resetting the filter calls the integer ambiguity resolver which requires an additional, although slight, computational burden.

The above results were for the static 0.6 meter per side square platform. Similar analysis

can be done with the space filter in order to determine the effects of dynamics on the error. For this analysis, the space filter will be placed in the LEO orbit described in Chapter 3. The results of one run of 7000 seconds are shown. This particular simulation run used the 0.6 meter IGPS array.

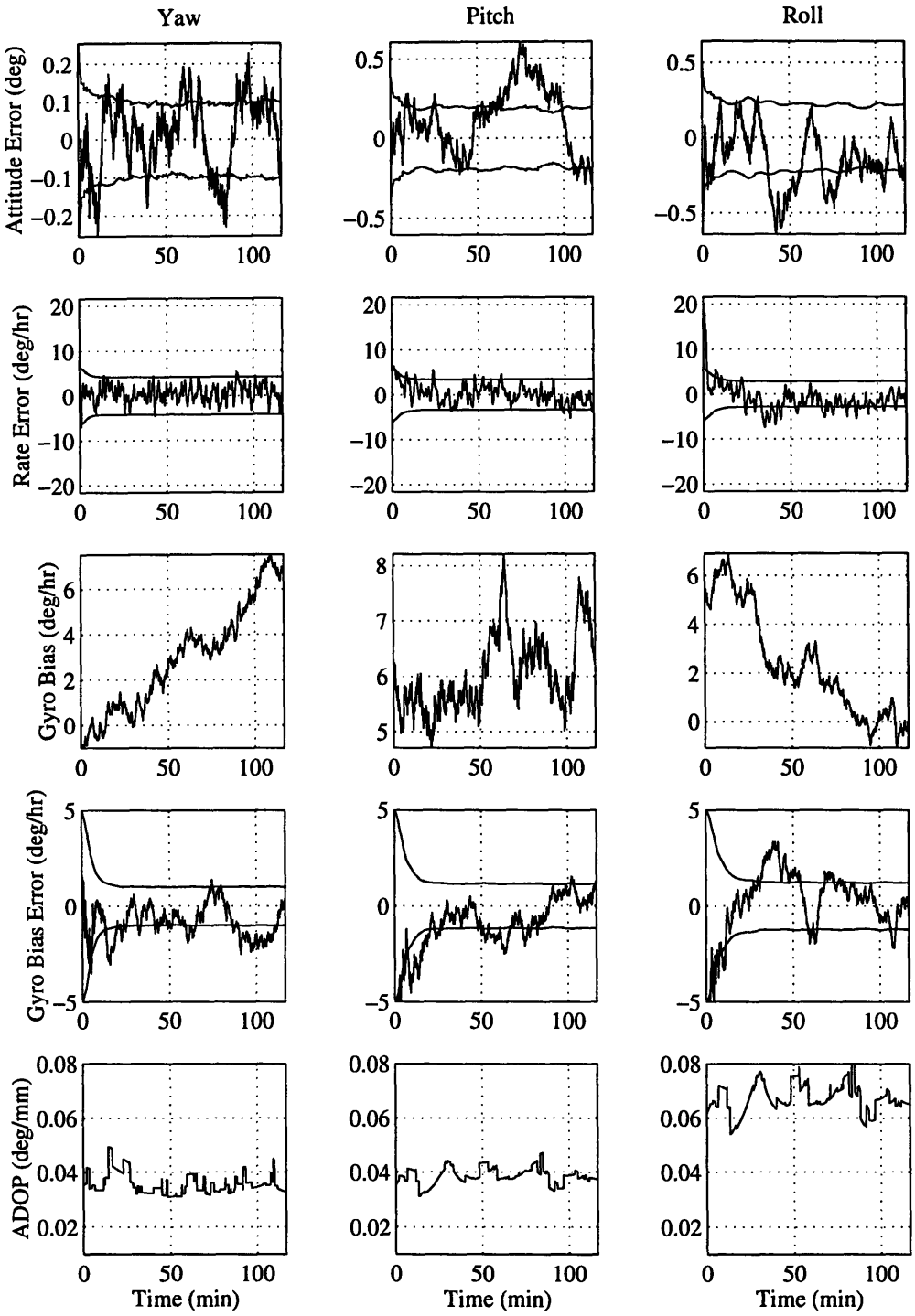

Figure 4.7: EKF Orbital Simulation Results

For the above run the GPS update frequency was 1Hz. The 1 σ standard deviations overlays are included along with the errors. The errors are derived by subtracting the estimate

from the truth. The process noise intensity used on the attitude rate was 1.2 X 10^{-5} N-m. When GPS measurements are varied from 1Hz to 1/80Hz, the errors are bounded in a similar fashion as in the static roof-top case:

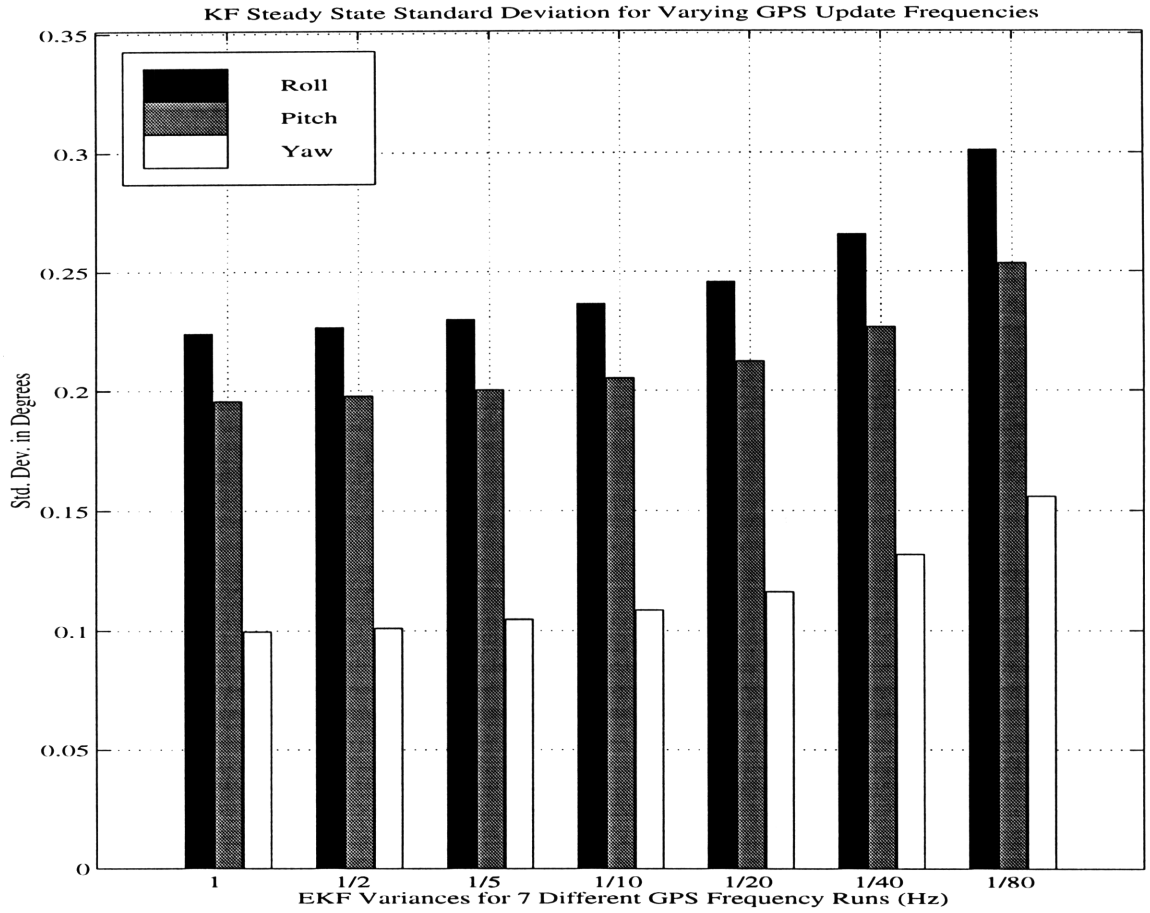

Figure 4.8: EKF Standard Deviations for Varying GPS Use Sim Runs

The linearized version of the above analysis conforms to the expected trends as shown in the following plot:

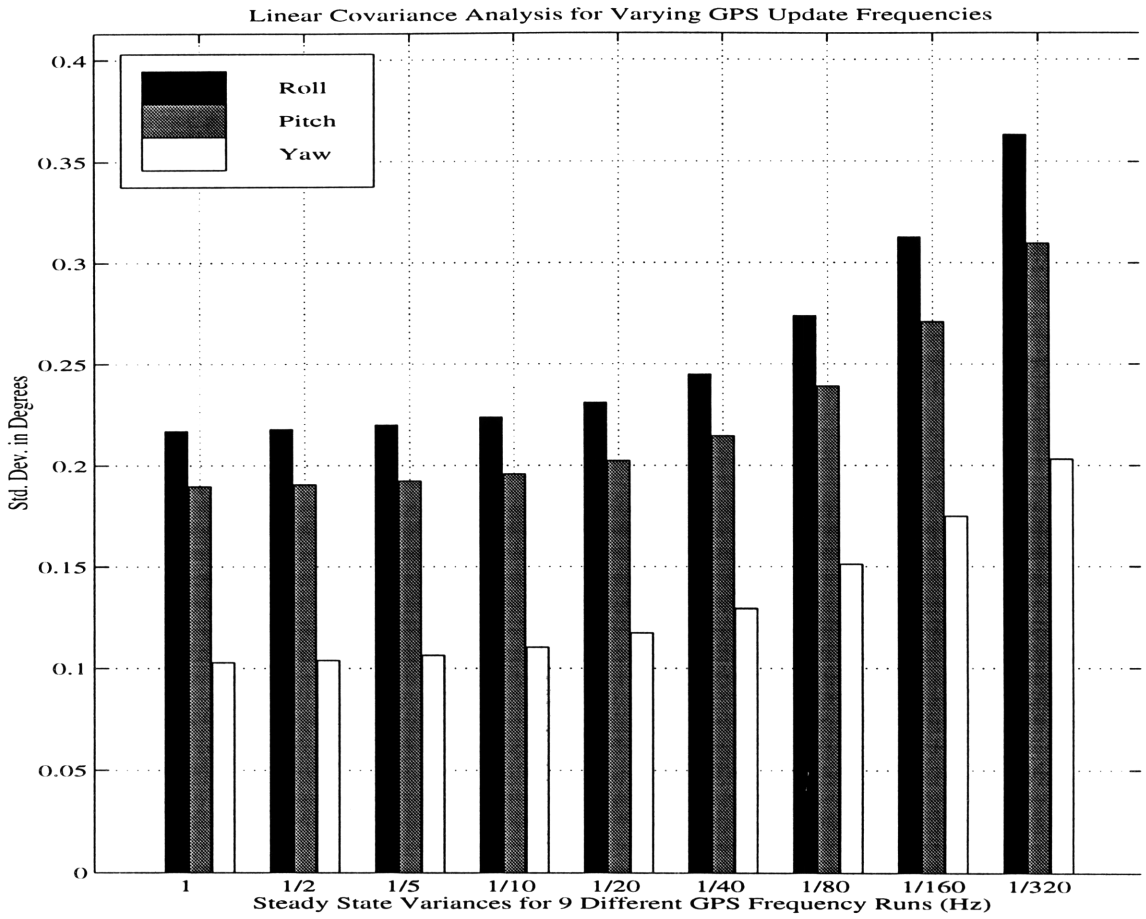

Figure 4.9: Linearized Analysis for Space Sim

The previous plots support the accuracy of the linearized covariance analysis method. This linear analysis is the basis for the rest of the covariance analysis which follows.

4.3 Analysis

The conclusion that can be drawn from the space simulation results is important in understanding the performance limits of the system. As compared to the roof tests, we would expect the errors of the high dynamic space simulation environment to increase due to the higher uncertainty of orbital dynamics represented by the added process noise. The orbital errors were actually a bit smaller since the error bounds had to be increased on the roof filter to make up for multipath effects on the roof. What is important to note, however, is that

the space filter's errors were very comparable to the roof filter's errors.

4.3.1 Unmodeled Dynamics

There are two reasons why the space filter errors do not differ greatly from the roof-top filter errors. The body-frame *motion* experienced by the static roof-top filter due to the moving satellite geometries is comparable to the slow body-frame dynamics of a spacecraft. As long as LOS vectors are updated quickly enough in the space simulation, the effects of the gravity gradient torque are not that large. Another possible explanation is that the EKF in the space simulation is based on a model of the dynamics that is rather simple. If the EKF is depending on the model too much to propagate the state, in other words the process noise on angular rate error is low, it is difficult to see just how much of an impact varying GPS measurement frequency or gyro quality has on the performance of the ADS. The nominal design process noise on the angular rate error, $\sigma_{\delta\omega}$, of 1.2 X 10^{-5} N-m intensity is an optimistic estimate of likely orbital conditions. If typical sources of unmodeled torques are summed, such as aerodynamic drag, solar radiation pressure, magnetic field torque, and internal spacecraft dynamics, the intensity of the unmodeled disturbance torques might reach as high as 10^{-3} N-m [26]. This value does not include any perturbations of the "known" spacecraft attitude control system torques. In order to observe the effects of varying the design process noise, analysis is done on a 0.6 meter and 1 m IGPS array by using a suite of lower quality gyros ($\boldsymbol{b}_g$ = 100°/hr, τ_g = 2 hrs and ARW = .75°/$\text{hr}^{1/2}$) and a 1 Hz GPS update frequency rate:

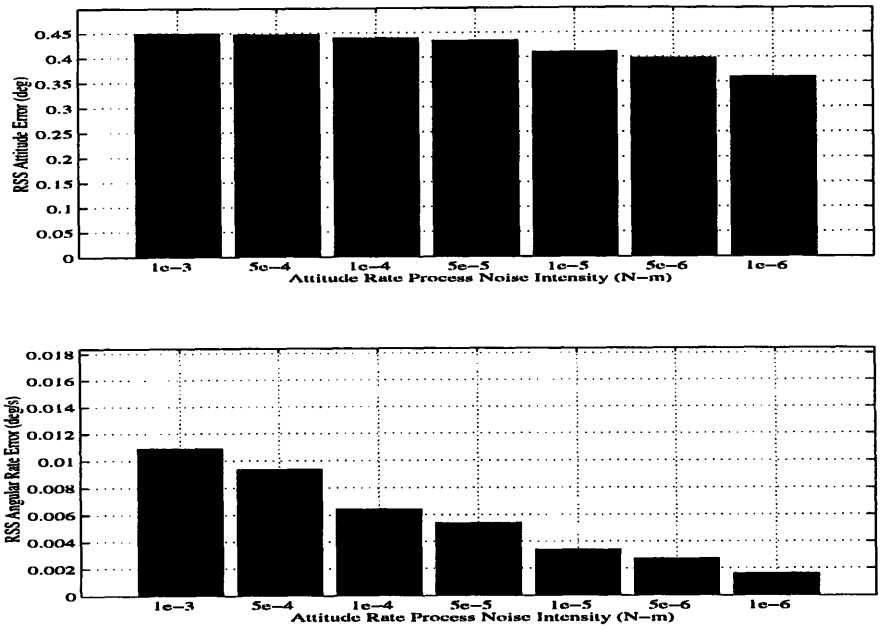

Figure 4.10: Attitude and Rate Error as a Function of Design Process Noise Intensity for 0.6 m Array

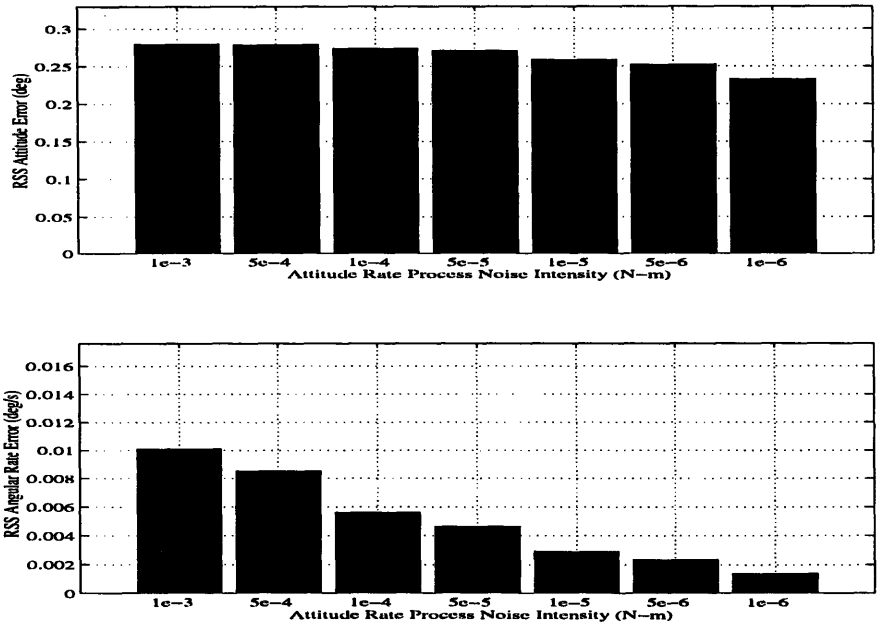

Figure 4.11: Attitude and Rate Error as a Function of Design Process Noise Intensity for 1 m Array

Attitude error drops as expected when the dynamic model is more precise. We see, how-

ever, that even though the angular rate error increases with increasing angular rate process noise, there is an upper bound on the RSS attitude error. This bound is provided by the GPS phase measurements. As will be shown in the next few pages, having a better gyro will help tighten these error bounds since the unknown disturbances will be better estimated.

The error, as a function of decreasing GPS updates and increasing design process noise, will now be examined. The following 3-D bar graph summarizes these effects for a 0.6 meter IGPS antenna array.

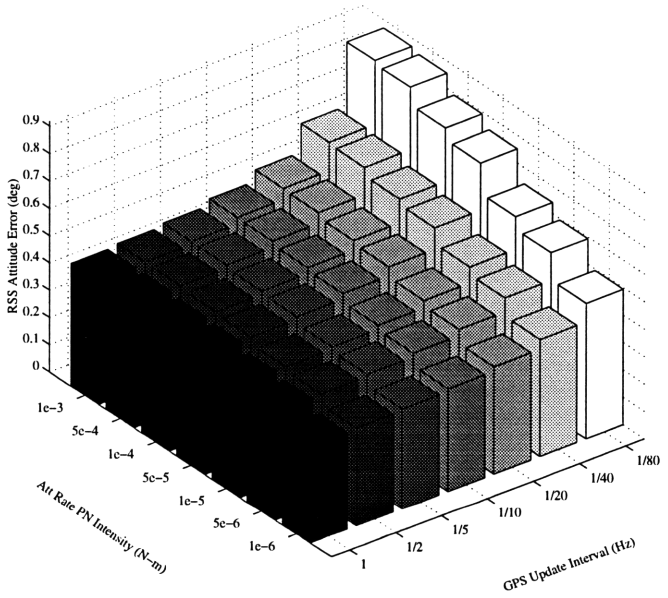

Figure 4.12: S/C Attitude Error as a Function of GPS Update Interval and Dynamic Model Quality/Design Process Noise for a 0.6 m IGPS Array

The bound that the GPS measurements had imposed in Figure 4.10 is now stretched with decreasing GPS updates. The unknown dynamics are allowed to propagate for a longer time, hence decreasing the performance of the estimator. This bound, however, can be reduced with a suite of better gyros. Figure 4.13 demonstrates the performance improve-

ments obtained when increasingly better gyros are applied. The different gyro suites tested are listed in the following table.

Name	Bias (deg/hr)	Time Constant (hr)	ARW $deg/hr^{1/2}$
Suite 1	1	8	.1
Suite 2	5	8	.25
Suite 3	10	8	.25
Suite 4	20	8	.5
Suite 5	40	6	.75
Suite 6	80	4	.75
Suite 7	100	2	1

Table 4.1: Description of Various Gyro Suites Analyzed

The attitude rate process noise was held at 1.5×10^{-4} N-m which seems to be a reasonable value that can be expected from external spacecraft torques (not to include ACS torques) [26] .

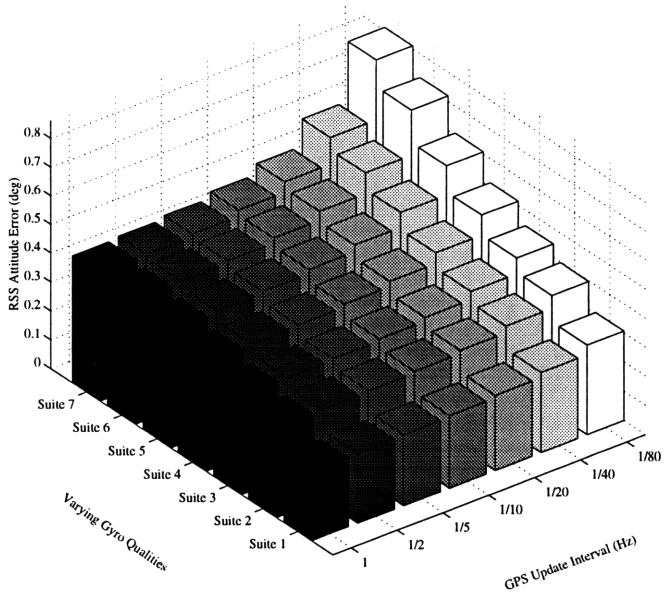

Figure 4.13: Attitude Error as a Function of GPS Update Interval and Gyro Quality for a 0.6 m IGPS Array

The higher the gyro quality, the better the ADS can track high frequency dynamics during GPS outages. Performance and cost are synonymous with trade-offs in engineering, and this system is no different. What remains to be analyzed is how much power the IGPS receiver requires and how compatible this cost is with available/obtainable gyro qualities. This will be discussed in Chapter 7.

A repeat of the analysis done in Figure 4.12 and 4.13 is now shown using a 1 meter IGPS antenna array. Increasing the size of the array is one method to improve this ADS's performance. This comes at the expense of larger size and a greater computational burden to resolve the integer ambiguities. This also will be discussed in Chapter 7.

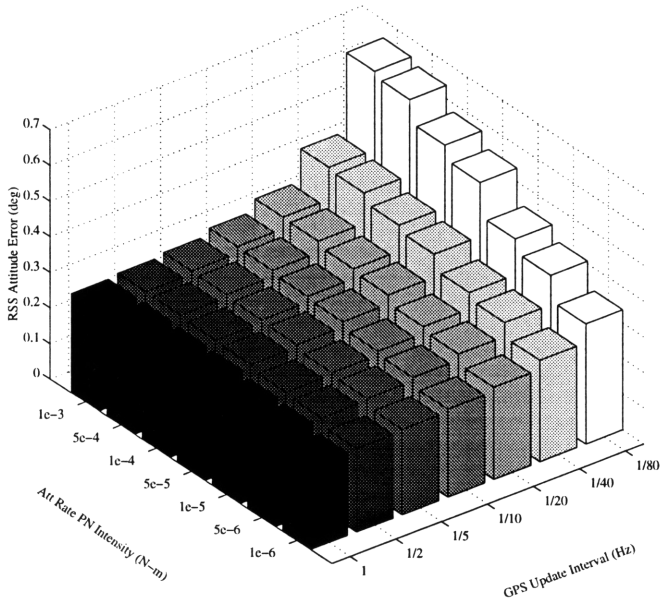

Figure 4.14: S/C Attitude Error as a Function of GPS Update Interval and Dynamic Model Quality/Design Process Noise for a 1 m IGPS Array

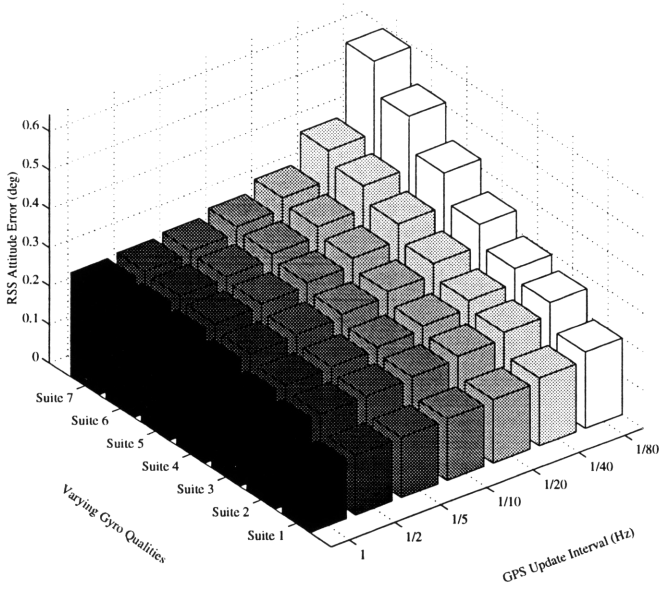

Figure 4.15: Attitude Error as a Function of GPS Update Interval and Gyro Quality for a 1 m IGPS Array

Chapter 5

Robustness to Failure

One important aspect of a system, especially when comparing it to other viable alternatives, is its robustness to failure. The performance of a system must be analyzed *vis-á-vis* the redundancy of the system. This chapter will look at some inherent redundancies in the IGPS/MM Gyro ADS which make it robust to failure.

5.1 Introduction

Most aerospace systems are designed with some type of robustness to failure. The failure of only one system, such as the ADS, could result in loss of mission capabilities. To provide robustness to failure most aerospace ADS's come with either a variety of instruments, such as a suite of sun/horizon sensors, gyros, magnetometers and star trackers; or a redundancy in the number of certain sensors, such as multiple gyros. If an orthogonal gyro triad is measuring rate about three axes, then a loss of one gyro would be a single point of failure. Solutions to this problem can either be to provide back-up gyros or to align five or six gyros in such a manner so as each senses components of rate from multiple axes. In either case, the cost of providing redundancy is higher than having a bare-bones system.

5.2 Advantages of the T-C Model Replacement Mode

The tightly-coupled model based Kalman filtering used for this application actually gives the ADS a certain degree of robustness to failure not inherent with traditional model replacement mode systems. The following figure is a visualization of the way measurements are treated in this application.

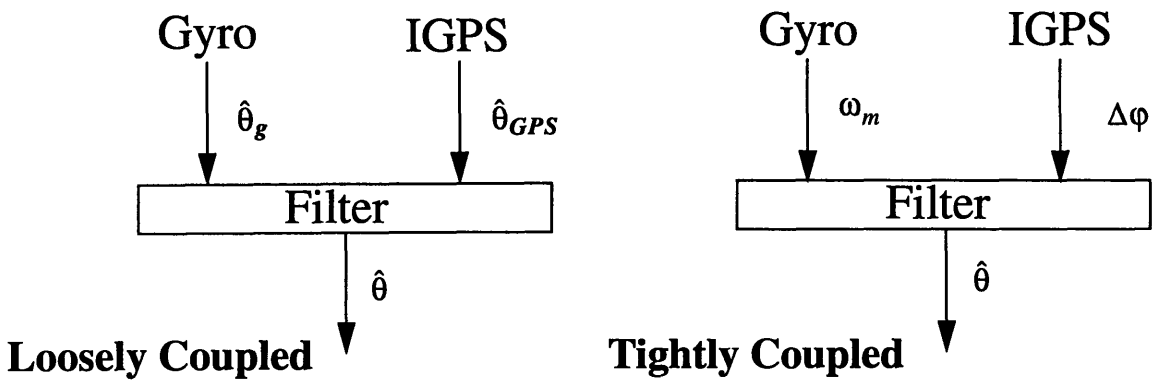

Figure 5.1: Tightly Coupled vs. Loosely Coupled ADS

In the loosely coupled system the filter is used to optimally blend two attitude estimates previously computed by the gyros and IGPS. The IGPS solution is then a least squares point solution. One disadvantage with this method, as well as with the traditional model replacement mode, is that each strapdown gyro is a single point of failure. If these systems are to be made robust, then redundant gyros have to be used resulting in an increase in cost of the entire ADS. The tightly coupled integration proposed for this application circumvents this disadvantage. Each strapdown gyro output is treated as basically one measurement out of the total number of measurements, which for this application would be one out of twenty-one measurements: three gyros and eighteen phase measurements (six channels times three baselines).

5.2.1 Robustness to Gyro Failure

Since there is a dynamic model to aid in state propagation, we would expect continued operation (albeit degraded) from this system in the event of a gyro malfunction. This would be impossible in a model replacement mode system that depended on the gyro triad output for state propagation. The amount of performance degradation in the event of a gyro malfunction is a function of the quality of the MM Gyros and the IGPS measurement

update interval. The gyro triad characterized by Suite 2 in Table 4.1 is a good approximation of the quality of MM Gyros that may be achieved in the near future. The following table describes the three operating states that will be examined using the Suite 2 triad.

Gyro State	Description
Normal	[1 1 1]
Pitch Out	[1 0 1]
Pitch & Yaw Out	[1 0 0]

Table 5.1: Descriptions of Operating States

The effect on performance of using these three different operating scenarios are listed in the following table as a function of IGPS update interval. The results are for a 0.6 m^2 IGPS array.

IGPS Update Freq	Normal State [1 1 1]			Pitch Out [1 0 1]			P & Y Out [1 0 0]		
	Roll	Pitch	Yaw	Roll	Pitch	Yaw	Roll	Pitch	Yaw
1 Hz	.2177	.1904	.1028	.2177	.2755	.1031	.2179	.2774	.1701
1/2 Hz	.2187	.1912	.1041	.2187	.2802	.1043	.2189	.2823	.1793
1/5 Hz	.2208	.1931	.1066	.2208	.2865	.1068	.2209	.2887	.1925
1/10 Hz	.2246	.1966	.1106	.2246	.3008	.1108	.2247	.3030	.2161
1/20 Hz	.2319	.2032	.1176	.2319	.3290	.1178	.2320	.3313	.2587
1/40 Hz	.2459	.2155	.1296	.2459	.3862	.1297	.2460	.3886	.3424
1/80 Hz	.2748	.2405	.1515	.2748	.5397	.1517	.2749	.5424	.5752

Table 5.2: Attitude Error in Deg. of Three Gyro Conditions as a Function of Varying IGPS Update Intervals

These statistics can be better visualized in the following figure.

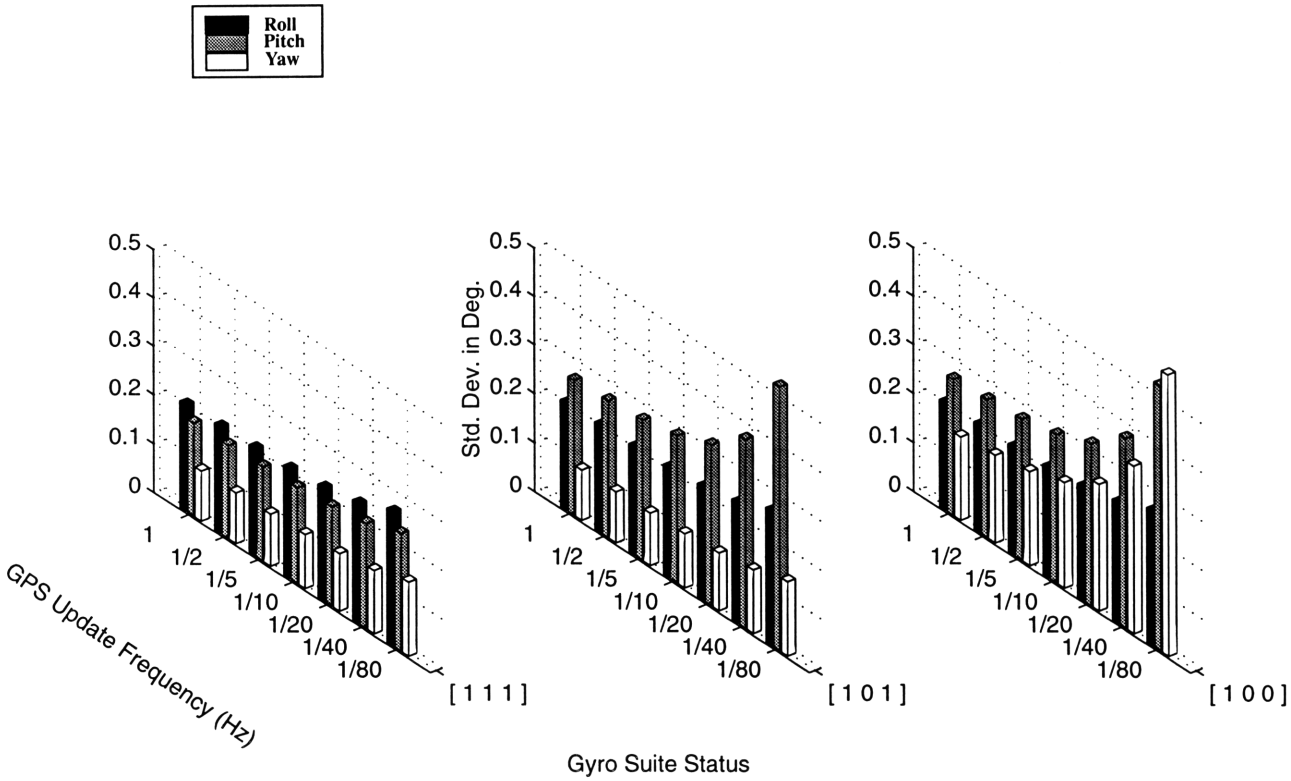

Figure 5.2: Attitude Error in Deg. of Three Gyro Conditions as a Function of Varying IGPS Update Intervals

The first bar chart in Figure 5.2 conforms with values in Figure 4.8. In the nominal configuration, the diagonal baseline of the IGPS array is aligned with the roll axis as demonstrated by the following figure.

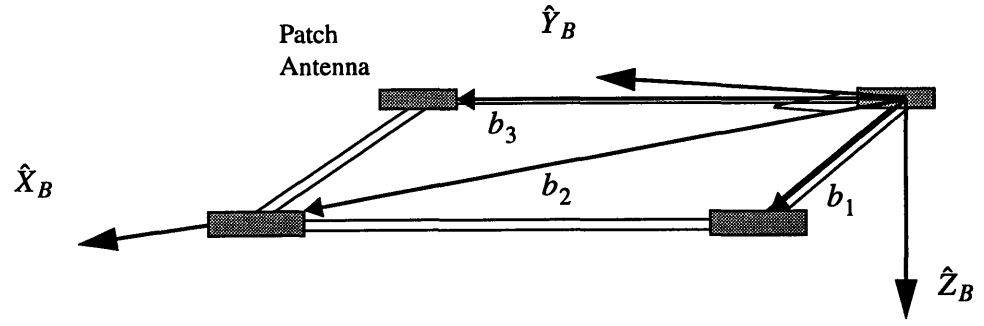

Figure 5.3: Nominal Configuration of IGPS Array

Notice that it is not possible to observe roll about a baseline using measurements solely from that baseline. Since the large diagonal baseline is used as the body frame roll axis, roll performance is worse than that of pitch and yaw. (If better roll performance is desired, rotation of the array to align the pitch axis with the long baseline is possible. Improved roll performance, however, would come at the expense of pitch performance.) Recall that yaw performance is better because the IGPS array is orthogonal to the yaw axis. In the second sub-plot of Figure 5.2, having the pitch gyro out significantly degrades pitch knowledge. With decreased IGPS updates, the pitch performance worsens faster than that of roll and yaw. The third plot in Figure 5.2 has the pitch and yaw gyros off-line. Although there is a noticeable degradation in both pitch and yaw performance, the orthogonality advantage mentioned above constrains the yaw errors at high IGPS updates. At lower IGPS updates, however, this advantage is clearly lost. Yaw knowledge degradation actually surpasses that of pitch in the lowest IGPS update frequency case. This is due to the coupling effect of the dynamics.

Although the loss of one or two gyros resulted in degraded performance, the ADS was still able to provide attitude information. To quantify the robustness to failure that this system provides, nine scenarios were created for this ADS each having a different operating sta-

tus. The nine cases are described in the table below. Suite 2 is the same gyro suite described in Table 4.1.

Case	Description of Sensor Status
Case 1	Normal Suite 2, IGPS Update of 1 Hz
Case 2	Normal Suite 2, IGPS Update of 1/10 Hz
Case 3	Suite 2 Pitch Out, IGPS Update of 1 Hz
Case 4	Suite 2 Pitch Out, IGPS Update of 1/10 Hz
Case 5	Suite 2 Pitch & Yaw Out, IGPS Update of 1 Hz
Case 6	Suite 2 Pitch & Yaw Out, IGPS Update of 1/10 Hz
Case 7	No Gyros, IGPS Update of 1 Hz
Case 8	No Gyros, IGPS Update of 1/10 Hz
Case 9	Suite 2, No IGPS

Table 5.3: Description of Operating Scenarios

The RSS steady state attitude errors associated with the above cases are shown below. All values assume an IGPS array of 1 m^2.

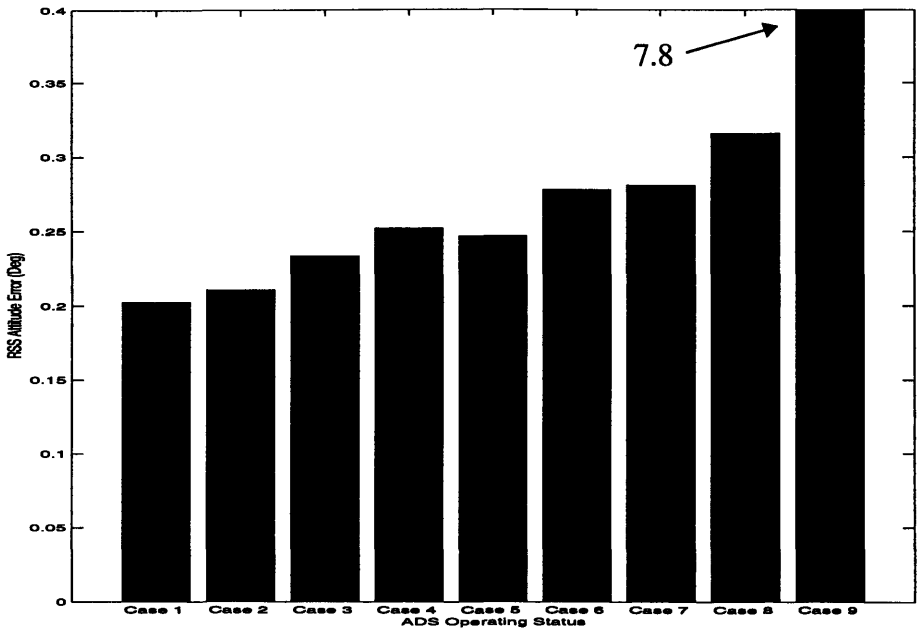

Figure 5.4: Performance Results of Various Operating Scenarios

Some interesting conclusions can be drawn from the above analysis. The IGPS bounds the errors of the ADS at 0.281 degrees at the 1 Hz GPS update frequency and at 0.316 degrees with a 1/10 Hz rate. Any amount of gyro information, whether from a full suite as in case 1 and 2 or just one roll sensor as in case 5 and 6, adds some benefit to the GPS only scenario. Another important point to note, however, is that the system is rendered useless if the interferometer malfunctions as shown in case 9. (Value shown for case 9 is after one hour. Error would be expected to increase monotonically with time.) GPS outage is a single point of failure, and the mean time until failure of the IGPS sensor will dictate the system's failure expectancy. However, even current off-the-shelf GPS systems have high failure tolerances.

5.2.2 Simulation Implementation for Gyro Loss

The space simulation is utilized in order to test the robustness claims made with the linear steady state covariance analysis. A 1/10 Hz GPS update run similar to that shown in Fig-

ure 4.7 is conducted, only that this time the pitch sensing gyro is rendered useless halfway into the orbital simulation. The gyro failure occurs at a time of about 58 minutes into the run. Simulation results are shown in Figure 5.5:

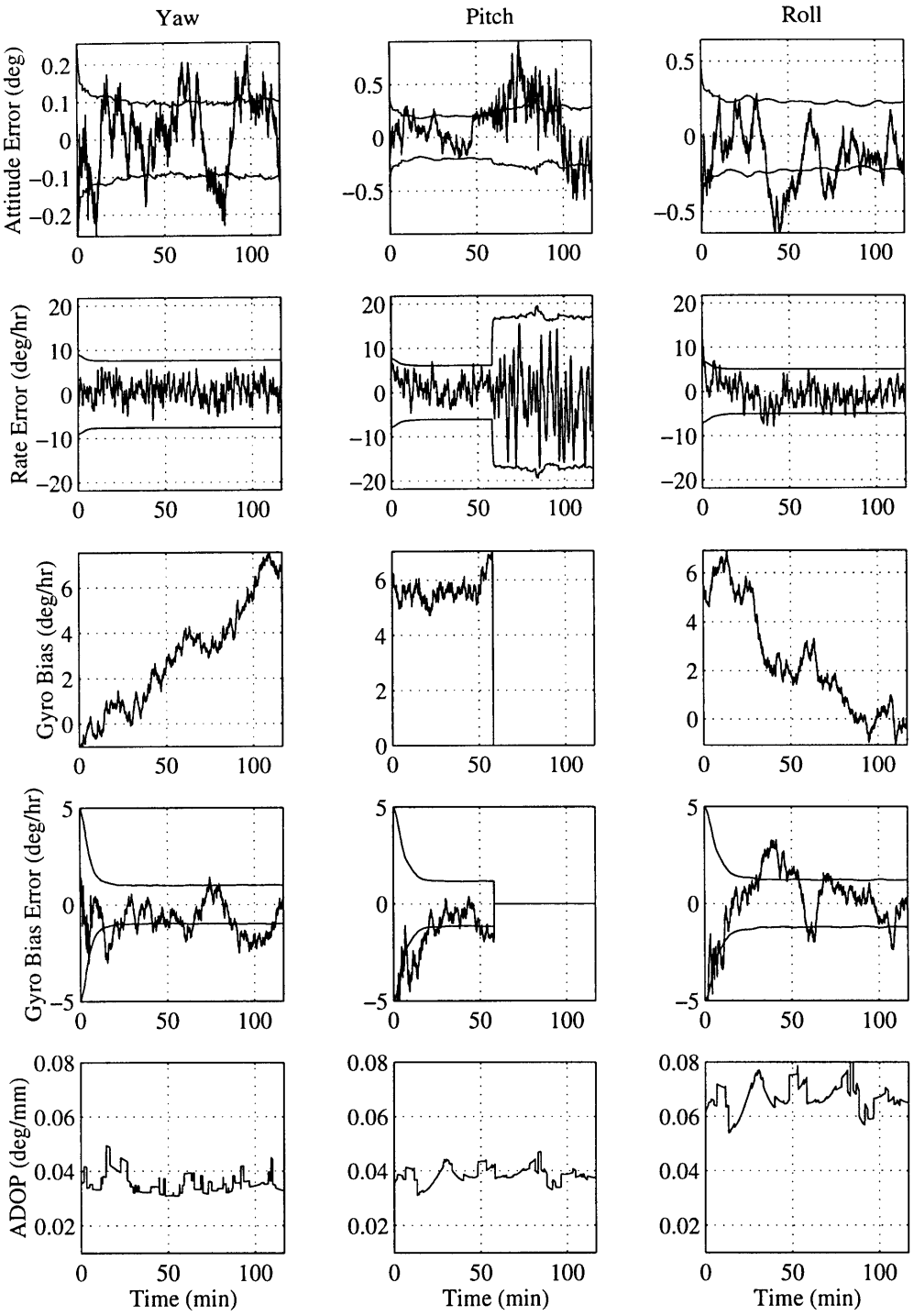

Figure 5.5: EKF Orbital Simulation with Pitch Gyro Failure at Midpoint (IGPS = 1/10 Hz)

We see that when the gyro fails, the error bounds on the rate immediately widen. The atti-

tude bounds follow suit, and although performance is degraded, complete system failure does not occur. In fact, integer ambiguity lock was still maintained in this scenario and no filter reset was required.

5.2.3 Robustness to Antenna Failure

It was mentioned above that an IGPS receiver outage was a single point of failure in this system, however, the interferometer will continue to provide useful information in the event of the loss of one baseline. Having four antennas with three baselines inherently provides robustness to an antenna failure, as the interferometer needs a minimum of three antennas and two baselines to operate. The following figure shows the loss in performance when no measurements are used from the diagonal baseline (illustrated in Figure 5.3) due to a failure in antenna number two. With the loss of one baseline and because of the disqualification of the invalid SV of Figure 4.2, a maximum of 10 GPS measurements (versus 18 possible) were used for this linear analysis.

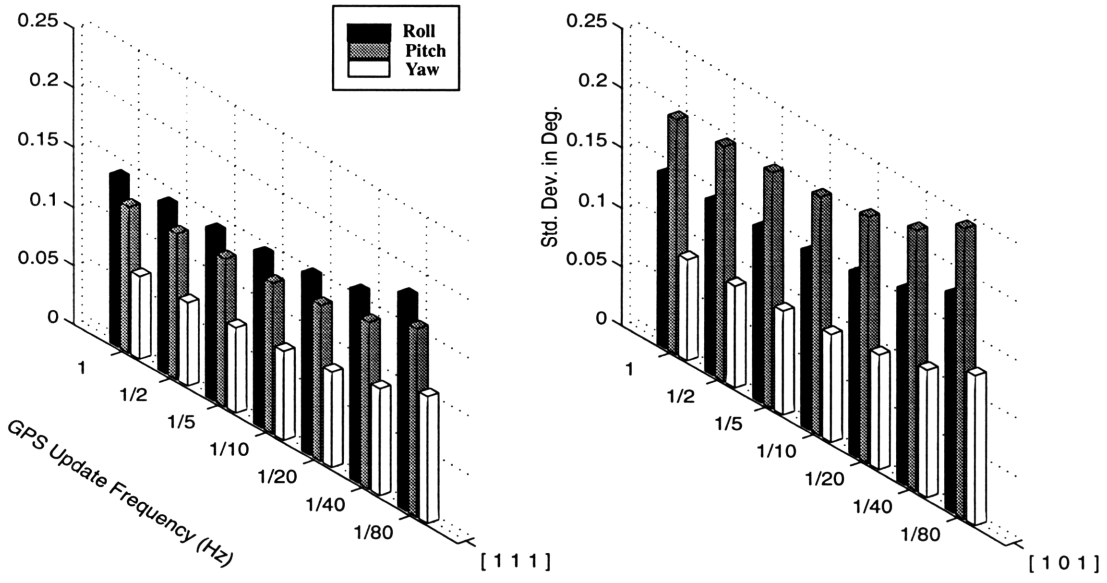

Figure 5.6: Performance Degradation with Loss of Baseline 2

Gyro Suite 2 was used in the above analysis. Notice the degradation of performance primarily in

the pitch axis. Yaw is also affected, but roll is not. As mentioned previously, roll about a baseline cannot be detected, and since the second baseline was aligned with the roll axis, no roll knowledge is lost.

5.2.4 Simulation Implementation for Baseline Loss

The following figure contains results for an orbital simulation in which the entire orbit was run with only baselines one and three operating. The GPS update interval was 1/10 Hz.

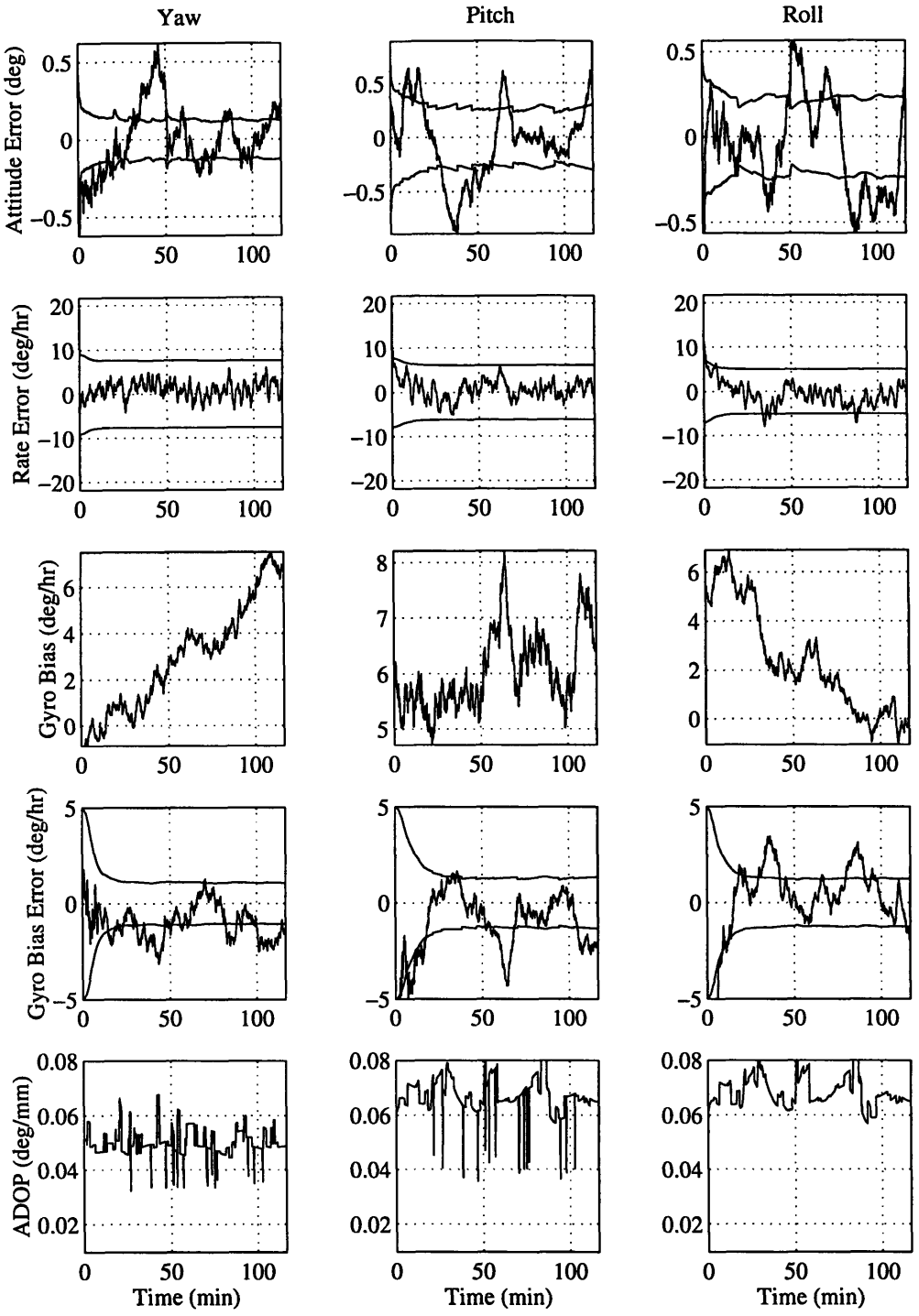

Figure 5.7: Simulation Results with loss of Baseline/Antenna 2

The results show that errors, although slightly degraded from the nominal array configuration shown in Figure 4.7, are still bound and that no filter reset was needed.

Chapter 6

Real Gyro Data Integration

All analysis so far has been done either with simulated gyro measurements (from the models of Chapter 2), as in the case of the EKF runs with GPS measurements; or with gyro error parameters, as in the case of the linear covariance analysis. This chapter presents results for the integration of real MM Gyro data on the static roof-top receiver.

6.1 Post Processing

Since the Draper Lab MM Gyros are still in development, GPS data and gyro data were taken on separate days and in separate environments. This is not a problem since the gyro data is obtained from a drift run, and the GPS array is static on the roof. Dynamic tests can also be done by integrating gyro data obtained from a turntable with the space simulation. Pre-determined rate trajectories can be fed into a programmable turntable and the recorded gyro outputs can then be used as the gyro measurements in the space simulation. Only a one-axis turntable is needed since the yaw, pitch and roll axes can be done separately and with the same test instrument. Dynamic testing with real gyro data, however, could not be completed in time for the publication of this work. Only the static results with the roof-top filter are presented in this chapter.

A static fifteen hour gyro drift test was temperature compensated and divided into three five hour blocks to form measurements for a three axis gyro suite. The gyro output was collected at every second and since the filter is set up to take gyro measurements at the 2 Hz rate, an interpolation scheme was formed to fill in the gaps. This scheme consisted of passing the gyro data through a lowpass Butterworth filter to separate the correlated bias

from the noise. The interpolation was done on the lowpass output and then corresponding random noise was added to yield gyro data every half second. The figure below shows the temperature compensated drift data collected from a prototype gyro and its corresponding correlated and white noise components.

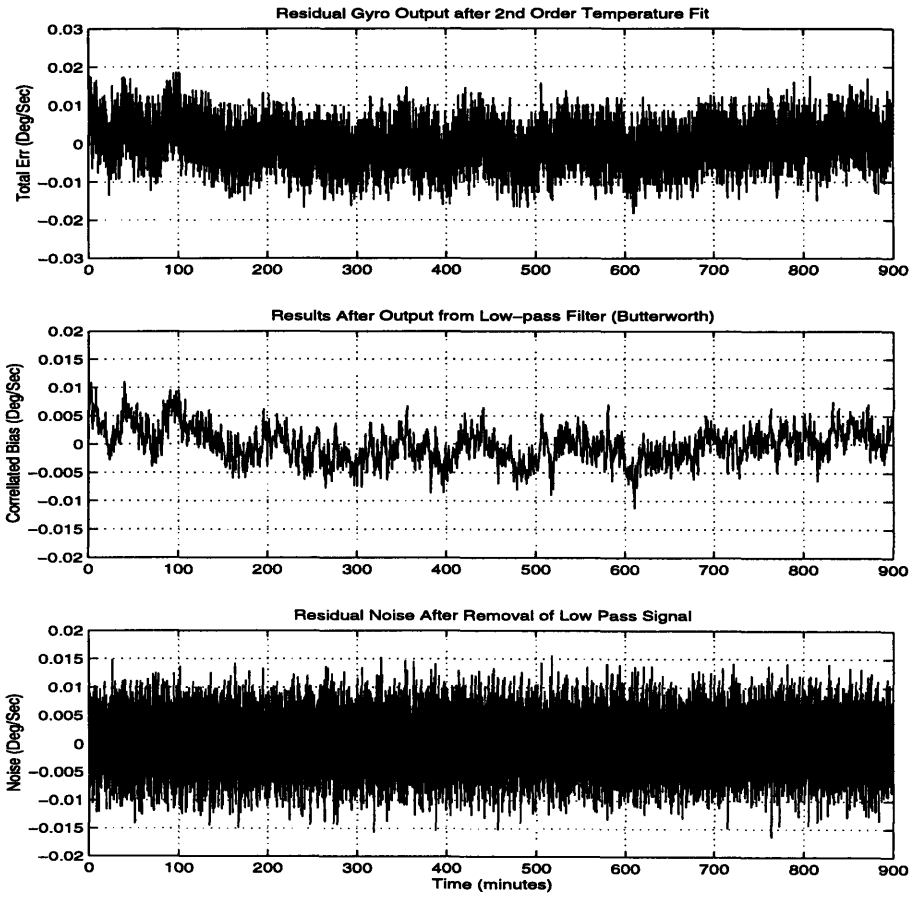

Figure 6.1: Data Analysis from a Prototype MM Gyro

The MM Gyro data had a bias of about 11°/hr and an ARW of .57 deg/hr$^{1/2}$.

6.2 Results

Draper Laboratory has made tremendous progress in the development of MM gyros and will continue to improve them from their present developmental stage. The results from

integrating the above data into the roof-top filter are shown below. The GPS updates came once every ten seconds. Again, although exact truth was not known, the covariance 1 σ overlays are centered about the mean.

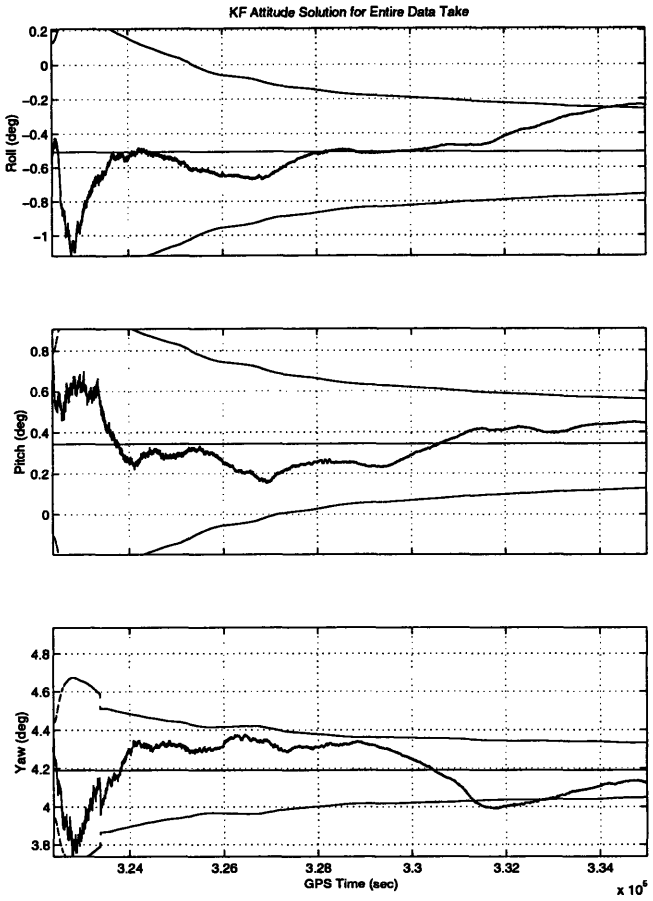

Figure 6.2: EKF Output Integrating Real Gyro Data and Real GPS Phase Measurements (GPS Update Interval of 1/10 Hz)

The results do not differ significantly from Figure 4.3. This attests not only to the importance of the dynamic model and the GPS measurements, but also shows that gyro qualities, of the levels needed for useful integration for this ADS, are being achieved. A run using the same gyro data with GPS updates at about once every minute is presented next. In this figure only a 30 minute frame of the three and a half hours is shown.

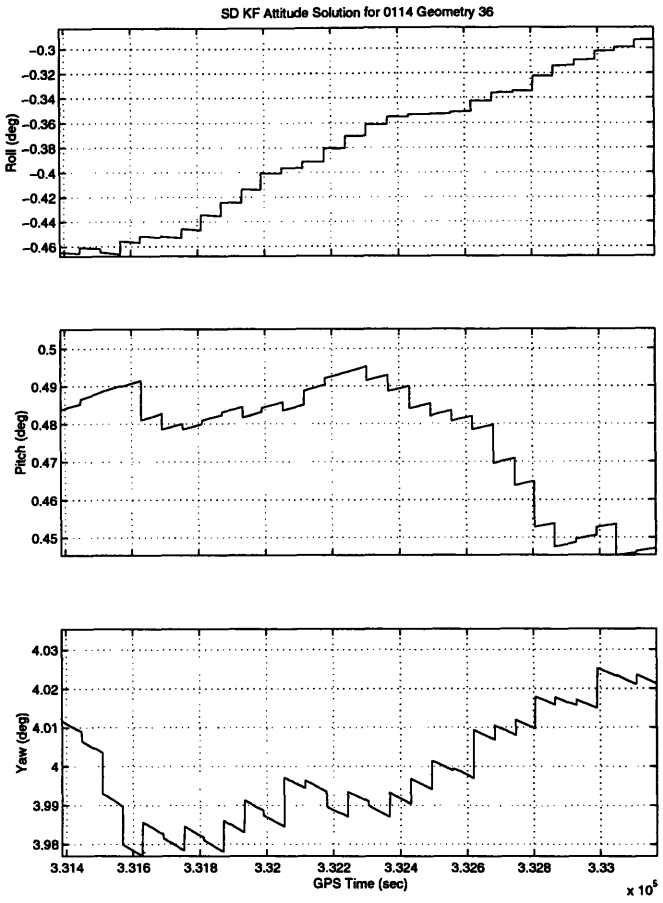

Figure 6.3: EKF Output Integrating Real Gyro Data and Real GPS Phase Measurements (GPS Update Interval of 1/64 Hz)

Figure 6.3 better illustrates how each GPS measurement update affects the estimate. With this view we can see that, if the gyro quality continues to improve, sporadic GPS measurements need to be used only for calibrating the gyro's low frequency bias. In addition to its use as a calibrating device, the IGPS receiver will provide redundancy to accomodate failure in the ADS. If the gyro suite is ever lost, the ADS could continue to operate as described in Chapter 5.

Chapter 7

Power Analysis

7.1 Introduction

In order for the IGPS/MM Gyro ADS to become viable, it must offer an efficient power budget. Chapter 4 analyzed the performance of this system as GPS use and gyro quality were varied. This chapter attempts to quantify the actual energy expenditure of this proposed system. Analysis is performed on simulations of typical orbital missions that the ADS would fly.

7.2 Interferometer

Although the differential phase data collected in Chapter 6 was done with a Trimble TANS Vector receiver, this chapter explores the concept of a minimum energy interferometric GPS receiver. Guinon characterizes and quantifies the energy needed for such a receiver in [10], and a summary will be presented below. Design information on commercial off-the-shelf interferometers like the TANS can be found in [5].

An IGPS will consume minimum energy if any receiver subsystems not in use are turned off. Consequently, when GPS update intervals are increased (as explored in Chapter 4), less energy will be used by the interferometer. The energy needed for a differential phase measurement is based on the energy consumed by the following GPS receiver sub-systems: the radio frequency electronics (RFE), the digital signal processor (DSP), the data dependent processor (DDP) and the reference oscillator. They are shown in the following figure.

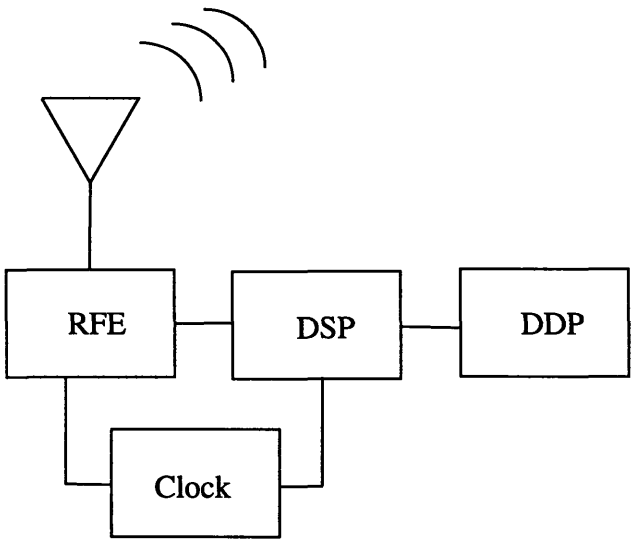

Figure 7.1: IGPS Receiver Sub-Systems

Radio Frequency Electronics

The RFE's, consisting of low noise amplifiers, one or more superheterodyne gain stages and an analog to digital converter; consume most of the power in an interferometer. Along with the reference oscillator and frequency synthesizer, the power consumption of the RFE (P_{RFE}), using available off-the-shelf technology, is 0.25 Watts per antenna. Guinon shows that the power consumption of a multiplexer offsets any benefits gained by sharing RFE's.

One way to save on power would be to use two baselines instead of three, therefore eliminating the need for one antenna's RFE. Phillips shows that converting the 1 m^2 array into one with only two baselines and three antennas is feasible [18]. The following figure illustrates this methodology.

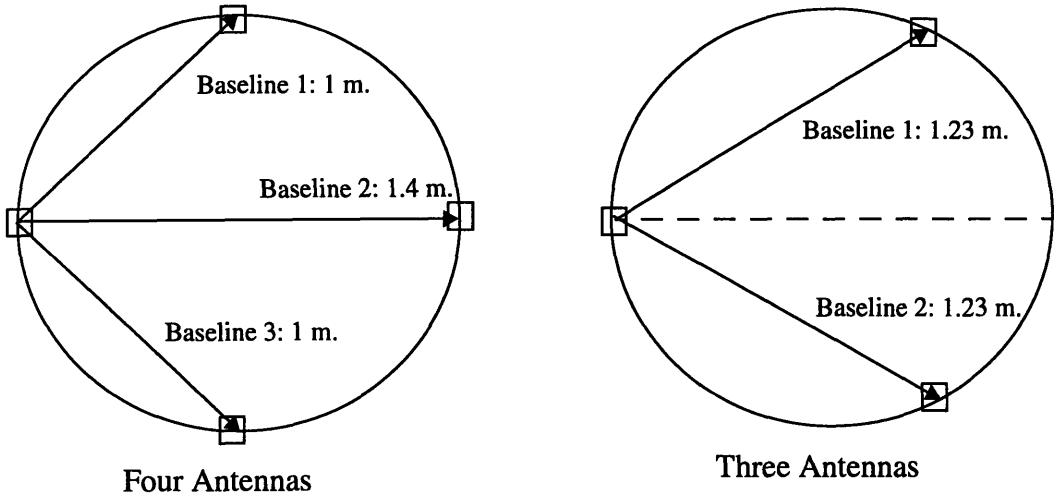

Figure 7.2: Four versus Three Antenna Configuration

There is only a small trade-off in accuracy for losing one antenna (since the baselines span the same plane); however, with the power savings that it provides, more GPS updates can be used. The increase in GPS measurement use actually allows for slightly better attitude estimation at equal power settings with the three antenna set-up. However, redundancy is lost since one lost antenna would cause a loss of three axis attitude estimation with the IGPS. (Although one baseline could still provide some attitude information, this analysis considers less than three functioning antennas a single point of failure since neither integer ambiguity nor a point solution can be calculated.) Because the three antenna design would lack the redundancy analyzed in Chapter 5, it is not considered further.

The energy used by the RFE's is defined by the product of power the hardware consumes and the length of time that it is on:

$$E_{RF} = P_{RFE} \cdot T_{IN} \tag{7.1}$$

where T_{IN} is the length of the signal intercept. Signal intercept length is a function of the method used for the L1 code alignment, as well as the signal to noise ratio, and is derived

in [Guinon].

Digital Signal Processor

The Digital Signal Processor (DSP) is specifically used for all arithmetically intensive computations inherent with Doppler delay analysis and carrier phase measurement of the GPS signal. The energy consumed by this subsystem is

$$E_{DSP} = N_{OP} \cdot E_{OP}(DSP) \tag{7.2}$$

where N_{OP} is the number of operations, or complex multiply accumulates (MAC's) needed to compute the Dopple/delay spectrum for all channels during code alignment, plus the number of MAC's needed for carrier phase measurement on all antennas. Operations on the order of 10^{10} are required for code lock, whereas only about 10^5 MAC's are needed for each phase measurement. E_{OP} is the energy per operation used by the processor. Assuming a processor such as an Analog Devices ADSP--2100 DSP Microcomputer, this energy consumption would be about 4 nJ (4 X 10^{-9} Joules) per 2X8-bit MAC. For a complete derivation of the minimum energy required for code lock and phase measurement see [10].

Data Dependent Processor

The Data Dependent Processor (DDP) is used for all calculations other than those performed by the DSP. These include satellite selection, computation of satellite position from a stored ephemeris, estimating the pseudo ranges and calculating the user position and clock bias. The DDP will also be used to integrate the gyro triad output, processing the Extended Kalman filter algorithms and computing the integer ambiguities when needed. Although the digital signal processor could be implemented to perform the DDP functions, it is assumed here that the DDP will be the main processor onboard the satellite.

This would facilitate integration with the attitude control system (ACS) as well as make it easier to alter the EKF from ground control since it would be inherently linked with the Telemetry, Tracking and Command (TT&C) sub-system. Another benefit of having the DDP be part of the main spacecraft processor is better line bias estimation since the thermal sub-system on the spacecraft could aid in temperature monitoring of the IGPS cables. The energy consumed by the Data Dependent Processor for running the IGPS/MM Gyro ADS can be characterized as

$$E_{DDP} = N_{OP} \cdot E_{OP}(DDP) \tag{7.3}$$

The number of operations performed by the DDP for this ADS will vary depending on the level of integration and algorithm complexity, but typical computations will include estimation of the pseudo ranges for positioning (which is important for LOS calculation) and integer ambiguity resolutions.

With past interferometric applications the integer ambiguity checks imposed a major computational burden. There are two reasons why this will not be a problem in this system. First of all, the DCAR method developed by Puri only requires operations on the order of 10^4 to resolve the integers and compute the least squares point solution attitude estimate for a one meter square array (which is the longest baseline considered here useful for small satellites). This is a great improvement over previous methods. The other reason has to do with the low probability that the integer resolver will even be called. The Extended Kalman filter keeps track of the ambiguities by forming the differential phase prediction. The only time the integer resolver is needed is when the measurement residuals become large due to the phase prediction not matching the phase measurement. Situations where this could conceivably occur might arise due to unmodeled control torquing of the vehicle. To determine the number of integer resolutions this system is likely to expect, the aforementioned orbital simulation was used. In the prior simulations, it was assumed that the control torques were exactly modeled (at least to the level of the process noise imposed on

the rate error state). The nominal control used in the simulation is a simple deadband controller that keeps the spacecraft aligned within a certain deadband angle, θ_{DB}. Now an unmodeled control is added within the orbit. This attitude control torque is typical of what a satellite in an Iridium-type constellation could expect in order to accomplish mission requirements such as satellite-to-satellite or satellite-to-ground node tracking. Figure 7.3 shows the true yaw, pitch and roll angles and rates experienced during a simulation of one oribt.

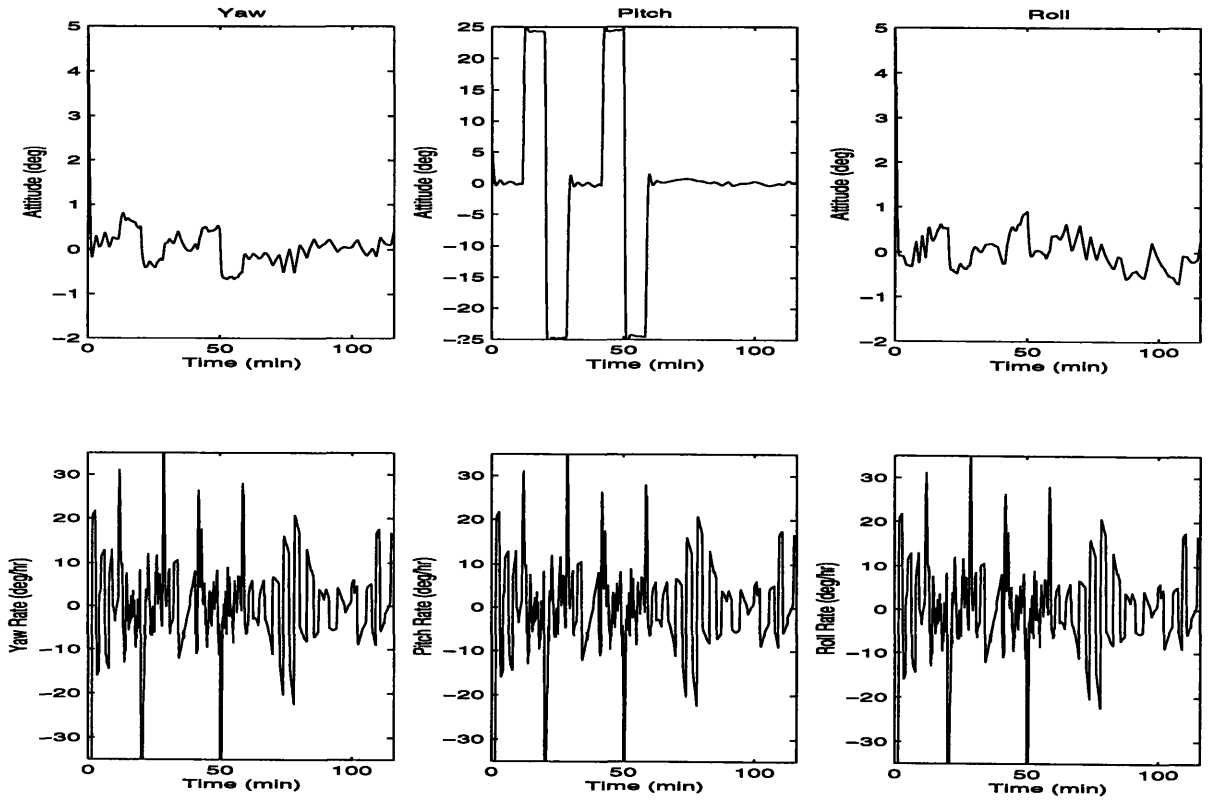

Figure 7.3: Simulation Attitude History

Notice the larger magnitudes during the mission dependent control maneuvers, especially in pitch. Figure 7.4 displays the attitude errors along with the 1 σ standard deviation overlays. The simulation was run at a 2 Hz gyro update frequency. GPS update frequency was 1/10 Hz except during the mission maneuvers where it was increased to 1 Hz.

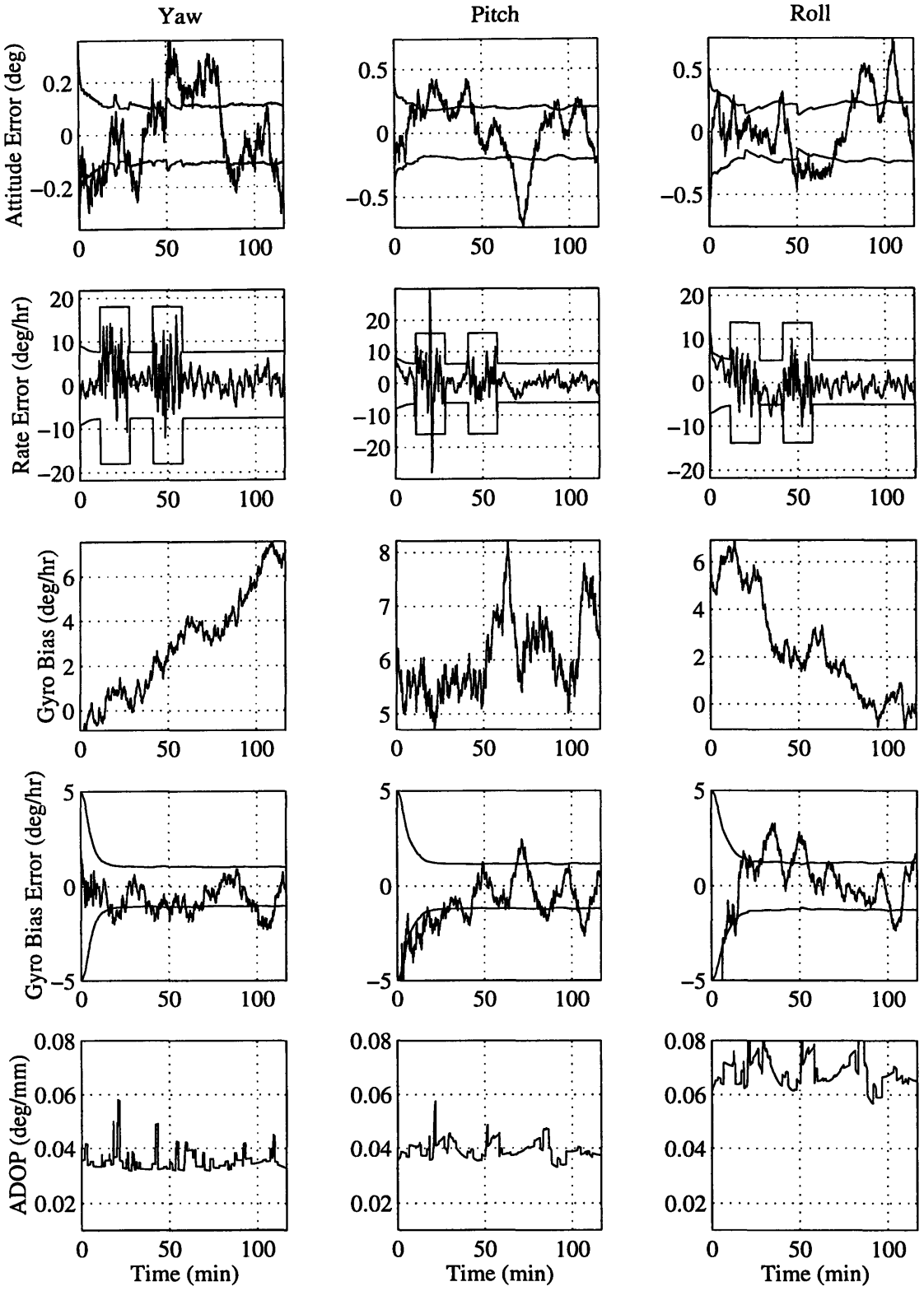

Figure 7.4: Simulation Results with Unmodelled Maneuvers

Notice the increase in the rate error variance, caused by an increase in the process noise, to account for the unmodelled control torques. Figure 7.5 and 7.6 show the history of the rest of the state errors.

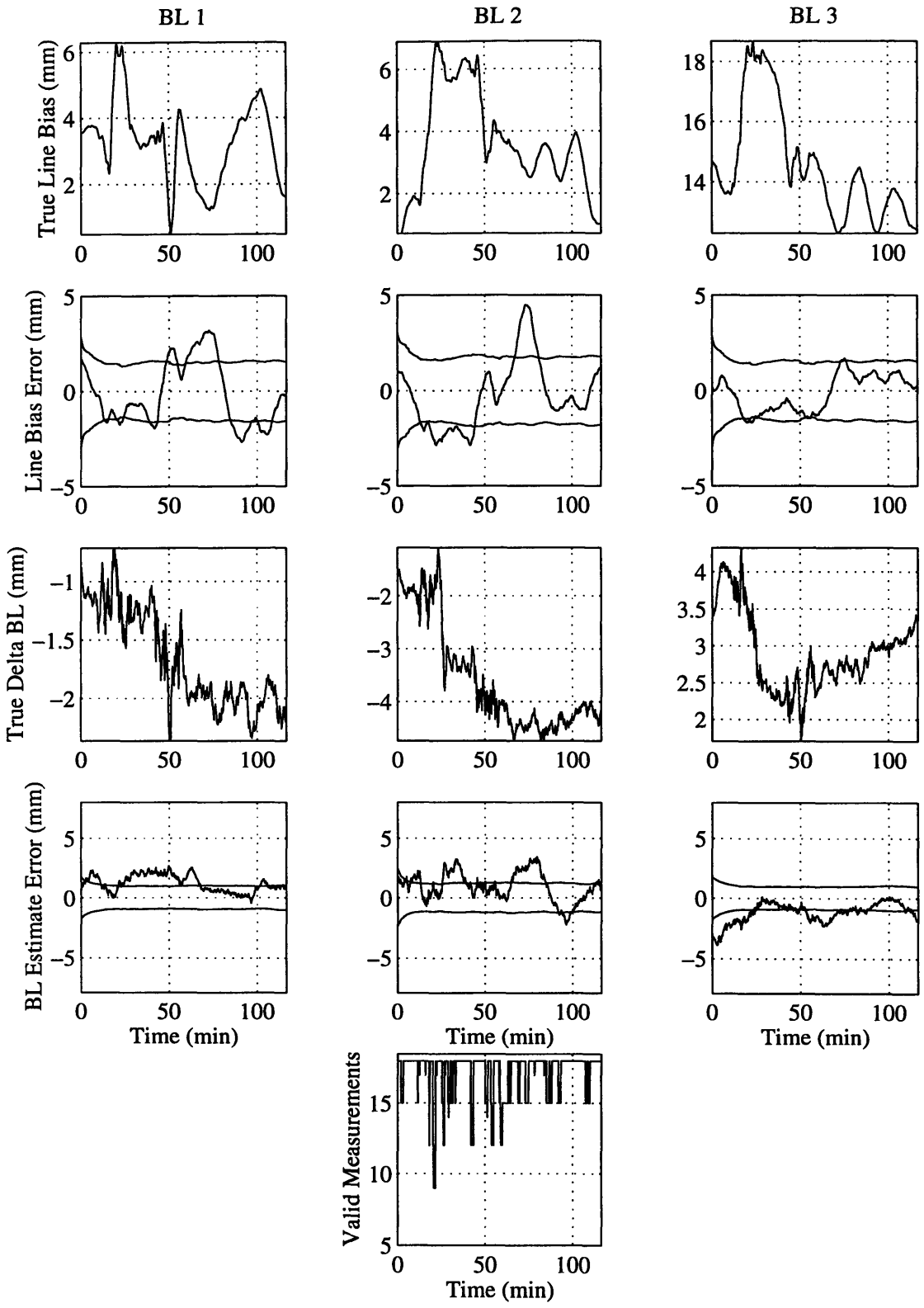

Figure 7.5: Simulation Results Continued

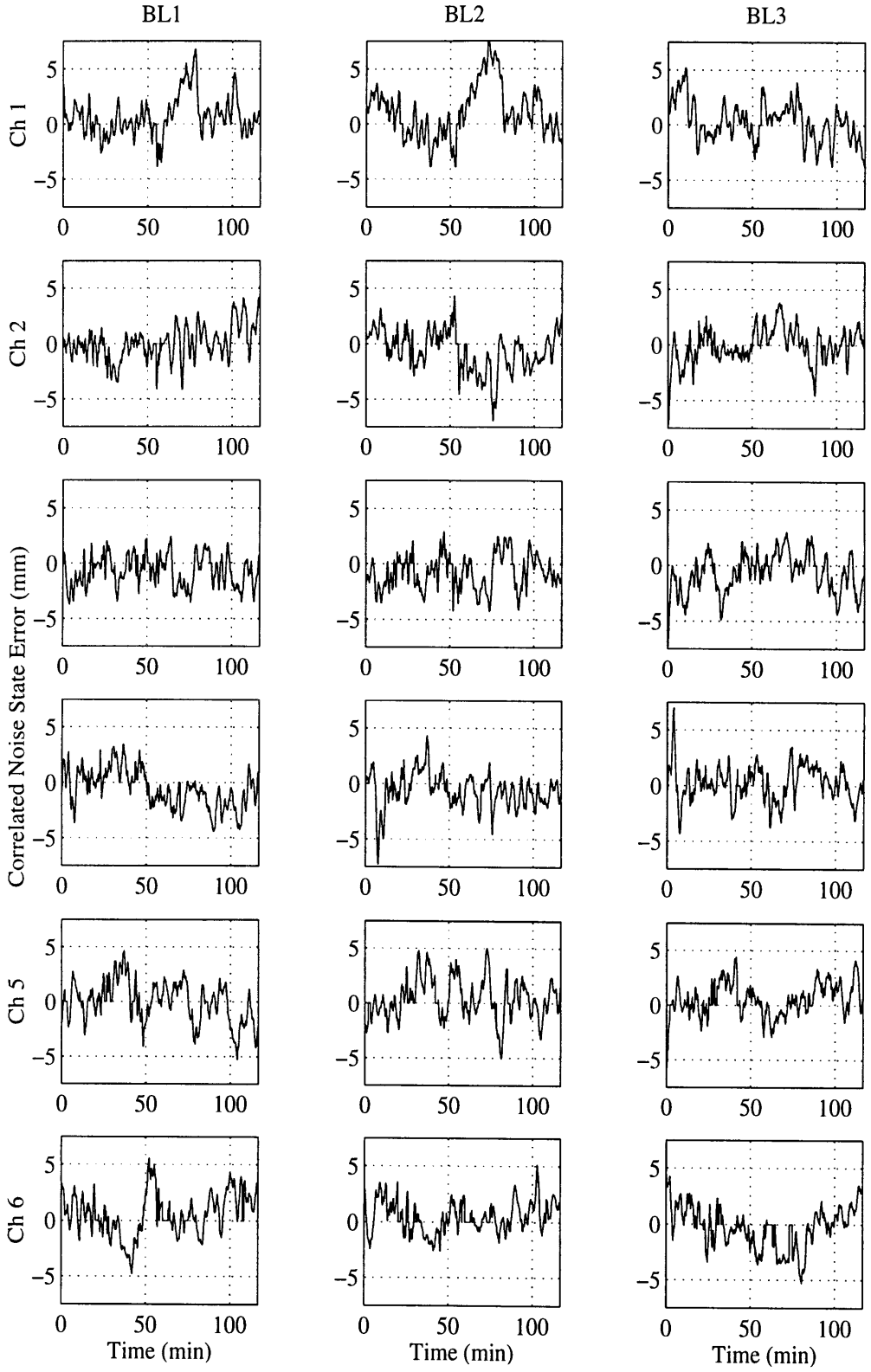

Figure 7.6: Simulation Results Continued

Notice the decrease in the number of valid measurements shown in Figure 7.5 during the mission dependent maneuvers. Even with less available measurements the EKF was able to hold integer lock. The integer ambiguity resolver was called twice during the entire orbit. The first time was the initialization. It was called a second time during the first maneuver period when GPS measurements were scarce. However, since the difference in the output of the DCAR was within a set threshold of the estimate, a filter reset was not called and the variances and states were allowed to keep propagating unchanged. Similar results were experienced when the GPS update intervals were kept at 1/10 Hz throughout the mission dependent maneuvers.

As shown above, the number of operations that the DDP will have to compute will not be significantly increased by the ambiguity resolver. Calculating the four pseudo ranges (three for position, one for time) and running the filter dependent algorithms will be largest source of operations required. To obtain a safe estimate of the magnitude of necessary calculations, the floating point operations count from the above simulation in Matlab is used. The simulation required an average of 10^5 calculations per second. It must be noted that the above simulation performed many more operations than would be required of this ADS. (These include operations such as simulating the gyro and phase measurements as well as computing environmental and system truth states). Using this number on a typical DDP, such as a Cirrus Logic ARM 7100FE 32-bit RISC processor, can give an idea of the power consumption required of this sub-system. The above device consumes 15 mWatts at an 18 MHz processor rate. Allowing 32 cycles for one floating point operation would mean less than 3 mWatts power consumption. Since this is such a small amount under such conservative projections, the DDP power expenditure required for this ADS will be ignored for the rest of this analysis.

7.3 MM Gyro

The MM Gyros currently being developed at Draper Laboratory are being packaged together with the ASICs that run the electronics. Current prototypes operate at roughly 200 mWatts per channel. New ASICs should cut this power down by a factor of four by the end of 1998 [13].

7.4 Total Power Consumption

From the above analysis total power consumption for the entire IGPS/MM Gyro ADS can be quantified. The total power will be a combination of the gyro triad expenditure plus the power consumption of the IGPS at the desired update interval. Adapting analysis performed by Guinon, the following figure describes the energy consumption of the IGPS.

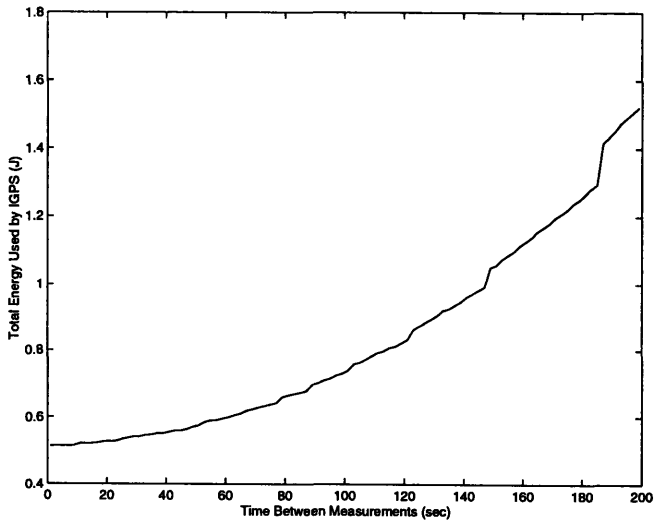

Figure 7.7: IGPS Energy Consumption vs. Time Since Last Measurement

The following figure illustrates the total ADS power consumption at varying GPS update intervals. Gyro triad consumption of 150 mWatts is assumed.

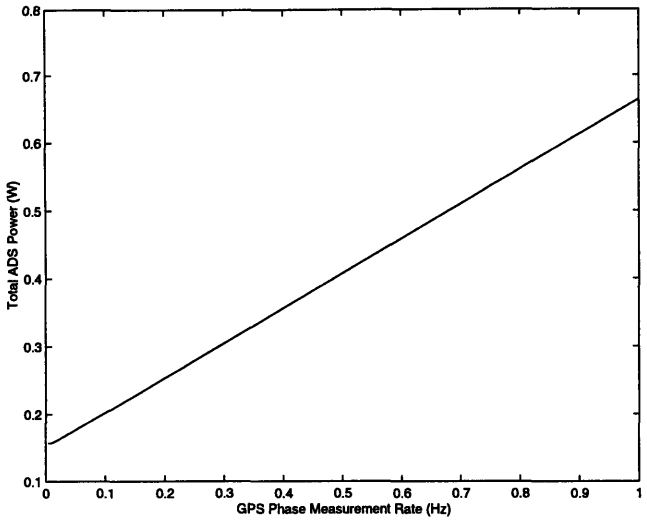

From the covariance analysis performed in Chapter 4 (reference Figure 4.6, for example), we see that the attitude estimation errors increase exponentially with decreasing GPS use. Attitude estimation errors do not significantly grow, however, until GPS update frequencies are lower than 1/30 Hz. Using a GPS update interval of 1/10 Hz would provide the performance capabilities detailed in Chapter 4 with a minimal ADS power consumption of 200 mWatts.

Chapter 8

Conclusions

The goal of this thesis has been to address some of the integration issues associated with the IGPS/MM Gyro ADS. Of chief concern was the power consumption of the interferometer and the robustness of the system to component failures. Successful tightly coupled integration of real micro-mechanical gyro data with real GPS phase measurements was also performed.

8.1 Summary of Results

The performance capabilities of the IGPS/MM Gyro ADS are a function of various parameters. These include gyro quality, dynamic model quality and the amount of interferometer use. The cost in power to operate this system is a function of the amount of interferometer use and the type of IGPS receiver (off-the-shelf versus minimal energy receivers).

A linear covariance analysis was used to quantify performance capabilities of the system with variations in the above stated parameters. It was determined that for GPS phase measurement updates in the range of one every second to one every 30 seconds, the attitude performance variation was less than .05 degrees. This justifies the development of a minimum energy receiver to take advantage of the potential power savings of less frequent GPS measurements.

Effects of varying the model quality of the EKF were also quantified. It was determined that in a worse case scenario, when for some reason the dynamic model in EKF provides

no additional information to the measurements, then the quality of attitude estimation was bound by the errors of the best sensor. When poor gyros are used this steady state error bound is the performance of the interferometer which for a 0.6 m^2 array is about 0.45 degrees 1 σ RSS attitude error and about 0.28 degrees for a 1 m^2 array within the GPS update range mentioned above.

Varying gyro qualities were also analyzed. For a projected MM Gyro with 5^o/hr bias, 8 hour time constant and $0.25^o/hr^{1/2}$ ARW, steady state 1 σ RSS attitude errors of about 0.3 and 0.2 degrees can be expected for a 0.6 m^2 array and 1 m^2 array, respectively, at a 1/10 Hz GPS update frequency.

The inherent robustness to failure aspect of the tightly coupled integration scheme implemented by this system was also analyzed. Using both a linear covariance analysis and actual space orbit simulations, the redundancy of this system was proven. Various sub-optimal cases were considered to include loss of gyro(s) and loss of a GPS antenna.

Chapter 6 presented EKF results using real gyro data obtained from a static laboratory test with real GPS phase measurements collected on the Draper Laboratory roof. Results confirm that the proposed integration scheme is experimentally valid with current technology.

Chapter 7 summarized the energy expenditures for the system. It was concluded that an ADS with 1 σ RSS attitude errors of about a quarter of a degree could operate at about 200 mWatts. The table below details what a typical ADS of the type needed to fill the telecommunication niche costs in terms of size, power and money. Note that the following quotes are rough estimates and were obtained from the specifications of typical components available in industry.

Sensor	Mass (kg)	Power (W)	Cost (K$)
INS	0.75	11	60-85
Sun Sensor	0.5	.5	40-60
Horizon Sensor	4	10	~200
GPS	1.5 (w/o antenna)	5	150
Total	~6.75	~27	~470

Table 8.1: Typical ADS Components

The following table summarizes the same type of estimate for the proposed IGPS/MM Gyro ADS.

Sensor	Mass (kg)	Power (W)	Cost (K$)
MM Gyro (triad)	0.5	.15	50
IGPS (1/10 Hz)	1	.05	50
Total	~1.5	~0.2	~100

Table 8.2: Estimates of the IGPS/MM Gyro ADS

Note that the gyro cost figure is a rough estimate for a system that is still in its developmental states. From the above tables it is easy to see how such a system could find a viable market in the growing telecommunications arena.

8.2 Suggestions for Future Work

The author can suggest several areas where future work can be concentrated. Due to time constraints for this thesis, a dynamic real data integration was not possible. As stated in

Chapter 6, MM Gyro data can be obtained from gyros mounted on turn-tables programmed at desired rates. This output can then be integrated into the space simulation used in this analysis. This would serve as a further step in validating the system, and it could be used as another way of testing its sensitivities.

Another area of study would be research into robustness methods for the model based estimation filter. Research in this area has already begun at Draper, but integration of robustness algorithms with actual data and a tightly coupled EKF has yet to be accomplished. Also, better dynamic models need to be developed. This study only characterized gravity gradient effects, but other torques such as internal spacecraft torques and control torques have yet to be modeled.

Finally, the GPS error models could benefit from better modeling of phase center variation and multipath. Real time identification of multipath has yet to be successfully implemented in such a design. Whether the benefits obtained from such calibration justify the cost (especially in a low multipath space environment) is another question left to be answered.

Appendix A

Derivation of Attitude Rate Dynamics

A.1 Introduction

As stated in Chapter 3, the model based nature of the Extended Kalman filter used in this study is highly dependent on the quality of modelling of the dynamics. The following will give a derivation of the dynamics of attitude rate error state, $\delta\underline{\omega}_{BN}^{B}$. Following the derivation will be a brief explanation of how this model is incorporated into the framework of the EKF.

A.2 Derivation

The angular rate error, $\delta\underline{\omega}_{BN}^{B}$, is the difference between the true rate and estimated rate:

$$\delta\underline{\omega}_{BN}^{B} = \underline{\omega}_{BN}^{B} - \hat{\underline{\omega}}_{BN}^{B} \tag{A.1}$$

To derive the dynamics of the angular rate error we first begin with Euler's vector equation of motion:

$$\frac{d}{dt}(\underline{\omega}_{BI}^{B}) = \boldsymbol{I}^{-1}(\boldsymbol{T} - \underline{\omega}_{BI}^{B} \times (\boldsymbol{I}\underline{\omega}_{BI}^{B})) \tag{A.2}$$

Applying equation A.1 we can linearize A.2 to yield

$$\frac{d}{dt}(\hat{\underline{\omega}} + \delta\underline{\omega})_{BI}^{B} = (\boldsymbol{I}^{-1}\{\boldsymbol{T} + \delta\boldsymbol{T} - (\hat{\underline{\omega}} + \delta\underline{\omega})_{BI}^{B} \times (\boldsymbol{I}(\hat{\underline{\omega}} + \delta\underline{\omega})_{BI}^{B})\}) \tag{A.3}$$

Subtracting the estimate of A.2 and ignoring higher order terms gives

$$\frac{d}{dt}(\delta\underline{\omega}_{BI}^{B}) = \boldsymbol{I}^{-1}([\boldsymbol{I}\hat{\underline{\omega}}_{BI}^{B}]_{X} - [\hat{\underline{\omega}}_{BI}^{B} \times \boldsymbol{I}])\delta\underline{\omega}_{BI}^{B} + \boldsymbol{I}^{-1}\delta\boldsymbol{T} \tag{A.4}$$

Using equation 3.42 we can expand the above to yield:

$$\frac{d}{dt}(\delta\underline{\omega}_{BN}^{B}) + \frac{d}{dt}(\delta\underline{\omega}_{NI}^{B}) = \boldsymbol{I}^{-1}([\boldsymbol{I}\hat{\underline{\omega}}_{BI}^{B}]_{X} - [\hat{\underline{\omega}}_{BI}^{B} \times \boldsymbol{I}])(\delta\underline{\omega}_{BN}^{B} + \delta\underline{\omega}_{NI}^{B}) + \boldsymbol{I}^{-1}\delta\boldsymbol{T} \tag{A.5}$$

By remembering the relation:

$$\frac{d}{dt}(A_Z) = \frac{d}{dt}(A_Y) + \underline{\omega}_{YZ} \times A \tag{A.6}$$

we know that:

$$\frac{d}{dt}(\delta\underline{\omega}^B_{NI}) = \frac{d}{dt}(\delta\underline{\omega}^N_{NI}) - \delta\underline{\omega}^B_{NI} \times \delta\underline{\omega}^B_{BN} \tag{A.7}$$

Furthermore, we can eliminate the second term above since for a circular orbit $\underline{\omega}^N_{NI}$ is constant leading A.5 to be expressed as:

$$\frac{d}{dt}(\delta\underline{\omega}^B_{BN}) = I^{-1}([I\hat{\underline{\omega}}^B_{BI}]_X - [\hat{\underline{\omega}}^B_{BI} \times I])(\delta\underline{\omega}^B_{BN} + \delta\underline{\omega}^B_{NI}) - \delta\underline{\omega}^B_{NI} \times \delta\underline{\omega}^B_{BN} + I^{-1}\delta T \tag{A.8}$$

Torque error is comprised of contributions from the gravity gradient and other sources and can be expressed via the small angle errors [23] as

$$\delta T = \frac{\partial T_{GG}}{\partial \underline{\Theta}}\delta\underline{\Theta} + \frac{\partial T_{GG}}{\partial \dot{\underline{\Theta}}}\delta\dot{\underline{\Theta}} + \delta T_{other} \tag{A.9}$$

The second term on the right side is zero since gravity gradient torque is a function only of angle displacement and not the rate. We ignore the contributions from other torque sources as well. In accordance with the analysis performed by Puri [20] , estimating torque errors such as aerodynamic or solar contributions yielded minimal improvements in a coupled interferometric-gyro attitude estimator as long as the process noise on the gyro replacement state was increased accordingly. The remaining torque error comes entirely from the gravity gradient and is given without derivation [23] as:

$$\begin{aligned}\delta T &= \frac{\partial T_{GG}}{\partial \underline{\Theta}}\delta\underline{\Theta} = \left[\frac{3\mu}{|\hat{R}|^5}([\hat{R}_X]I - [I\hat{R}]_X)[\hat{R}_X]\right]\delta\underline{\Theta} \\ &= [6\underline{\omega}^2{}_{NI}([\hat{r}_X]I - [I\hat{r}]_X)[\hat{r}_X]]\delta q^B_{BN}\end{aligned} \tag{A.10}$$

where the latter representation assumes a circular orbit. We finally have an expression for the angular rate error dynamics from the nav to body frame:

$$\frac{d}{dt}(\delta\underline{\omega}^B_{BN}) = \boldsymbol{I}^{-1}[6\underline{\omega}^2{}_{NI}([\hat{\boldsymbol{r}}_X]\boldsymbol{I} - [\boldsymbol{I}\hat{\boldsymbol{r}}]_X)[\hat{\boldsymbol{r}}_X]]\delta\boldsymbol{q}^B_{BN}$$

$$+\boldsymbol{I}^{-1}([\boldsymbol{I}\hat{\underline{\omega}}^B_{BI}]_X - [\hat{\underline{\omega}}^B_{BI}\times\boldsymbol{I}])(\delta\underline{\omega}^B_{BN} + \delta\underline{\omega}^B_{NI}) - \delta\underline{\omega}^B_{NI}\times\delta\underline{\omega}^B_{BN} \tag{A.11}$$

The linearized attitude dynamics then fall out as presented in Chapter 3. Following a similar derivation the pure attitude rate dynamics which are used to generate truth for the Extended Kalman filter follow the equation [20]:

$$\underline{\omega}^B_{BN} = \boldsymbol{I}^{-1}[\boldsymbol{T} - \underline{\omega}^B_{BI}\times\boldsymbol{I}(\underline{\omega}^B_{BI})] - \underline{\omega}^B_{NI}\times\underline{\omega}^B_{BN} \tag{A.12}$$

The term $\delta\underline{\omega}^B_{NI}$ is found by realizing that

$$\underline{\omega}^B_{NI} - \hat{\underline{\omega}}^B_{NI} = (\boldsymbol{C}_{BN}\cdot\underline{\omega}^N_{NI}) - (\hat{\boldsymbol{C}}_{BN}\cdot\underline{\omega}^N_{NI}) = (\boldsymbol{C}_{BN} - \hat{\boldsymbol{C}}_{BN})\underline{\omega}^N_{NI} \tag{A.13}$$

and remembering that

$$\tilde{\boldsymbol{C}}_{BN} = \boldsymbol{C}_{BN}\hat{\boldsymbol{C}}^T_{BN} \approx [\boldsymbol{1} + [\delta\underline{\Theta}]_X] \tag{A.14}$$

which, when applied to A.13 yields

$$\delta\underline{\omega}^B_{NI} = [\delta\underline{\Theta}]_X\cdot\underline{\omega}^B_{NI} \tag{A.15}$$

Appendix B

Roof-top Test Conditions

The conditions for the roof-top data collection of January 14, 1998, are summarized below. Time is in seconds and givein in GPS time. The differential phase measurements on this day used the GPS satellite geometries indicated on the first figure. The asterisk shows when the SV trajectory began. The second figure shows what channels were used at specific times.

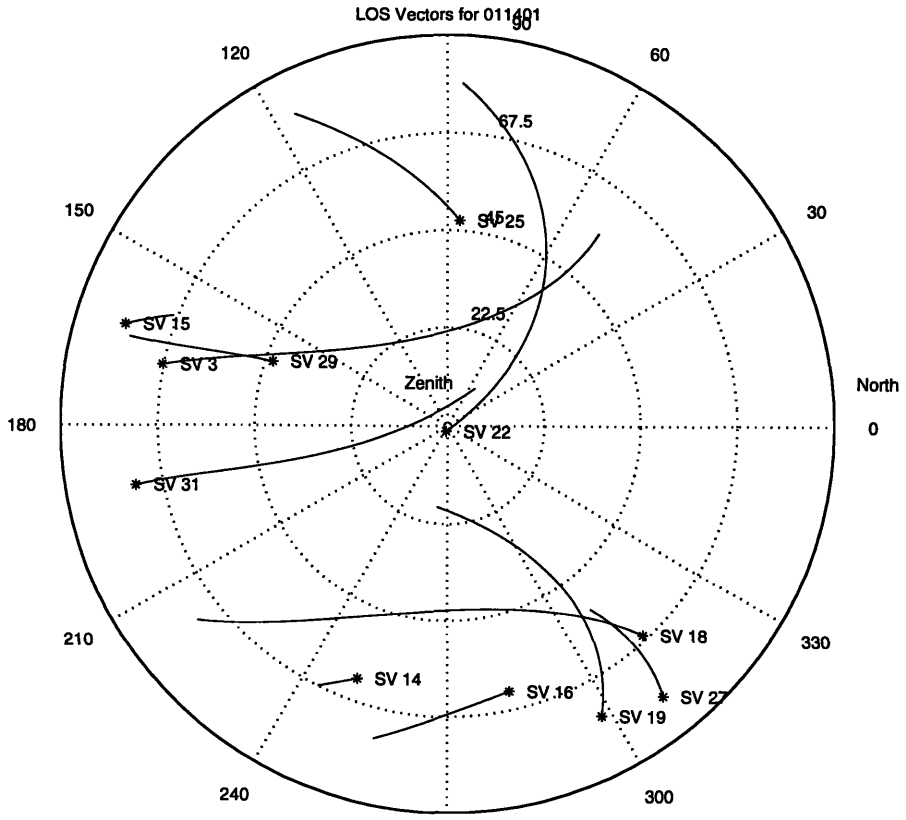

Figure B.1: GPS Satellite Geometries During Data Collection

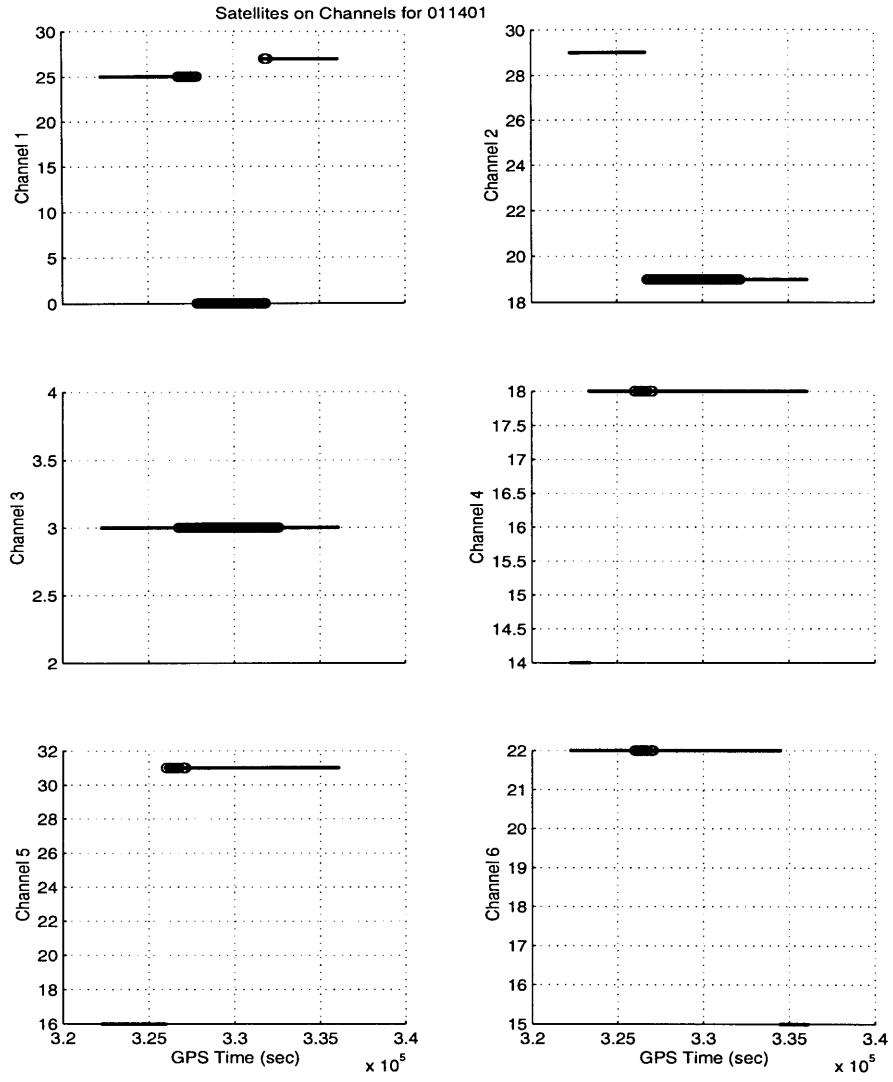

Figure B.2: Channels for Data Take

The thicker line regions are caused by circles being graphed instead of a line and correspond to times when there was an invalid measurement. However, all data for these regions is not bad since an invalid measurement at one second causes a circle to be placed on the graph which takes up more space than the second for which it corresponds. The following graph shows the total ADOP for the geometries of this data take.

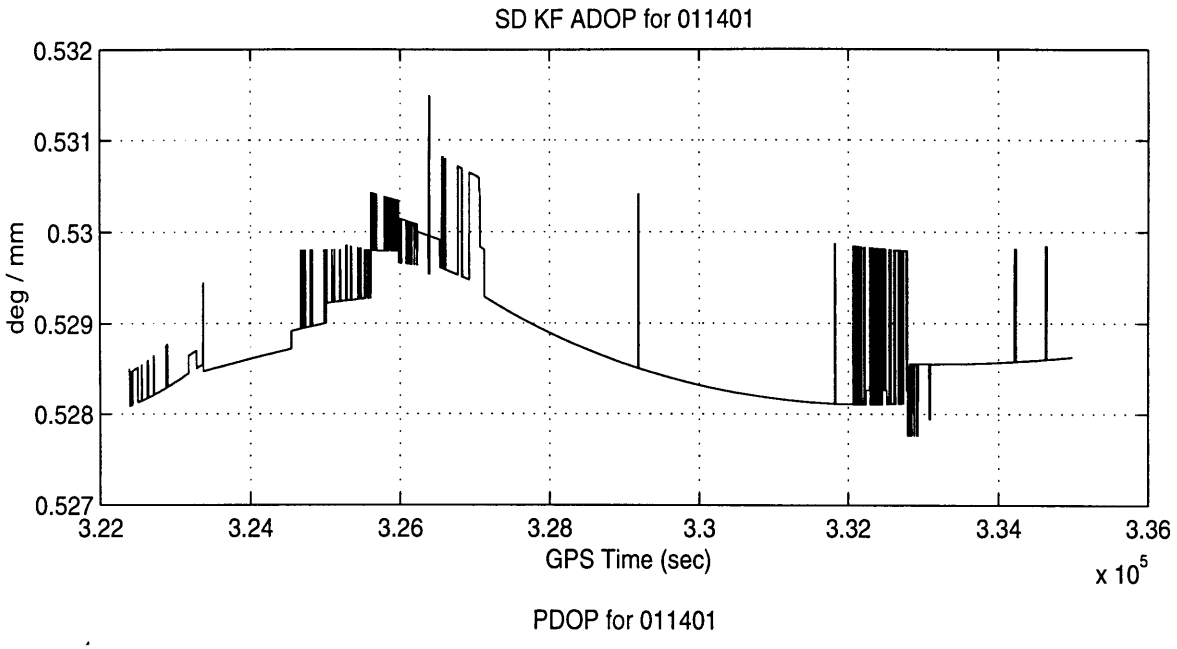

Figure B.3: Total ADOP for Data Take

Appendix C

IGPS Particulars

C.1 Introduction

The following Appendix contains a brief derivation of Attitude Dilution of Precision (ADOP) and a description of the single difference (SD) operator. More information on these two terms can be found in [20, 23].

C.2 ADOP

Dilution of Precision (DOP) is a term that describes how SV geometry degrades accuracy. Like the more common Geometric Dilution of Precision (GDOP), ADOP provides a measure of the theoretical attitude solution accuracy possible with a given satellite geometry. Recall from equation 3.61 that the sensitivity of the differential phase to attitude error is:

$$\frac{\partial \tilde{z}_{i,j}}{\partial \delta \mathbf{q}_{BN}^{B}} = 2 \cdot [\hat{\rho}_{j,est}^{B}]_{\times} \cdot \boldsymbol{b}_{i_0} \tag{3.62}$$

DOP has the general formula described by equation C.1:

$$DOP = \sqrt{trace[(\boldsymbol{H}^T \boldsymbol{H})^{-1}]} \tag{C.1}$$

so for the attitude case,

$$ADOP = \sqrt{trace[(\boldsymbol{H}_{\delta q}^T \boldsymbol{H}_{\delta q})^{-1}]} \tag{C.2}$$

For the ADOP calculations in this thesis, however, ADOP values correspond to the following equation:

$$ADOP = \sqrt{\sigma_{\varphi}^2 + \sigma_{\theta}^2 + \sigma_{\psi}^2} \tag{C.3}$$

which is effectively twice the value computed in equation C.2.

C.3 Single Difference Operator

When a differential phase measurement is taken, a slave antenna phase is subtracted from the master antenna phase. This procedure is represented by the single difference operator:

$$\begin{bmatrix} \Delta\varphi_{1,1} \\ \Delta\varphi_{2,1} \\ \Delta\varphi_{1,2} \\ \Delta\varphi_{2,2} \\ \cdots \end{bmatrix} = \begin{bmatrix} 1 & -1 & 0 & 0 & 0 & 0 \\ 1 & 0 & -1 & 0 & 0 & 0 \\ 0 & 0 & 0 & 1 & -1 & 0 \\ 0 & 0 & 0 & 1 & 0 & -1 \\ & & & \cdots & & \end{bmatrix} \cdot \begin{bmatrix} \varphi_{M,1} \\ \varphi_{1,1} \\ \varphi_{2,1} \\ \varphi_{M,2} \\ \varphi_{1,2} \\ \varphi_{2,2} \\ \cdots \end{bmatrix} = SD \cdot \begin{bmatrix} \varphi_{M,1} \\ \varphi_{1,1} \\ \varphi_{2,1} \\ \varphi_{M,2} \\ \varphi_{1,2} \\ \varphi_{2,2} \\ \cdots \end{bmatrix} \tag{C.1}$$

GPS errors, such as multipath, phase center variation, receiver noise and line bias, are errors which corrupt the carrier phase before the antenna phase differencing takes place. (Baseline length error is an exception since it does not effect the raw carrier phase.) The resulting differential phase errors (for a three baseline example) are represented by the single difference operator:

$$\underline{\Delta e} = \begin{bmatrix} \Delta e_{1,j} \\ \Delta e_{2,j} \\ \Delta e_{3,j} \end{bmatrix} = SD \cdot \begin{bmatrix} e_{M,j} \\ e_{1,j} \\ e_{2,j} \\ e_{3,j} \end{bmatrix} = \begin{bmatrix} 1 & -1 & 0 & 0 \\ 1 & 0 & -1 & 0 \\ 1 & 0 & 0 & -1 \end{bmatrix} \cdot \begin{bmatrix} e_{M,j} \\ e_{1,j} \\ e_{2,j} \\ e_{3,j} \end{bmatrix} \tag{C.2}$$

where e is an error vector on undifferenced carrier phase, and Δe is the effect of the error on differential phase. The correlation between baselines is described by:

$$\Lambda_{\underline{\Delta e}} = E[\underline{\Delta e} \cdot \underline{\Delta e}^T] = E[\underline{SD}\underline{e} \cdot \underline{e}^T \underline{SD}^T] = SD \cdot \Lambda_{\underline{e}} \cdot SD^T = \begin{bmatrix} 2 & 1 & 1 \\ 1 & 2 & 1 \\ 1 & 1 & 2 \end{bmatrix} \cdot \sigma_{\underline{e}}^2 \tag{C.3}$$

where $\Lambda_{\underline{e}}$ is the covariance of the error on undifferenced carrier phase. The differential phase error covariance, $\Lambda_{\underline{\Delta e}}$, has two times the variance of the original error and is corre-

lated across baselines [20].

References

[1] Brown, R. G. and P. Y. C. Hwang, *Introduction to Random Signals and Applied Kalman Filtering*, John Wiley & Sons, Inc., New York, NY, 1983.

[2] Chesley, B. and P. Axelrad, "Integrated GPS Attitude Determination System for JAWSAT", *Proceedings of ION GPS*, Vol. 2, 1994, pp. 1251-1261.

[3] Chesley, B. C., *An Integrated GPS Attitude Determination System for Small Satellites*, Ph.D. Dissertation, Department of Aerospace Engineering Sciences, University of Colorado, 1995.

[4] Chu, D., Wheeler, Z., and Sedlak, J., "Motion Models in Attitude Estimation," *NASA Goddard Space Flight Center, Flight Mechanics/Estimation Theory Symposium*, 1994, pp. 545-557.

[5] Cohen, C. E., *Attitude Determination Using GPS*, Ph. D. Dissertation, Department of Aeronautics and Astronautics, Stanford University, Dec. 1992.

[6] Cohen, C.E. and B. Parkinson, "Mitigating Multipath Error in GPS Based Attitude Determination," *Advances in the Astronautical Sciences,* Vol. 74, 1991, pp. 53-68.

[7] Fujikawa, S. J. and D. F. Zimbelman, "Spacecraft Attitude Determination by Kalman Filtering of Global Positioning System Signals," *Journal of Guidance, Control and Dynamics,* Vol. 18, No. 6, Nov.-Dec. 1997, pp. 1365-1371.

[8] Garrison, T., M. Ince, J. Pizzicaroli, and P. Swan, "IRIDIUM® Constellation Dynamics: The Systems Engineering Trades," *46th International Astronautical Congress,* Oct. 1995.

[9] Gelb, A. (Ed.), *Applied Optimal Estimation*, The MIT Press, Cambridge, MA, 1974.

[10] Guinon, W., "Minimum Energy Design of a Spacecraft Attitude Determination System," C. S. Draper Laboratory Report, Feb. 12, 1998.

[11] Kaplan, E. D., *Understanding GPS Principles and Applications*, Artech House, Inc., Norwood, MA, 1996.

[12] Kourepenis, A., J. Borenstein, J. Connelly, P. Ward, and M. Weinberg, "Performance of Small, Low Cost Rate Sensors for Military and Commercial Applications," *23rd Joint Services Data Exchange for Guidance, Navigation and Control,* Nov., 1996.

[13] Kourepenis, A., Private Communications, Mar.-Apr. 1998.

[14] Larson, W. J., and J. R. Wertz (Ed.), *Space Mission Analysis and Design,* Microcosm, Inc., Torrance, California and Kluwer Academic Publishers, Dordrecht, The Netherlands, 1992

[15] Lefferts, E. J., F. L. Markley, and M. D. Shuster, "Kalman Filtering for Spacecraft Attitude Estimation," *Journal of Guidance, Control and Dynamics,* Vol. 5, No. 5, Sept.-Oct. 1982, pp. 417-429.

[16] Mahar, K. B., Private Communications, Jan.-May 1998.

[17] Parkinson, B. W., and J. J. Spilker, Jr. (Ed.), *GPS Theory and Applications,* American

Institute of Aeronautics and Astronautics, Inc., Washington, D.C, 1996.

[18] Phillips, R. E. "Antenna Array for a Spacecraft Attitude Determination System," C. S. Draper Laboratory Memo #E43-98-032R, Apr. 98, 1998.

[19] Phillips, R. E., Private Communications, Jan.-May 1998.

[20] Puri, V., *Tightly Coupled GPS-Gyro Integration for Spacecraft Attitude Determination*, S. M. Thesis, Department of Aeronautics and Astronautics, MIT, June 1997.

[21] Savage, P. G., *Introduction to Strapdown Inertial Navigation Systems*, 7th Printing, Strapdown Associates, Inc., 1996.

[22] Shuster, M. D., A Survey of Attitude Representations," *The Journal of the Astronautical Sciences*, Vol. 41, No. 4, Oct.-Dec. 1993, pp. 439-517.

[23] Stohl, J. C., *Performance Analysis of a GPS Interferometric Attitude Determination System for a Gravity Gradient Stabilized Spacecraft*, S. M. Thesis, Department of Aeronautics and Astronautics, MIT, May 1995.

[24] Tranquilla, J. M., and Colpitts, B. G., "GPS Antenna Design Characteristics for High Precision Applications," *Proceedings of the ASCE Specialty Conference on GPS-88 Engineering Applications of GPS Satellite Surveying Technology,* 1988, pp. 2-14.

[25] Ward, L. M., *Spacecraft Attitude Estimation Using GPS: Methodology and Results*, Ph.D. Dissertations, Department of Aerospace Engineering Sciences, University of Colorado, 1996.

[26] Wertz, J. R. (Ed.), *Spacecraft Attitude Determination and Control,* D. Reidel Publishing Company, Dordrecht, Holland, 1978.